
Università Politecnica delle Marche
Scuola di Dottorato di Ricerca in Scienze dell'Ingegneria
Corso di Dottorato in Ingegneria Industriale - Ciclo XXXIV

---

# Innovative 3D-printed gamma-camera collimators for medical imaging

Ph.D. Dissertation of:
**Lorenzo Verdenelli**

Supervisor:
**Prof. Lorenzo Scalise**

Assistant Supervisor:
**Dr. Luigi Montalto**

Academic Year: 2020-2021

# Abstract

In nuclear medicine, the gamma-camera is one of the most used imaging devices for radionuclide imaging. Gamma-cameras are the key point of many devices used in nuclear medicine ranging from the scintigraphic system to SPECT (Single photon emission computed tomography) system. The main aim of a gamma-camera is to provide to the physician useful information in terms of spatial resolution and sensitivity of the organ under investigation. So, starting from previous studies where the AM (Additive manufacturing) technologies have been applied for the realization of collimators, we proceeded providing a novel concept of a parallel hole collimator with optimized hole shape and with a completely novel fabrication strategy, printing the negative of the traditional collimator. With "negative geometry" we mean extruding the holes, usually empty, and filling then the space between these holes with a high dense metal powder (eg. Tungsten). Applying this concept, we found to be able to provide a fully customizable and low-cost product using traditional FDM (Fused deposition modeling) and SLS (Selective laser sintering) printing technologies. Two different geometries, for a total of six samples, have been 3D printed. These samples have been then filled by hand-filling process with tungsten powder and have been scanned, using CT scanner, in order to evaluate how the powder is dispersed between the septa. An imaging system used to acquire the printing process has been also mounted on-board of the FDM printer and it has been used to acquire a picture of each printed layer while being illuminated by three laser-line illuminators working in the 630 nm range (red illuminators). Laser illuminators have been placed to provide the best and constant illumination conditions on the imaged layer. Images have been post-processed and used to recreate a 3D model of the printed part to be then used in the simulation software GATE. A numerical analysis, based on GATE Monte Carlo toolkit, has been conducted to simulate the reference and the innovative concepts collimators. The simulation have been done using different radio-isotopes (Tc99, Lu177, In111 and Ga67) and materials (Tungsten, PLA and PA2200). Experimentally, the sample have been proved with the Tc99m, In111 and Ga67 sources, to confirm the validity of the proposed idea. Results of the numerical analysis show a similar behavior for what concern the spatial resolution with the respective reference collimators, while for the sensitivity a reduction that range from 45% up to 80% of entries is reported. This is due mainly to the extruded pixel, made of PLA or PA2200, having higher density ($\sim$1.24 g/cc for PLA and $\sim$0,95 g/cc for PA2200) with respect to air ($\sim$0,0012 g/cc). The 3D reconstructed model using the imaging system has been numerically evaluated as well, demonstrating that the additive process errors, such as non-linearity and non-parallelism between the extruded holes, can have a worsening effect on the system performance. For future application further implementations are needed, specially for what concern the filling procedure that must be improved in order to reach an higher percentage of filled powder.

# Contents

# List of Figures

# List of Tables

# Chapter 1

# Introduction

Nowadays the development and the continuous growing and updating of additive manufacturing technologies and consequently the born of several 3D printing brands with low cost machines, have made available to everyone the possibility to purchase a 3D printer. The most diffuse are those based on the FDM technology, that cover more than 60% of the 3D printer market. Thanks to this widespread diffusion more and more research groups have purchased a 3D printer for rapid prototyping or to fabricate functional parts for their needs. However, these technologies have always been confined to specific industrial sectors, mainly, automotive, robotic or in the medical field with a huge focus on the additive manufacturing of prostheses, scaffolds for the growing up of biological tissues or for implants such as the dental one. However, in the medical field additive manufacturing has the possibility and potentiality to be applied to many other aspects, not only related to the biological world, but also for what concern mechanical or optical components for nuclear medicine diagnostic or therapy devices. It is precisely on the therapy and diagnostic devices that we focused the research work presented here. Particularly, we focused on gamma camera systems and precisely on the first layer of its sandwich structure which is given by the collimator. Nowadays, the collimator production is still based, for the majority, on the traditional fabrication techniques, such as machining bulky blocks of dense metal (e.g. lead) for example, that require a huge amount of time to be produced, a huge amount of waste material due to the working process that result in a significant final cost for the final product. Considering a standard collimator with dimension 105x55x45 mm, with hexagonal holes arranged in parallel, the total cost can be of few thousands of euro. This cost is replicated also using metal additive manufacturing technologies where tungsten powder is used. In this case the cost can be easily around ∼8000 euro. These costs, obviously can be easily faced by big research groups, hospitals or companies. But, in case a small or medium research group or a small company, as could be a start-up, or a small hospital, would like to have available a collimator for a nuclear medicine imaging device with specific and custom geometries, and performance ad-hoc for the purpose of their investigations, it could be a huge expense to face. This, typically leads to choose collimators that show an average behavior in terms of spatial resolution and sensitivity.
This problem could be faced applying the additive manufacturing processes nowadays available. As a case study, in this work, we investigated the possibility and the feasibility to fabricate an innovative small collimator concept to be used on a scintigraphic imaging system supplied with the Biomession Technology Solutions [1], for small ani-

mal imaging studies. The proposed collimator has been developed from the necessity to adapt the 3D printing technologies to fabricate such a particular geometry in terms of dimensions and specially in terms of materials used for the production. Materials that are available only for the metal additive manufacturing processes, that unfortunately, have shown to be still really expensive and not affordable from everyone. We investigated the use of two of the most used 3D printing technologies available on the market that are the FDM (Fused deposition modeling) and the SLS (Selective laser sintering) technology. These technologies have shown to be good and reliable additive manufacturing processes for rapid prototyping, specially the SLS that shows better performance in terms of accuracy and precision of printing with respect to the FDM prinetrs (specially if the FDM printer is a cheap one). The FDM process has been also flanked by an imaging system used to follow and control the printing process. Indeed, using FDM printers the problem is not only confined to the materials choice but also to the errors of the printing process itself that can cause geometries errors that can derive in many different scenarios.

# Chapter 2

# Context: Gamma-Camera imaging system, problem definition and motivation

## 2.1 Radionuclide imaging system

Radionuclide imaging systems are the most important devices in nuclear medicine. The widest used imaging device is the *gamma camera* also known as the *Anger scintillation camera*, named after its inventor, Hal Anger, that replaced the previously used film-screen for radiation detection with an single large area NaI(Tl) crystal and a photomultiplier.
The aim of a radionuclide imaging system is that to collect a distribution of the radio-pharmaceutical injected within the patient body(e.g., intravenous injection). The collection of the emission from the radio-pharmaceutical is possible thanks to an external detector located at different distances from the body of the patient. This permits the physicians to image the organ under investigation as it could be for the heart, where it is used to study the myocardial perfusion assessing coronary artery disease and heart muscle damages after infarction. Depending on the type of investigation it want to be performed and according to the type of tomographic investigation system used (planar, SPECT or PET) different kind of radionuclide can be used. If the system is a SPECT (single photon emission computed tomography) or planar 2-D scintigraphic system, the radionuclide used shows $\gamma$-rays with an approximate energy emissions ranging from 80 to 500 keV, while if the system is a PET (Positron emission tomography) only positron emitting radionuclide can be used, showing high energy of annihilation photons (511 keV).
These kind of energies are usually adequately penetrating within the tissues to be assimilated by the deep-lying organs. An important aspect to take in consideration is that the detectors used in the gamma camera should have a really good detection efficiency for the $\gamma$ rays and they should also be able to discard all those gamma rays that, due to Compton scattering inside the patient's body, have lost positional information and so are not useful to the organ's image production.
The efficiency of the detection system, the really good image quality and the relative ease of use made the gamma camera the first choice for nuclear-imaging systems like SPECT.

The gamma camera can be thought as a sandwich, composed of several layers, as can be seen in Figure 2.1. Each layer has a specific role in the formation of the final image of the organ under investigation. The front component is the collimator. The collima-

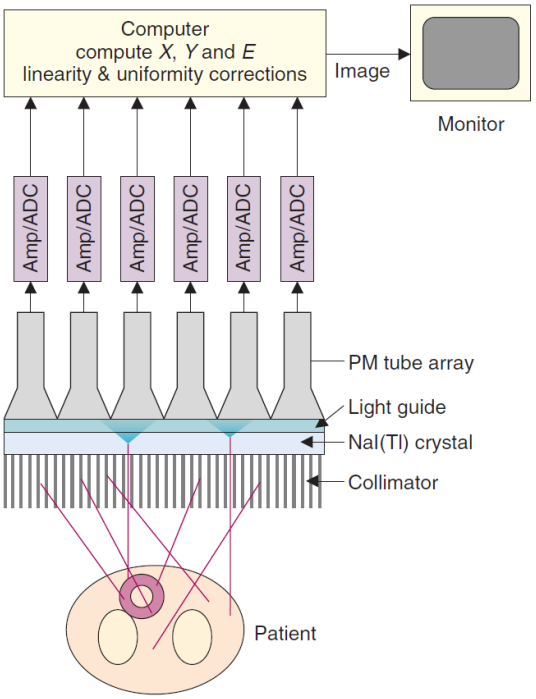


Figure 2.1: Basic configuration of a typical gamma camera. X,Y position of gamma-ray emission and E energy of the photon. Courtesy:Physics in Nuclear Medicine [10]

tor is usually made up of lead plate where several holes have been made. Its role is to guide the incoming photons towards the scintillation crystal, typically NaI(Tl), that is the second layer of the system and is responsible for the conversion of the incoming radiation into visible pulses of light. Pulses of light that are then guided, thanks to a light guide, towards, usually, two or more photo-multipliers (PMT) tubes[10]. Usually several PMT are used in order to better detect the position of the incoming light for the correct formation of the image. The output signal from a PMT is directly proportional to the amount of visible light recorded from the crystal. The signal coming out from the PMT is usually amplified by a large factor. The current produced at the anode is very small so, immediately after the PMT are placed amplifiers which role is to transform this current into voltage which can be then converted into a digital signal thanks to an analog-to-digital (ADC) converter.[9] The digitized signal is then passed to a digital position logic circuit that determine the X-Y location of each scintillation pulse (that reflects the position of the incoming photons inside the patient's body), compute the energy (E, proportional to the total measured pulse amplitude) deposited by the gamma ray accepting the energy that falls into a specific energy windows and that is useful for the final image formation. The energy collection before forming the final image is really important. Indeed, selecting only that energy that, falling between a specific energy window, assures a discrimination against those $\gamma$-rays that scattering inside the patient's body will loose their positional information

producing noise, a useful image from the clinical point of view is assured. Typically, a narrow pulse-height analyzer window, centered around the photopeak, is chosen guaranteeing that only those photons that show no scatter or a really small-angles scatter inside the body are accepted and processed.

But, in order to obtain the image of the organ under investigation, it is necessary that the incoming $\gamma$-rays from the radioactive source are correctly projected onto the detector. This collimation is properly performed by the collimation system, that as previously said, represents the first layer of the gamma-camera system.
The collimator, above all the other components, play a fundamental role in the definition of the final image, since it is responsible for the spatial resolution (collimator spatial resolution) and sensitivity of the system itself. The collimator is typically made of dense metals that show high atomic number Z and density. The necessity for this kind of metals relates to the fact that the collimator, in order to correctly projects the incoming photons on the detector, to reproduce the image of the organ, needs to have an absorptive component. Component this, that is given by the metals high density and atomic number. Usual metals used are lead ($\rho$=11.3 g/cm$^3$ and Z= 82) that is the most common metal used due to its availability and cost and tungsten ($\rho$=19.3 g/cm$^3$ and Z= 74); but also metals like tantalum ($\rho$=16.6 g/cm$^3$ and Z= 73), gold ($\rho$=19.3 g/cm$^3$ and Z= 79) and even depleted uranium ($\rho$=18.9 g/cm$^3$ and Z= 92).[10]
This absorptive properties permit only those photons that travel straightforward with a specific direction to reach the crystal detector, while blocking instead all the other rays coming obliquely and that will produce a useless contributes to the final image. Unfortunately, this absorption tends also to block some photons that traveling slightly obliquely will carry useful information. So, it's really important that the collimator is properly designed in order to achieve the maximum spatial resolution and sensitivity admissible.

### 2.1.1 Basic collimators

According to the type of investigation that a physician wants to perform and according to the isotope energy used too, different kinds of collimators should be used. There are four standard types of collimators that are typically used with a gamma camera and are: parallel hole collimator, diverging hole, converging hole and pin-hole collimator. Each of these collimators show properties and performance on their own.
The most common collimator, used in the majority of laboratories, is the *parallel hole collimator*. This kind of collimator is usually made from drilling or casting lead foils together. It is composed of several holes, positioned in order to be parallel between each other. These holes show different shapes ranging from the hexagonal to the square one passing through circle or triangle shapes. However the most common and used shape is the hexagonal one (Figure 2.2). This collimator projects an image onto the detector that is neither magnified or minified as it is possible to observe in the scheme in Figure 2.3. The image projected on the detector surface has dimensions equal to the one of the object imaged and no distortion is present as instead is when using converging collimator for example, as we will see later. Another really used collimator is the pin-hole collimator, that with the converging one, is mostly used in all those situations where there is the need for a magnification of the organ under investigation, such as for imaging thyroid or heart or also in small-animal imaging

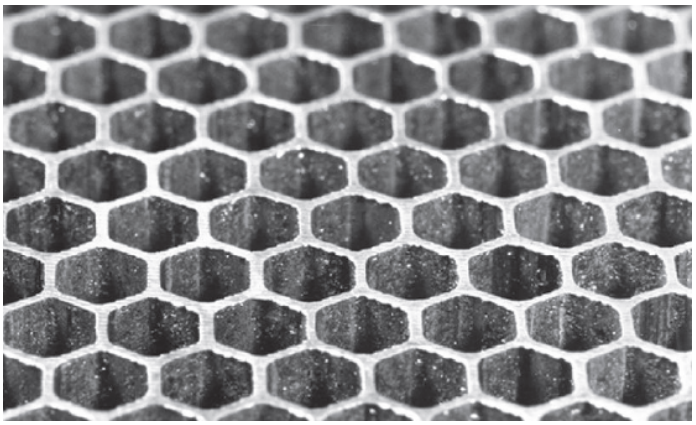

Figure 2.2: Typical parallel-hole collimator. Courtesy:Physics in Nuclear Medicine[10]

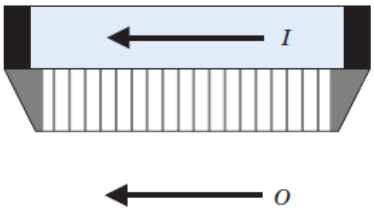


Figure 2.3: Parallel-hole collimator scheme. Courtesy:Physics in Nuclear Medicine[10]

application. The pin-hole collimator that can be seen in Figure 2.4 consists of a really small aperture located at the top of a conical structure typically made of lead. The aperture is few millimeters small and the distance with respect to the detector

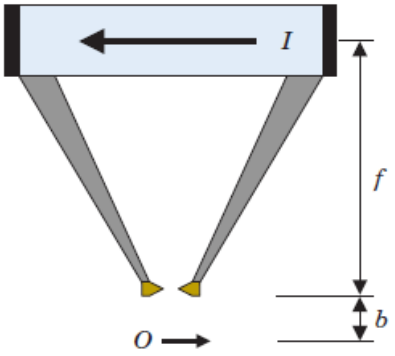


Figure 2.4: Pin-hole collimator scheme. Courtesy:Physics in Nuclear Medicine[10]

ranges from several centimeters in human applications pin-hole to few centimeters in small-animal applications. A rule of thumb to respect with this kind of collimator is that the dimension of the detector should be at least twice the dimension of the organ under investigation. This aspect is really important to consider because, as for the converging collimator too, we have a magnification of the target on the detector

and for this reason we need a detector surface big enough to accommodate both the target and the background so to be able to separate the two and compute the spatial resolution and sensitivity of the system. For example if we are imaging the thyroid that is typically 1-2 cm big we should have a detector 4x4 cm $^2$ in order to recognize it with respect to the background. If for example we are using a magnification factor equal to 5 in order to magnify 5 times the thyroid then we need a detector with dimensions equal to 20x20 cm$^2$.
The image projected by the pin-hole on the detector is an inverted image and the image is magnified or minified according to the distance $b$. The image size I and object (source) size O are related according to

$$I/O = f/b \tag{2.1}$$

I and O are respectively the image projected in the detector and source size.

An example of the magnification effect of the pin-hole collimator can be observed in Figure 2.5 where the imaging characteristics of the pin-hole are compared with respect to the one of the parallel hole. As it is possible to see the parallel hole collimator does not produce any magnification or minification and the image is not inverted when projected onto the detector, as previously said, while the pin-hole highly magnify the object an produce an inverted image onto the detector according to eq. 2.1. The other

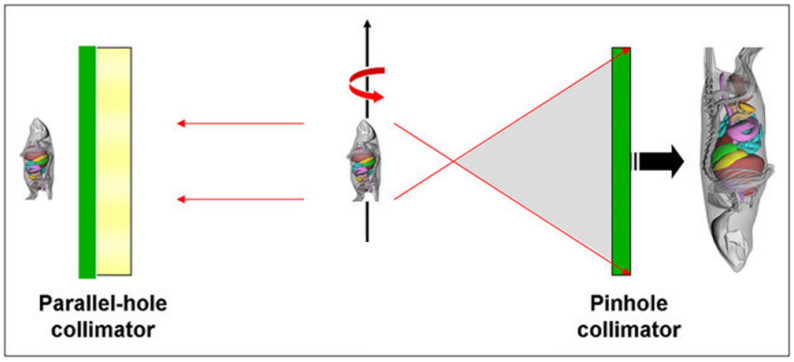


Figure 2.5: Parellel hole vs Pin-hole collimator. Courtesy:Robert A DeKemp

two most used collimators are the *diverging collimator* and the *converging collimator*. A diverging collimator (Figure 2.6) has holes that diverge from the detector face. The holes diverge from a point typically 40-50 cm behind the collimator, projecting a minified, non-inverted image of the target onto the detector. The level of minification is strongly related, as for the pin-hole collimator too, on the distance $f$ from the front of the collimator to the convergence point, the distance $b$ from the front of the collimator to the object (source), and the collimator thickness $t$ according to the following equation [10]

$$I/O = (f - t)/(f + b) \tag{2.2}$$

Usually this kind of collimator are used on those gamma camera that mount a small detector. The drawback using this collimator as the converging one or the

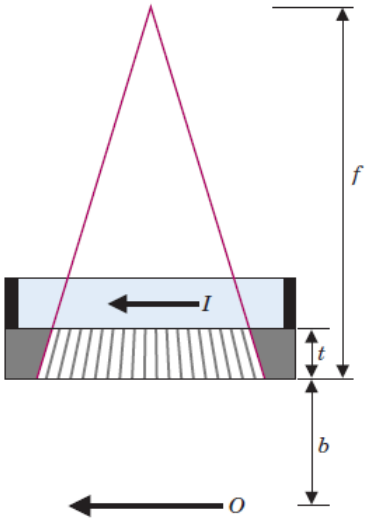


Figure 2.6: Diverging collimator scheme. Courtesy:Physics in Nuclear Medicine[10]

pin-hole is that, changing the size of the object modifying the distance source to collimator, there is a certain amount of image distortion.

The converging collimator works in the exact opposite way of the diverging one. A converging collimator (Figure 2.7) has holes that converge to a point 40-50 cm in front of the collimator. For objects between the collimator face and the convergence point, the converging collimator projects a magnified, non-inverted image of the source distribution. Image size I and object size O are related according to:

$$I/O = (f + t)/(f - b) \tag{2.3}$$

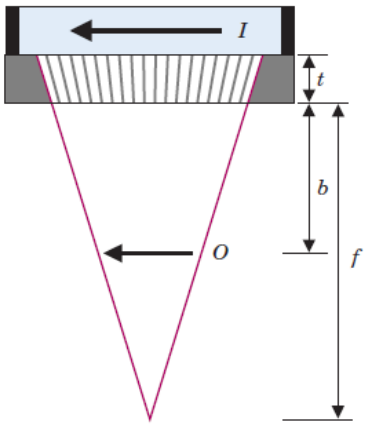


Figure 2.7: Converging collimator scheme. Courtesy:Physics in Nuclear Medicine[10]

In opposition to the diverging collimator, the converging one are used with those gamma-camera that presents larger detector that permit to image magnified source distribution. As already said, because the image size change with the distance from collimator to source distribution we experience some distortion as can be seen in Figure 2.8 where two images, one obtained using a parallel hole collimator and the other using the converging one are reported.

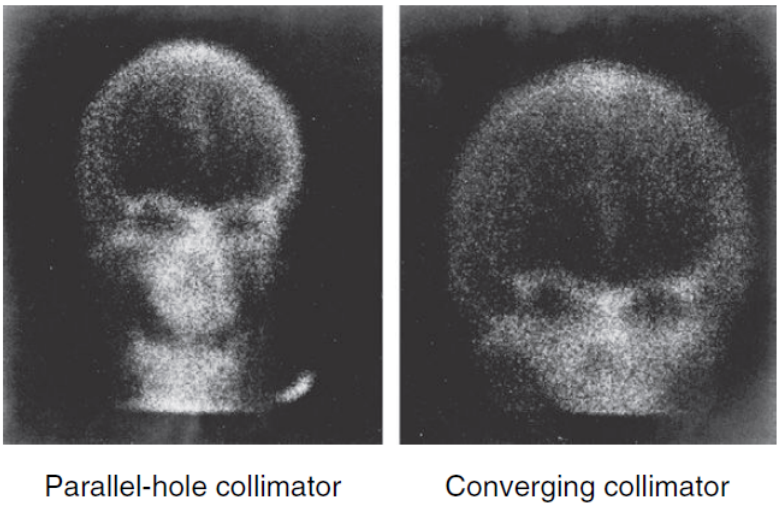


Figure 2.8: Image distortion of converging collimator compared with the parallel hole collimator. Courtesy:Physics in Nuclear Medicine [10]

### 2.1.2 Measurement characteristics of a Gamma-camera

The performance of a gamma-camera is a sum of several important aspects. A good gamma-camera should show a good spatial resolution, a good detection efficiency, good capacity to measure the energy of the incoming radiation and a reliable counting rate. The spatial resolution can be separated into *intrinsic spatial resolution*, that depends by the detector and the electronics used and into *collimator spatial resolution* which is related to the type of collimator used.

#### Intrinsic spatial resolution

The intrinsic spatial resolution is usually computed placinig a lead mask with several narrow slits (1 mm) on the face of the detector without placing the collimator on it. The image detected by the system can be seen in Figure 2.9 and consist of a series of lines.

The resolution is computed as the full width at half maximum (FWHM) of a profile

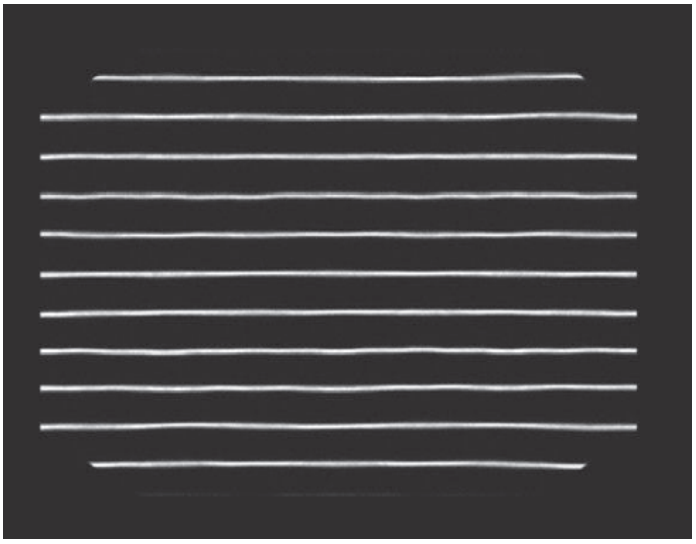

Figure 2.9: Straight-line test pattern obtained with a gamma camera for intrinsic spatial resolution measurement. Courtesy:Physics in Nulcear Medicine[10]

drawn perpendicular to the image of the lines at different locations in the field of view (FOV). Typically, the resolution computed with this method for standard gamma-camera is around 2.9 - 4.5 mm FWHM. The intrinsic resolution greatly depends from the detector (crystal thickness), system electronics and $\gamma$-rays used. A decrease of the energy used results in a worse intrinsic resolution as observable in Figure 2.10 (a). Crystal thickness also play an important role in the definition of the intrinsic resolution. Thicker detector indeed, results in greater spreading of scintillation light before it reaches the PM tubes, causing a much higher probability in detecting Compton-scattered events resulting in final noise on the image. This effect can be seen in Figure 2.10 (b), where at an increase in crystal thickness there is a worsening of the the spatial resolution.

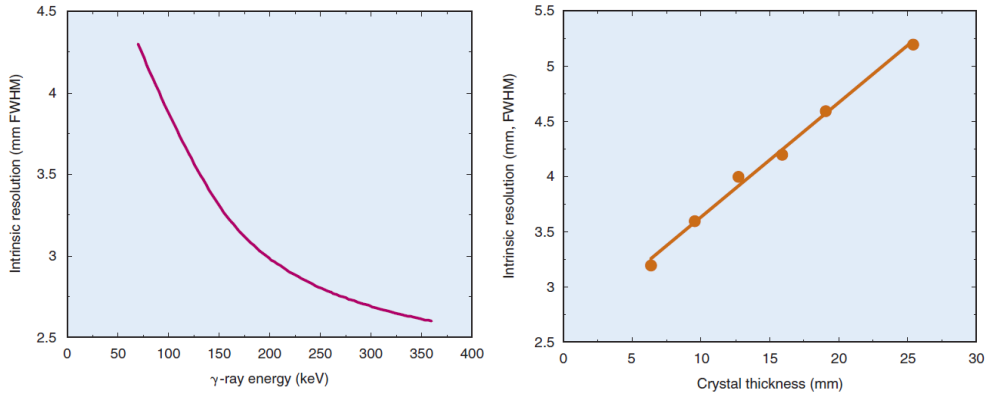


(a) (b)

Figure 2.10: (a) Intrinsic spatial resolution of a gamma camera as a function of $\gamma$-ray energy. (b) Intrinsic spatial resolution of a gamma camera at 140 keV as a function of crystal thickness Courtesy:Physics in Nuclear Medicine[10]

### Detection efficiency

Another aspect to consider when speaking about a gamma-camera is its *detection efficiency*, that is its efficiency in detecting the photopeak of the radionuclide used for the clinical investigation. The efficiency of photopeak detection increase with the increase in crystal (NaI(Tl)) thickness. So thicker crystals lead to better detection efficiency but tend to decrease the intrinsic spatial resolution. It is really important in this context to find a trade off in crystal thickness so to have both good detection efficiency and intrinsic spatial resolution.

### Energy resolution

Besides the detection efficiency another important parameter to take in consideration is the *energy resolution*. In a typical clinical investigation the number of Compton-scattered photons could be much higher than the unscattered one. It is really important to discriminate against the former one using a pulse-height analyzer applying an energy windows around its photopeak. The energy resolution is a measure of how efficient is the detector to discriminate against the scattered photons. Good energy resolution leads to have narrower photopeak in first place. This means that the photopeak is composed almost entirely by scattered photons, increasing the number of useful $\gamma$-rays recorded. Secondly, $\gamma$-rays that have been scattered from angles greater than 45 degrees are rejected in a more efficient way, providing a much better image contrast. The width of the photo-peak, $\Delta$E, is referred to be the energy resolution of the detector, also known as the *full-width-at-half-maximum* (FWHM). Typically the FWHM and so the energy resolution is defined as a percentage of the photo-peak energy ($E_\gamma$) of the radionuclide used:

$$FWHM(\%) = (\Delta(E)/E_\gamma) \times 100\% \tag{2.4}$$

In Figure 2.11 the energy spectrum of $^{99}$Tc-m obtained with a standard gamma camera is shown. Around its photopeak settled at 140 keV an energy window is applied using a pulse height analyzer (PHA) in order to use only that energy that show no or very little scatter photons. Typically, an energy window of ± 10 % or ± 20 % is used. In the specific case presented in the image an energy window of ± 15 % has been applied.[10]

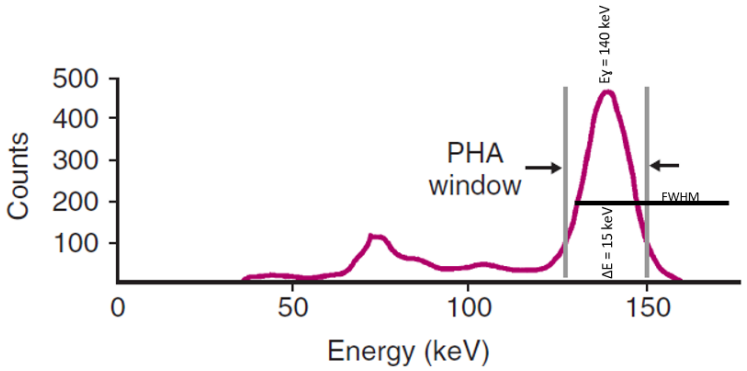


Figure 2.11: Tc99-m energy spectrum with energy window applied around the photopeak at 140 keV. Courtesy:Physics in Nuclear Medicine[10]

#### System sensitivity

System sensitivity of the gamma-camera is strictly dependent on the collimators used. For this reason it should be measured separately for each collimator used. Typically for low-energy collimators the radionuclide used is $^{99}$Tc-m ($E_\gamma$ = 140 keV). The sensitivity is computed as:

$$Sensitivity(cps/Bq) = \frac{countsinROI - backgroundcountsinROI}{time(sec)xsourceactivity(Bq)} \tag{2.5}$$

where the ROI refers to the region of interest and the background counts in ROI refers to the background noise recorded with the source removed.

## 2.2 Collimators influence on medical imaging systems

The collimator, due to its absorptive capacity, permits only a small percentage of the incoming $\gamma$-rays to strike the detector, resulting in a low efficiency. This effect results also in a poor collimator resolution if compared to the intrinsic resolution. These are limiting factors meaning that the collimator should be designed carefully in order to minimize as much as possible this efficiency and spatial resolution worsening. A bad design of it, will result in a useless collimator system.
Considering a parallel hole collimator several considerations must be kept in mind for its design. As said, the collimator is a very important layer of the gamma-camera

imaging system since it is responsible for projecting the incoming photons onto the detector providing the best image possible. In order to achieve the best projected image onto the detector it is necessary that the $\gamma$-rays penetration between the collimator parallel holes is as small as possible. Typically, since it is impossible to to stop all the incoming gamma rays and at the same time have good system efficiency, some penetration is accepted; usually around $\sim 5\%$ is a reasonably accepted value. From Figure 2.12 it is possible to determine the septal thickness required. The shortest path the incoming gamma-rays has to travel is $w$.

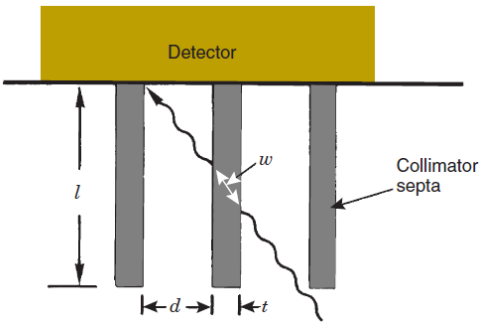


Figure 2.12: Shortest path length for a gamma-ray to travel through a collimator septa. Courtesy:Physics in Nuclear Medicine[10]

Since the septal thickness depends both on $w$, and on the height of the collimator $l$, and on the hole diameter $d$ according to the following equation:

$$t = 2dw/(l - w) \tag{2.6}$$

Supposing the septal penetration is less than $\sim 5\%$, the transmission factor for the specific thickness has to be:

$$e^{-\mu w} < 0.05 \tag{2.7}$$

with $\mu$ that is the linear attenuation coefficient of the material the septa is made of. Considering that $e^{-3}$ is about 0.05, this implies that:

$$\mu w > 3 \tag{2.8}$$

$$w > 3/\mu \tag{2.9}$$

$$t > \frac{6d/\mu}{l - (3/\mu)} \tag{2.10}$$

As a standard the septal thickness should be thick enough to block the majority of the oblique incoming gamma-rays, but small enough to not cover too much the underneath detector area causing a worsening of the system efficiency. Since $\mu$ is the linear attenuation coefficient is important to produce this kind of object using

materials, for the septa, with a large $\mu$ value.
Typically metals that show high atomic number and high density are preferred to achieve this purpose. For this reason the most used metals, as already said, are lead (Z=82, $\rho$=11.3 g/cm$^3$) and tungsten (Z=74, $\rho$=19.3 g/cm$^3$) that show high performance in stopping power and in if compared to the other metals that could be used such as gold, tantalum or uranium. When determining the septal thickness of the collimator, is also really important to consider the $\gamma$-rays energy involved. Different energies means different septal thickness, specially if we are using high energy such 400 keV or higher there is the need of thicker septa to block the incoming oblique photons. For example in small animal imaging application where the radionuclide used is $^{99}$Tc-m, which shows an energy peak around 140 keV (*low-energy $\gamma$-ray emitter*), it is highly preferable to use collimator with thin septa in order to collect the greater number possible of photons. Of course it could be also used a *medium-energy collimator* but at the expense of collimator efficiency because we will have thicker septa that will block more photons [10].
Next to the septal thickness, another important aspect to consider when designing a collimator is the holes geometry. Typically, in order ot maximize the crystal area exposed to the radiation circular, hexagonal or square holes are used. What really affects the collimator efficiency in this case is the hole length and diameter. Usually the collimator resolution is computed as the the full width at half maximum (FWHM) of the radiation profile obtained from a point source or line source (Figure 2.13). It

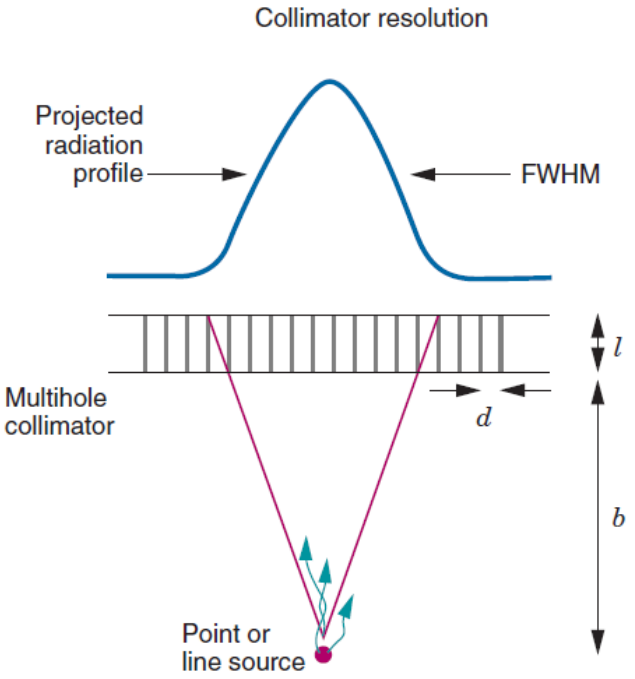


Figure 2.13: Radiation profile and FWHM. Courtesy:Physics in Nuclear Medicine[10]

is given by:

$$R_{coll} = \frac{d(l_{eff} + b)}{l_{eff}} \tag{2.11}$$

where $l_{eff} = l - 2\mu^{-1}$ represents the effective length of the hole considering both the length (l) of the hole itself and the linear attenuation coefficient ($\mu$) of the metal used, $b$ is the actual distance from the point source and the front face of the collimator and $d$ is the hole diameter.
The efficiency of the collimator is instead computed considering the amount of $\gamma$-rays that pass through the collimator per $\gamma$-rays emitted by the source. It is given by:

$$g \approx K^2(d/(l_{eff})^2[d^2/(d+t)^2] \tag{2.12}$$

where $t$ is the septal thickness while $K$ is a constant dependent by hole shape.
What is evident from the previous two equations (2.11 and 2.12) is that the collimator resolution will show an improvement when the ratio of the hole diameter to the effective length is made smaller [10]. Thus, imply that in the case we make a collimator with long and narrow holes we will experience an improved spatial resolution but we will also have a decrease in photons collection, causing a worsening of the collimator efficiency as the square of the ratio of the hole diameter to the effective length $(d/(l_{eff})^2)$. Collimator efficiency and resolution are therefore related as follow:

$$g \propto (R_{coll})^2 \tag{2.13}$$

According to the equation 2.11 we can also see that the collimator resolution tends to decrease with the increase of $b$ that is the distance from the source and the collimator front face. This condition that make the resolution worsening can be appreciated looking at Figure 2.14 where three different collimators are compared in terms of spatial resolution and source-to-collimator distance [10].

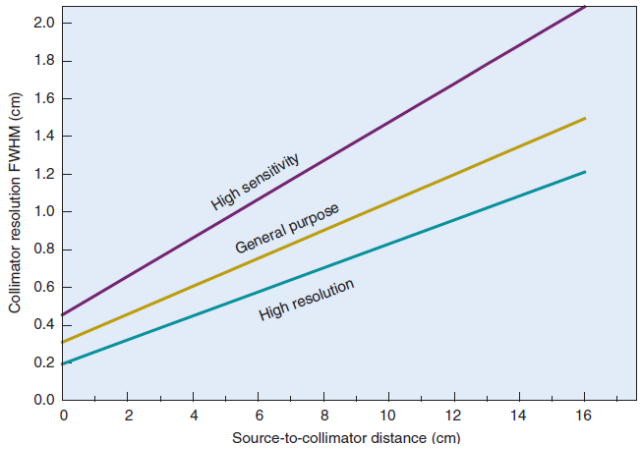


Figure 2.14: Collimators spatial resolution to source-to-collimator distance comparison. Courtesy:Physics in Nuclear Medicine[10]

A surprising thing to take in notice is that while the resolution is strictly dependent on the source-to-collimator distance, the collimator efficiency is instead free from this bond. Indeed, if a radioactive source located in air is moved farther away from the collimator, the efficiency with which radiation is transmitted through any one collimator hole decreases in proportion to $1/b^2$ (inverse-square law), but the number

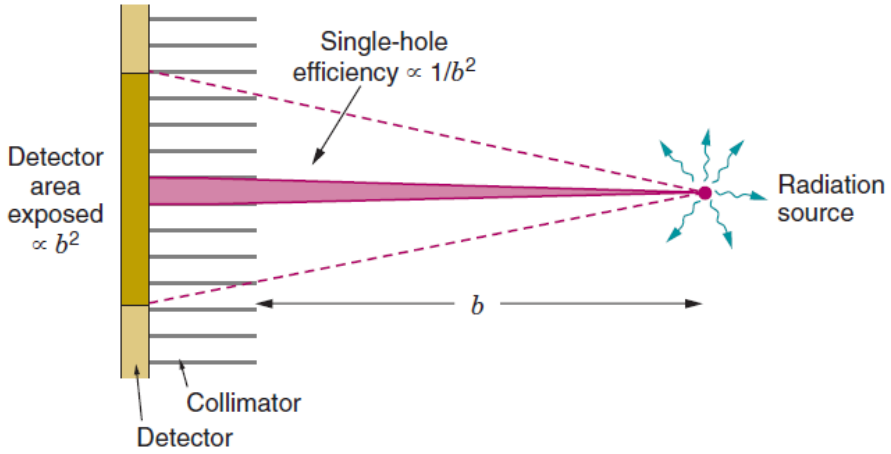


Figure 2.15: Collimator efficiency versus source-to-collimator distance. Courtesy:Physics in Nuclear Medicine[10]

of holes through which radiation can pass to reach the detector increases in proportion to $b^2$. The two effects cancel each other, with the result that total counting rate does not change with source-to-collimator distance as can be seen in Figure 2.15, considering both point, line or uniform sheet source.

## 2.3 Small Animal imaging system

As previously introduced, almost all SPECT imaging system involved the use of a gamma camera to assess the investigation. Typically the gamma camera is mounted on a rotating gantry and is sufficient to acquire two-dimensional (2D) projections images at a equally spaced angular intervals around the patient. The sensitivity of a SPECT system can be improved by incorporating multiple detector heads in the system. Dual headed or three headed systems exist and are widely used. These systems allows to acquire two or three projections at the same time. SPECT imaging system are used not only to investigate the whole body but also to perform investigation focused on specific organs such as the brain and more over the heart. Indeed, one of the most common uses for SPECT is to image the myocardial function. Because in this specific application there is the need to focus on a small FOV dedicated SPECT systems with high sensitivity have been developed.
Next to the wide use of SPECT systems for clinical use, they are also widespread used for small animal imaging applications in biomedical research field. Particularly, they are used for the evaluation of new radio-pharmaceuticals that will be then used for diagnostic purposes, or the evaluation of already existing radio-pharmaceuticals to measure functional, physiologic, or metabolic processes in an animal model to monitor or understand the response to a new therapeutic approach [10].
To perform the *in-vivo* assessment of new radio-pharmaceuticals and to monitor complex biochemical phenomena also x-ray tomographic investigation (CT) and magnetic resonance imaging (MRI) are used. Pre-clinical imaging of small laboratory animals is fundamental because allows to test *in-vivo* several methods and radio-pharmaceuticals not tested on humans yet. In the last decade the combination of different nuclear investigation techniques have been used to asses pre-clinical studies, specially on mice or rats. These kind of imaging systems include SPECT/CT, PET/CT, PET/MRI and others with the advantage of bringing increased data fidelity thanks to a more precise localization if compared to single PET or SPECT devices [36]. These kind of solution however, even if show excellent properties and performance, they also show drawback due to the difficulty in the use of theme and the high cost of maintenance and purchase make them extremely hard to be used as desktop device in a small or medium research laboratory.
For this reason in the last decades there was an increase in the use of planar imaging devices. This kind of device has shown simplicity and good performances resulting as a valuable alternative to tomographic systems [28]. Even if several attempts have been made to produce planar scintigraphic systems, all of them have always shown drawbacks and limitations due to the fact that were prototypes or only experimental one. Furthermore, they showed high costs of maintenance and high purchase cost comparable to that of multimodal imaging systems, with dimensions comparable to them too.

### 2.3.1 BioEmission Technolgy Solutions $\gamma$-Eye$^{\mathbf{TM}}$

An interesting device in this field of research has been proposed by BioEmission Technology Solutions[1], a Greek reality located in Athens. In accordance with the necessity of small and medium research groups, they proposed a planar scintigraphic system of small dimensions and low cost, embracing the needs of the researchers both in terms of system performance and affordability. The system they produced is called "$\gamma$"-eye$^{\mathrm{TM}}$ and is suitable for whole-body mouse static and dynamic imaging

(Figure 2.16), able to provide simple and fast screening of laboratory mice in a cost-effective way [14]. The system they proposed has demonstrated the ability to provide in a cost-effective, fast, and accurate way, a very good indication of the in vivo biodistribution, thus boosting research in drugs/pharmaceuticals, nanoparticles, and other biomolecule development and making the system a really attractive solution for those groups that work with SPECT isotopes, with no or small chance to have access to large multimodal imaging system.

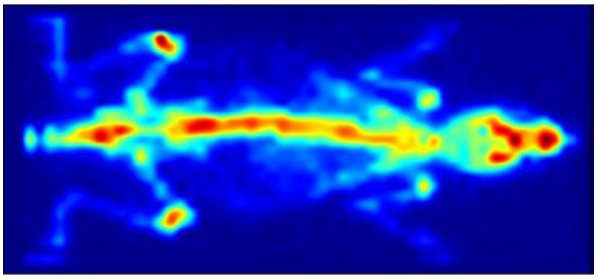

Figure 2.16: Mouse injected with [$^{99}$Tc]MDP at 4 h pi (15-min acquisition time). Courtesy: Georgiou et al.[14]

#### System Improvements

A system like the one presented above is opened to some improvements. These improvements, according to the authors too [14], can be in the forms of a new detectors using crystal pixels with dimensions smaller (1 x 1 mm) than the one already used (1.5 x 1.5 mm), using a monolithic scintillator instead of a pixelated one in order to increase both spatial resolution and sensitivity or change the dimensions and shape of the holes of the collimator used as well as the material itself. Indeed, the collimator used was of a standard design made up of lead with hexagonal holes. The possibility to exploit new materials, such as tungsten, and different shapes for the holes as well as their dimensions could provide an interesting improvement in the system performance.
In particular, this kind of improvement could be achieved nowadays exploiting the possibility offered by the additive manufacturing processes. For this reason, in collaboration with them, we proposed to investigate the application of different additive manufacturing processes in order produce a reliable and cost-effective collimator to be used then on-board of their imaging system.

## 2.4 State of the art and limitations in the production of nuclear medicine collimator

As previously introduced there are available several types of collimators ranging from the most common used the parallel hole, up to the pin-hole, passing through the diverging or converging hole collimators. The type of collimator used is strongly influenced by the investigation the physician want to perform, with particular attention to the ratio between the size of the FOV, the size of the imaging detector and the required spatial resolution and/or sensitivity that the physician is looking for [8].

Every application has its own requirements in terms of sensitivity and spatial resolution. In human whole-body application the resolution results to be less important than that needed in small-animal studies; this carry to the choice of collimators that will have dimensions and geometries that will differ between each other. Contrary, in cardiac imaging the sensitivity result to be much more important than the resolution and so different kind of collimator is needed. The same energy of the radioisotope used strongly influenced the selection of the collimation system. But different design means different geometries and dimensions, sometimes complex and difficult to achieve. Indeed, when designing a collimator it should be considered the difficult that it will be faced with the production process. Different standard manufacturing processes exists nowadays and each of them has its own drawbacks and limitations. Traditional production techniques for the production of parallel-hole, cone-beam or fan beam collimators involves the use of drilling, milling or machining bulky blocks of dense metals, such as lead. Parallel-hole collimator are typically made up by sheets of lead foil, folded in half-hexagonal holes. A huge number of stacked foil then produce the typical honeycomb structure. Some collimators can be manufactured by using molds onto which pour the fused metal. This type of production technique is more precise than the previous one and allows the production of collimator with thinner septa. Typically the minimum septal thickness is 0.15 mm applying these techniques and hole diameter of about 1.2 mm [8]. While these specifications are sufficient for typical clinical investigations, when there is the necessity for very high-resolution collimators smaller holes and septa are required. These specifications can therefore be achievable only by using alternatives production technique like x-ray lithography and metal electroforming, as proposed in the work of Makarova et al [26], that allow the production of very high-accuracy collimators using different metals (e.g. Cu, Ni, Pb, Ag and Au). These two techniques indeed represent a unique method for the production of microstructures with dimensions ranging from several microns to several millimeters with a really high precision. They reached to manufacture three different collimators using gold (40x40 mm size and septa 25 $\mu$m) and copper (64x64 mm size and septa 25 $\mu$m) by stacking layers of these materials together to form the assembly and lead (septa 130 $\mu$m).

The main problem experienced with these techniques is the deposition and the resulting alignment of the layers stacked together. In case the material is the tungsten several problems can arise. First of all the fact that the tungsten, in its pure form, shows a really high melting point making it unable to be used, as lead, in casting techniques. It is also brittle and so difficult to be machined, but tungsten alloys with nickel, iron and/or copper can be used resulting to be valuable for drilling or be machined by electric discharge machining (EDM) [8].

In the last years, next to the traditional manufacturing techniques, it has been stating a new approach in the production of collimators. This approach involves the use of additive manufacturing processes, best known as 3D printing, to produce collimators already working, or molds where to pour fused metal or metal mixture.

An interesting case regarding this last technique is provided by Miller et al.[27]. They used a 3D printer with a technology known as polymer-jetting in order to create molds to be used for casting tungsten powder mixed with epoxy resin or to create lost-wax molds for pin-hole fabrication. This techniques let them producing complex aperture designs, casting pin-hole for high-resolution SPECT imaging systems and producing high-shielding components for gamma-ray and X-ray applications.

However, an increasing number of research groups are converging on the use of additive manufacturing processes to fabricate collimators already ready to be implemented

on a gamma-camera or for x-ray investigation.
An interesting case has been proposed by Deprez et al. [12]. The aim of their work was that of fabricating a complex collimator composed of several pin-holes arranged obliquely. Since the traditional technologies made it really complex, and in some case impossible, to obtain such a geometry, specially when facing with metal like tungsten, they proceeded with metal additive manufacturing technology. They used a technology known as Selective Laser Melting (SLM), where a laser at high power is used to melt the tungsten powder and to fabricate the CAD object. The advantages given by the manufacturing process rely mainly on the possibility to have available custom geometry at a low cost (in this case the cost of the tungsten powder to be used in the printing process) and reduced production time compared to the traditional procedure.
The same additive manufacturing technology has been applied also in other works such as that proposed by Holdsworth et al. [17]. Applying the SLM printing process they fabricated a focused collimator in a dense metal alloy (stainless steel) to be used on a gamma-camera probe for intra-operative gamma-ray detection. The collimator is composed of several circular holes arranged into an hexagonal shape with a measured septa thickness smaller than 250 $\mu$m. Even if the system works well with gamma energy around 59.5 keV the lack of the SLM technology they used, at the time, to print with denser metal (e.g. tungsten) make the collimator difficult to be used with higher energy such as $^{99}$Tc-m that shows an energy peak around 140 keV, making the stainless steel (316L) used quite transparent to the incoming $\gamma$-rays that will penetrate easily the structure. Today the SLM is able to print using tungsten powder but other limitations can arise, specially regarding the price of the printed component and the fact that the tungsten results difficult to be printed, resulting in cracks and pores if not well post-processed [25].
Also other 3D printing metal technology have been used in the last years such the Direct metal laser sintering (DMLS) used to fabricate a collimator for neutron scattering. Indeed, Ridley et al. [30] using this technique were able to fabricate a customized collimator that showed to be able to reduce the limitations of the traditional collimators used in this research field. According to them these collimators showed to be limited in the volume they can focus on, due to difficulties in producing tightly spaced neutron-absorbing foils close to the sample and in integrating this into neutron instruments. They provided a solution to overcome these issues improving at the same time the signal-to-noise ratio.
Another example of use of 3D printing processes for producing collimator is presented by Stone et al. [35] that used a printing technology known as Binder Jetting to fabricate collimator for neutron scattering too. The printing technology works by spreading powdered material into thin layers and depositing a binder onto the layer using an inkjet print head. After the binder is deposited, the build volume drops, additional powder is spread, and the process start again. Collimator for X-ray diffraction have been made too using additive manufacturing processes as proposed by Kowarik et al. [22] using stainless steel.
Georgiou et al.[15] developed a imaging probe for axillary sentinel lymph node mapping called $\lambda$-eye using a 3D printed tungsten collimator. The collimator was provided by LayerWise, showing square holes of 2x2 mm in order to be perfectly matched with the underneath crystal matrix with size 1.9×1.9 mm. But the 3D printing processes can also be used, as we have seen with [27], to fabricate molds.
An example of this technique is offered by Zhu et al.[38] that produced a grid block mold with flared tubes which follow the divergence of the beam. They create the

mold using a printing technology known as Fused deposition modeling (FDM) and using a plastic filament as material known as PLA. They then poured melted Cerrobend (eutectic alloy of 50% bismuth, 26.7% lead, 13.3% tin, and 10% cadmium by weight) liquid into the mold, demonstrating the usefulness of additive manufacturing processes.
Another really interesting example of applying 3D printing processes that involves the fabrication of molds instead of the final object is proposed by Khong et al.[21]. They produced a complex collimator for energy dispersive X-ray diffraction (EDXRD) using an FDM printer and tungsten powder. They proceeded 3D printing a plastic hollow shell that was then filled with tungsten powder. This permitted them to fabricate a geometry otherwise impossible with the traditional production techniques (machining or drilling). A comparison of their collimator with a one 3D printed in tungsten using metal additive manufacturing processes, resulted that both the collimator have significantly the same performance. The filled collimator showed slightly worse peak resolution in momentum transfer, due mainly to X-ray transmission through the plastic walls and the much lower packing fraction of the tungsten powder. However, even if this kind of solution was considered, according to the authors, to be good only for prototyping or for short duration collimators, due to the lower durability of the printed part, it shows to be a promising starting point, specially considering the possibility to easily obtain complex geometry collimators with good measuring performance at a really low cost (£2 for the PLA filament and £23 for tungsten powder) if compared to the same object obtained with metal 3D printer (£2500).
The use of this particular technique has been also investigated by Verdenelli et al.[37]. Starting from the traditional parallel-hole collimator geometry they proposed a complete new geometry concept to be easily fabricated using FDM or Selective Laser Sintering (SLS) printing process, and using then tungsten powder as filling material to recreate the component with the stopping power for radiations.

The production of collimators using the traditional manufacturing processes is sometimes hard to apply and/or non affordable from the production costs of view. These limitations become much more big and sensed when small or medium-research groups, small hospitals or new born companies, such as could be a start-up, need collimation systems showing specific dimensions and geometry or collimator for specific energies. Indeed, sometimes all these professionals need collimators that show excellent performance for the specific investigation they are performing with a specific radio-isotope. However, high costs of producing a single collimator, also using metal additive manufacturing processes as Khong et al. highlighted, make this possibility highly utopian and difficult to realize.
Having available collimators that show performance ad hoc for each single energy that it wants to be investigated is quite impossible approaching the problem with the traditional production technologies. Indeed, this usually lead to the acquisition of one or two collimators that show an average behavior in terms of spatial resolution and sensitivity according to as many isotopes possible.
These limitations can be easily overcame by using alternatives production techniques offered by the additive manufacturing world that permit to achieve high customization levels and a huge reduction both in production costs and waste of materials.

# Chapter 3

# Aims of the work

As previously stated, all those professionals that do not have big budget to use for purchase tomographic multimodal systems for pre-clinical studies, as Georgiou et al. highlighted [14], turn up on gamma camera imaging devices with collimation systems that show an average behavior.
However, could be extremely useful and of great impact having available multiple collimators, at low cost and fully home customizable according to the specific clinical investigation that it want to be performed.
So, starting from the previously discussed limitations of the traditional production techniques in collimators fabrication, and considering also the advantages and drawbacks of using different additive manufacturing technologies nowadays available, with our work we proposed an innovative fabrication strategy to overcome all these limitations by presenting a simple and new approach to the problem.
By using two of the most used additive manufacturing technologies nowadays available such as the Fused Deposition Modeling (FDM) and the Selective Laser Sintering (SLS) **we proceeded to the development of a new concept of parallel-hole collimator design, printing the "negative" of a traditional parallel hole collimator**. This novel concept allows to an easily and fast production, showing a really low cost if compared to the commercial collimator fabricated both with traditional and additive manufacturing processes, but showing at the same time good performance characteristics if compared with a commercial parallel-hole collimator. The proposed idea demonstrates to be not only innovative since the production follow a new concept in the fabrication of this kind of object, but also because it demonstrates also to be highly adaptive to the specific needs.
Parallel to the innovative fabrication idea proposed, **has been also developed an imaging system to be mounted on-board of an FDM printer in order to provide an optimization and a control of the production process itself**. The system has been used to acquire every printed layer of the collimator sample during its production process and then, by means of a python algorithm, the 3D model of the printed collimator has been reconstructed with all its printed errors and distortions. The model has been then used in the numerical simulation campaign in order to see how those distortions and errors (e.g. non-parallelism, dimension errors) will influence the measurement characteristics of the imaging system. We started looking for those additive manufacturing technologies that allowed us to fabricate reliable and accurate prints with low costs. We then defined a numerical simulation campaign in GATE to see if and how the innovative idea of printing the negative of a traditional

collimator using plastic materials was valid and efficient in terms of spatial resolution and sensitivity. We defined several simulations that helped us to proceed with the 3D printing of the novel concept collimator samples and that confirm also the goodness of the imaging system mounted on the FDM printer. The 3D printed samples have been then sent to the BIOEMTECH company in order to be validated also experimentally as it is possible to see later in the chapter dedicated to the experimental results.

# Chapter 4

# Additive manufacturing technologies involved in the novel concept collimator's fabrication

In the last years many research groups have investigated the use of 3D printing processes to develop nuclear imaging collimators, mainly focusing on the use of metal additive manufacturing technologies, with respect to the one that used plastic, with all the advantages and disadvantages they brought with themselves, ranging from the cost of production to the difficult to print with metal powder. But all of them had show that applying this production technology, it was possible not only to overcome the much more higher cost of production with the traditional fabrication techniques, but also that complex geometry before impossible or really though to make were now easily accessible and that there was the need of much more less time for the manufacturing of a single collimator.
Indeed, using additive manufacturing (AM) processes allow to reduce not only the time needed to produce a single object, but also permit to greatly shorten the entire production chain. When using AM we start from a 3D CAD designed at the PC and then the 3D model is simply passed to the AM machine. So, basically we do not have all the intermediate stages that we will incur on if fabricating with the traditional technologies. A simple changing in the design of the object to be printed will result in a easy modification in the CAD file with no problems for the machine at all, thing that instead will produce a huge time expense if made via traditional manufacturing. Furthermore, using AM will produce also a great reduction in wasted materials, ranging from the material itself used for the object to all the intermediate devices needed if fabricated using carving or molding techniques, up to Computerized Numerical Control (CNC) machining. CNC machine are as AM computer based technology but they work for subtraction instead of adding material layer by layer. Furthermore, CNC processes involves more time for the preparation of the machine itself and complex geometry are not always possible.
The most common additive manufacturing technology according to Statista as of July 2018 is the Fused Deposition Modeling (FDM) with 69% of market share, followed by Stereolitography 3D printing (SLA) with 15% and the Selective Laser Sintering

(SLS) with 12%, while material jetting and metal sintering covered both 2% [34].

## 4.1 Fused Deposition Modeling (FDM)

Fused Deposition Modeling (FDM) technology is the worldwide most used additive manufacturing process, specially because it is possible to find solutions on the market that range from few hundreds of euro to some thousands of euro, making it affordable for everyone who wants to start 3D print. Material extrusion technologies involve the construction of the final object by deposition of fused material layer by layer. The working principle of an FDM 3D printer can be easily described as follow:

- Loading the plastic filament (or pellet or powder according to the hot-end technology)
- Liquefy the material
- Application of a specific pressure to push the fused material through the nozzle
- Extrusion of the fused material in the form of a filament
- Printing of the wanted geometry according to the CAD model and GCODE passed to the printer
- Possible post-processing of the printed part

A basic scheme describing the technology can be seen in Figure 4.1

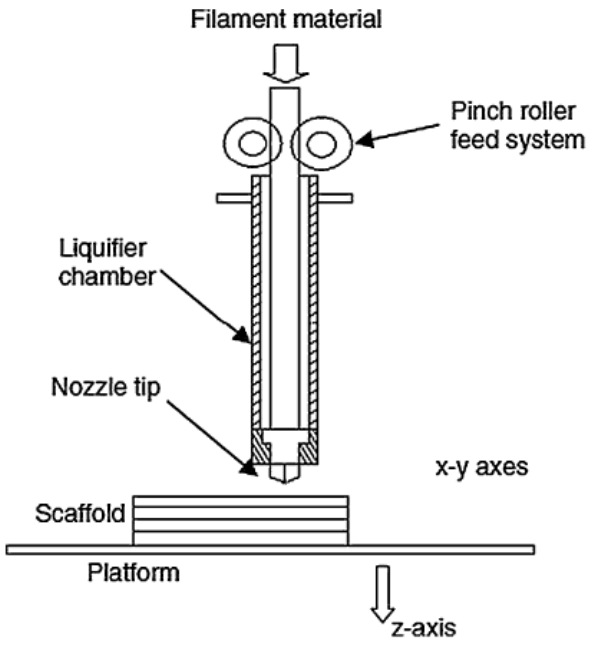


Figure 4.1: FDM working scheme. Courtesy: Additive Manufacturing Technologies

The fused material, typically PLA or ABS, are pushed toward the liquifier chamber

by means of a feed system composed of pinch roller. The temperature to be used with PLA is usually around 190-210 °C while for ABS i a bit higher around 225-230 °C. These rollers are responsible for generating the pressure needed for the extrusion to happen. However, an equilibrium between the pressure generated by the rollers and that provided by the atmosphere outside the nozzle should exist, otherwise if the rollers pressure is higher non-flow or buckling can occur when feeding the material. After the material has been extruded starts the cooling process. The cooling process is quite delicate because if not properly controlled or achieved can lead to deformities or shrinkage of the printed part. Indeed, is quite important that the differential temperature between the chamber and the surrounding atmosphere is maintained to a minimum (e.g. using controlled environmental chamber when building the part)[16]. The temperature of the building bed it's a really import aspect to take in consideration too when considering errors or distortion due to the cooling process. Indeed, it is really important to keep a bed temperature between 50 °C and 80 °C for PLA while, as stated by Choi et al., it should be kept around 100 °C if printing with ABS in order to avoid errors and problems due to shrinkage or warping of the part[11]. This is really important to consider specially for long time printing. The adhesion between the bottom of the printed part and the bed must be as high as possible ensuring that the part do not unglue causing the part to distort or shrink.
The quality of the print in the FDM process is ensured by a series of factors linked together. Typically, the most common parameter that everyone look for when purchasing an FDM 3D printer is the resolution, express in $\mu$m (e.g. 300$\mu$m, 200$\mu$m). But this is only one of the many parameters to look for. Indeed, that resolution typically expressed in the data sheet refers not to the smallest feature that the printer is able to reproduce, but to the resolution in the Z direction. Many times this is not highlighted causing confusion. The resolution in the Z direction regard the minimum thickness reproducible by the printer; smaller the value better will be the print along that axis producing a print where the single layers are not easily distinguishable, producing a smooth surface. Then we got the X-Y resolution. This is quite important since from it depends the dimension of the features printed. The lower the value, the smallest will be the horizontal movement of the extruder in the X and Y plane producing prints with high details. The quality of the movement in the X and Y directions are controlled by stepper motors and their drivers. Better are the drivers and so the stepper motors, better will be the movement performed by the extruder. This is quite important because not all the FD printer mount good stepper motor, specially those of low or mid-range. The printing quality is then strictly dependent also on the nozzle used. Nozzle with diameter of 0.6 mm or 0.8 mm will print parts in a faster way with respect to smaller nozzle diameter, but this will cause parts with lower precision compared to the CAD model. Furthermore, the diameter of the nozzle also determines the minimum features size that can be printed. Indeed, it is not possible to have features smaller that the nozzle diameter. However, FDM printers show some limitations that rely mainly on the printing speed and printing accuracy. The speed can be lowered setting different infill in the pre-slicing setup as well different printing speed or layer thicknesses for example. If someone want a good and accurate part, specially when printing really small features, the extruder speed should be kept as low as possible (e.g. 30 mm/s) and the nozzle diameter used should be smaller as possible (e.g. 0.2 mm or 0.3 mm). As a rule of thumb the layer thickness can be set to be half of the nozzle diameter; this will lead to a smoother surface in Z direction. According to the geometry that is going to be printed, its complexity and quality needed, a lot of several others parameters can be considered and modified to achieve

the best result possible. All these parameters, except for the one depending on the physical hardware such as the quality of the stepper motors, or the quality of the filament that play a really important role in the overall quality of the print (dry filament or filament that have absorbed moisture will behaves differently) as well, can be modified ad adjusted according to expertise and printer specifications directly in the slicer software such as Ultimake Cura or Slicer3D.

## 4.2 Selective Laser Sintering (SLS)

Selective laser sintering (SLS) is, with the FDM and Stereolitography (SLA), oone of the most used 3D printing technology. Its technology is based on a process called Power bed fusion (PBF) and different materials can be used ranging from polymer one to metallic powder and finishing with ceramic composite.
The polymer SLS process involves the use of thermoplastic materials that can be easily fused due to their relatively low melting temperatures, low thermal conductivity, and low tendency for balling phenomena. The most common and widely used polymer in SLS is the polyamide also known as nylon or PA2200. A given amount of laser energy will melt a certain amount of powder; the melted powder fuses and cools quickly, forming part of a cross section[16].

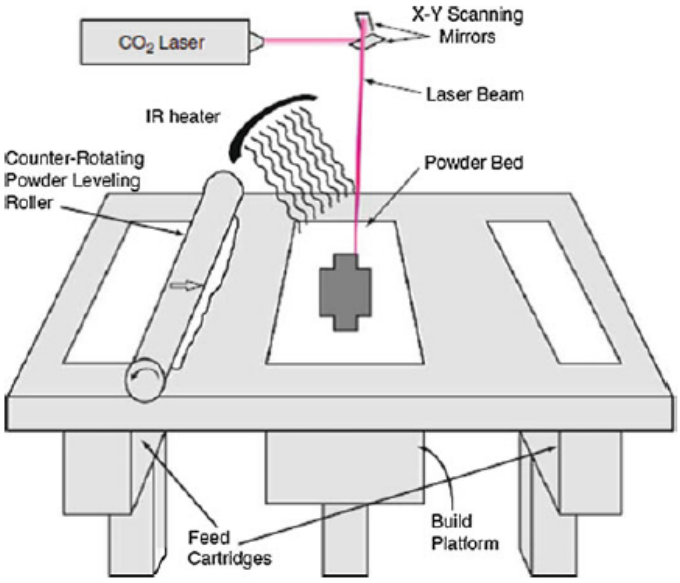


Figure 4.2: SLS working scheme. Courtesy: Additive Manufacturing Technologies

The printing process takes place inside a chamber hermetically closed and inside which is placed nitrogen gas used to avoid degradation and oxidation of the powder. The powder placed on the building platform is maintained at an elevated temperature just below its melting point and a series of infrared heaters are placed above the build platform to maintain an elevated temperature around the part being printed, as well as above the feed cartridges to preheat the powder prior to spreading over the build area[16]. Some machines have also the building platform heated up. The powder preheating has a double function. The first is that it is used in order to use less laser

energy to fuse the material and secondly because, as for the FDM process, having a preheated powder and building platform will greatly reduce the warping defects durinig the part building.
Once a layer of powder has been heated and formed, a focused $CO_2$ laser beam, moved by means of galvanometers, is directed onto the powder bed and moved in such a way to form a cross section according to the CAD model. The surrounding powder remaining non-fused serves as support for subsequent layers, avoiding in this way the need of specific support like for the FDM or SLA process. At the end of the printing process the part should left cooling down sufficiently in order to not incur in warping due to differential temperature between chamber and atmosphere or degradation due to a premature exposure to the ambient atmosphere that can degrade the material.
SLS technology allow to reach higher quality print with respect to the FDM, with resolution that depends mainly from the laser spot and galvanometers. Typically, a layer thickness of about $10\mu$m are achievable with this technology.

These are two of the most used 3D printing technologies nowadays used worldwide. According to the need someone could choose the FDM because for a single object the printing process is cheaper and quicker than the SLS, but in the case that many part of the same CAD model are needed the SLS become the first choice because the price per unit fall down as also highlighted by Kudelski et al[23]. If the need instead is the quality of the print and its usability, the SLS should therefore be the first choice regardless the higher price if only one printed object is required. Indeed, the FDM is a technology used more for prototyping than obtaining functional parts, and the quality that it can achieve is much lower than that achieved by the SLS process.

# Chapter 5

# Numerical Simulations

The collimator novel concept has been numerically simulated by means of a dedicated software (GATE) where it is possible to define all the measurement chain, from the collimator to the electronics, of medical imaging device such as a gamma camera. The gamma camera electronics and configuration was the one replicating the configuration of the working gamma camera by BIOEMTECH Technology Solutions.

## 5.1 What is GATE

GATE is an open-source software developed by the international OpenGATE collaboration with advanced toolkit dedicated to numerical simulations in medical imaging and radiotherapy. Using GATE is possible to simulate several nuclear medicine experiments and device ranging from simulations for Emission Tomography (Positron Emission Tomography - PET and Single Photon Emission Computed Tomography - SPECT), Computed Tomography (CT), Optical Imaging (Bioluminescence and Fluorescence) and Radiotherapy experiments.[19] [33] [18] [32] The language used to code the experiments is based on easy macro mechanism that can be used to configure and setting up different experiments, simple or extremely complicated from the physics point of view.
GATE plays a decisive role in the design and definition of the medical imaging devices, in the study of new radio-pharmaceuticals used for pre-clinical studies or for dose calculation in radiation therapy.

## 5.2 BIOEMTECH Gamma Camera

The gamma camera configuration considered for the numerical simulations is the one reproducing the electronic of the imaging device the BIOEMTECH $\gamma$-eye$^{\mathrm{TM}}$. The gamma camera mounted a collimator of dimension 105x55x45 mm in the first configuration while a 105x55x30 mm in the optimized configuration. The crystal box was composed of 29x58 CsI(Na) crystals with dimension of 1.5x1.5x6 mm spaced with 0.2 mm septa. A glass windows of 2.5 mm thick was used and it is composed of two position sensitive photo-multiplier tubes.

## 5.3 Collimator's configurations simulated

Considering the BIOEMTECH $\gamma$-eye$^{TM}$ hardware chain configuration we proceeded modifying the collimator they had with the one proposed and investigated in our work. We numerically simulated six different 3D printed collimators, three for the first concept and three regarding the new optimized concept. The simulation we did consider the actual dimension, length and width, of the collimator it is mounted on the working device (105x55mm).

### 5.3.1 Standard geometry

Before simulating the new concept collimators we proceeded with some standard geometries in order to have data of reference to which compare the novel collimators concept. Considering the first concept we firstly simulate a geometry where the square pixels were 1.5x1.5 mm$^2$ big and 45 mm in length and spaced by 0.2 mm of septa (5.1(b)). We decided to test this condition because in this case we were perfectly matched with the underneath crystals that have that exactly dimension. Being matched with collimators holes and crystals allows us to see how much the spatial resolution and sensitivity of the imaging system improve with respect to a condition where they are not matched. Indeed, having a simulation with these characteristics allows us to see how, increasing the septa to 0.4 mm, to simplify the manufacturing procedure, influences the sensitivity and spatial resolution of the system.
In Figure 5.1(a) is presented a standard hexagonal parallel hole collimator, simulated in GATE, and it is immediately clear that such a pattern tends to cut out, by means of the septa, a lot of active surface of the underneath crystals, causing a loss in terms of incoming photons records. In GATE the the collimator holes material has been set

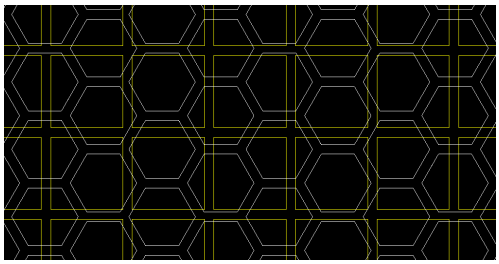

(a)

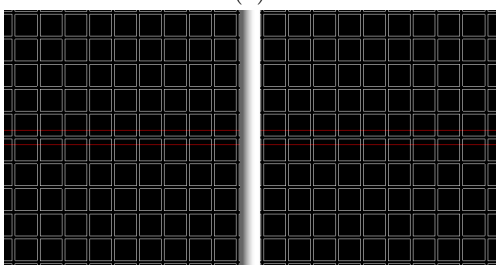

(b)

Figure 5.1: Top view of the standard hexagonal hole collimator(a), top view of the square hole collimator close-up(b)

as air like it is in a standard collimator. Instead the material surrounding the holes was set as tungsten. Doing so we simulated a standard parallel hole collimator to be used as reference.
A standard geometry has been simulated also with the optimized geometry. In this case the hole dimension and the septa thickness were, since the beginning, bigger than the crystals dimension and spacing. For this reason, even if we used again the square shape, the hole are no more matched with the underneath crystal matrix. This can be seen in Figure 5.2.

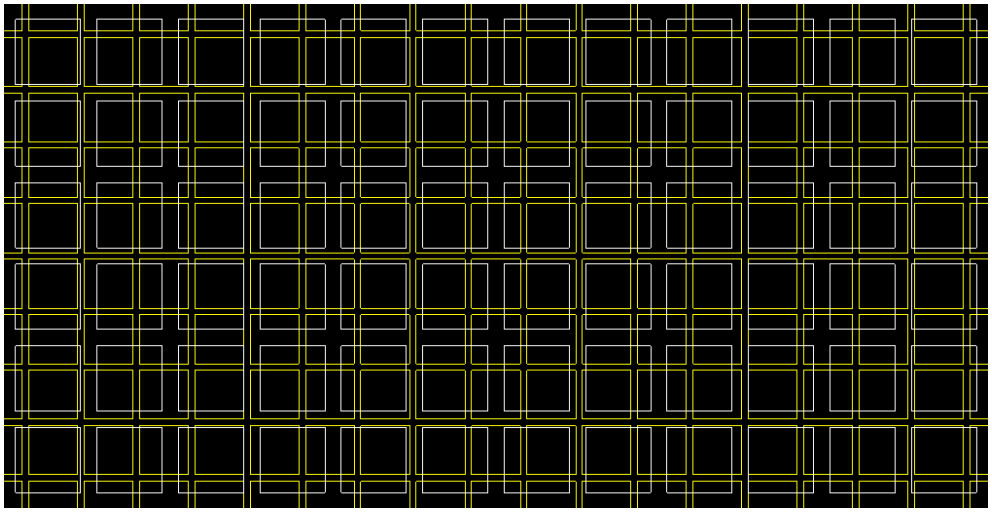

Figure 5.2: Top view of the optimized concept 2x2mm and 0.5mm septa

Also in this case the holes material has set to air and the surrounding material as tungsten. A reference geometry (extruded septa)(Figure 5.3) has been also simulated for the configuration used for the first collimator concept, where we increased the septa up to 0.4 mm.

In addition to the standard configuration where the tungsten has been used has surrounding material to create the element with stopping power for the incoming radiation that travel obliquely, we simulated also an additional material. The material we simulated is the one provided by Virtual Foundry [13] that is a PLA loaded with 95% in weight of tungsten powder. We did this in order to have an idea of its efficiency in terms of spatial resolution and sensitivity if compared to the standard tungsten. The material has a density around 8 g/cm$^3$

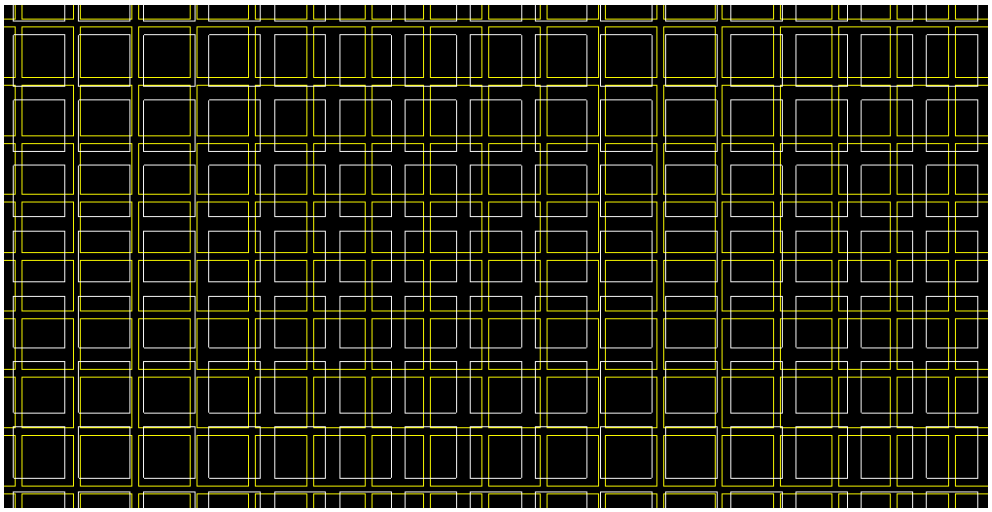

Figure 5.3: Top view of the first concept 1.5x1.5mm and 0.4mm septa

### 5.3.2 First novel concept geometries

We then proceeded to simulate the novel geometry with the extruded holes. The first concept showed the same height of the reference collimator but changed in septa thickness. Indeed, due to printing limitations we decided in accordance also with BIOEMTECH, to increase the septa thickness up to 0.4 mm in order to have more freedom with the additive manufacturing process. Again, as for the optimized concept, also here increasing the septa thickness make us loose the matching advantage we previously got. In this case the holes material has been set to PLA with the same density of the material used for the printing process (1.24 g/cm$^3$). In this case we wanted to simulate the collimator sample 3D printed using the FDM additive manufacturing process.
Then we changed the hole material to PA2200 that is an industrial Nylon with a density $\sim$0.95 g/cm$^3$ and leaving the surrounding material to tungsten. We mimic in this way the collimator sample 3D printed by PROSILAS using the SLS printing technology.

Numerically, simulating the materials we used in the additive manufacturing processes allows us to understand if the material used has properties suitable for the purpose of the pre-clincal investigation. Particularly, what we wanted to see was the effect the plastic materials would have had on the sensitivity of the imaging system. Indeed, having a density much higher than the air we expected a decrease in sensitivity.
We also simulated the collimator 3D printed by M.A.D.E where the grid in PLA was placed at half of its height. We did this simulation in order to see how and if the grid influenced the spatial resolution and sensitivity of the system.

### 5.3.3 Optimized novel geometries

After the numerical simulations with the simulated geometries for the first concept collimator have been done, we proceeded in collaboration with BIOEMTECH Tech-

nology Solutions to optimize the geometry. The optimized geometry has been then numerically simulated as for the previous concept changing time by time the material of the holes. The materials used were always PLA and PA2200.
In GATE we maintain the same electronics and physics of the previous simulation going to change only the collimator holes, septa and height that now is 30 mm and no more 45 mm.

### 5.3.4 Geometry from 3D printer imaging system

Finally we proceeded to simulate also the 3D model obtained with the imaging system mounted on-board of the Ender 5 Plus FDM printer. We import the STL file of the model into GATE and we set the material of the model to PLA. The model is only a portion of the real collimator, as it is possible to see later. This means that we got a lower value for the sensitivity due to the fact that it actually cover a much small area of the crystal matrix and so less photons have been recorder. However, this simulation allows us to see how the actual printed object with all its defects will behaves in terms of spatial resolution and sensitivity.

## 5.4 GATE simulations configurations

As already introduced previously in the chapter, the gamma-camera, electronics, and configuration simulated in GATE refers to the one used in the $\gamma$-eye$^{TM}$ system at BIOEMTECH Technology Solutions. We simulated both the first collimator concept (1.5x1.5x45 mm and 0.4 mm septa) and the optimized concept (2x2x30 mm and 0.5 mm septa).
The simulations configurations have been defined as follow for the FIRST NOVEL COLLIMATOR CONCEPT:

- Square hole, 1.5x1.5x45 mm and 0.2 mm septa, **material**: real tungsten, extruded septa (**standard geometry**)
- Square hole, 1.5x1.5x45 mm and 0.4 mm septa, **material**: real tungsten, extruded septa (**standard geometry**)
- Square hole, 1.5x1.5x45 mm and 0.4 mm septa, **material**: PLA loaded with tungsten, extruded septa (**standard geometry**)
- Square hole, 1.5x1.5x45 mm and 0.4 mm septa, **material**: real tungsten for septa and PLA for extruded holes (**novel concept**)
- Square hole, 1.5x1.5x45 mm and 0.4 mm septa, **material**: real tungsten for septa and PA2200 for extruded holes (**novel concept**)
- Square hole, 1.5x1.5x45 mm and 0.4 mm septa, **material**: real tungsten for septa and PLA for extruded holes (**novel concept M.A.D.E**)

We then simulated the following configurations for the OPTIMIZED NOVEL GEOMETRIES:

- Square hole, 2x2x30 mm and 0.5 mm septa, **material**: real tungsten, extruded septa (**standard geometry**)
- Square hole, 2x2x30 mm and 0.5 mm septa, **material**: real tungsten for septa and PLA for extruded holes (**novel concept**)
- Square hole, 2x2x30 mm and 0.5 mm septa, **material**: real tungsten for septa and PA2200 for extruded holes (**novel concept**)

### 5.4.1 Spatial resolution: simulation strategy

A capillary source have been used for the calculation of the spatial resolution. The capillary is 60 mm in length and has an outer diameter of 1.4 mm and an inner diameter 0.6 mm, filled with 6,2 MBq of $^{99}$Tc solution. The capillary has been placed at different distance (5-30 mm) from the collimator surface to assess system's spatial resolution and sensitivity. $^{99}$Tc has been used as radioisotope in the simulations done with the first collimator concept. The optimized concept instead has been evaluated also considering higher energy isotopes such as Lu177, In111 and Ga67. Indeed, the optimized geometry has better characteristics for the evaluation of these higher isotopes used in pre-clinical studies. Bigger holes and thicker septa allow to increase the efficiency of the collimator making them "high-sensitivity" collimators. The full width at half-maximum (FWHM) of the capillary source using Gaussian fit has been calculated. FWHM values (mm) were extracted by multiplying the variance of the distribution $\sigma$ with 2.35. The numerical simulations have been acquired for 30 s.

### 5.4.2 Sensitivity calculation

Sensitivity has been computed considering all the counts after applying the energy window ($\pm$20%) on the reference energy spectrum peak. The sensitivity is expressed as cps/MBq.

# Chapter 6

# Innovative collimator production concept in Additive Manufacturing

After the simulations have confirmed the goodness of the proposed idea we proceeded to the fabrication of the novel concept collimator by means of the two previously described additive manufacturing technologies, the FDM and SLS.
The innovative concept born as a consequence of the investigated limitations and advantages of the different additive manufacturing processes. Due to the elevated costs of a metal additive technology and its limitations in the use of tungsten powder it has been decided to avoid the use of such of fabrication technology. We moved towards something that was more affordable, easy to use in every day laboratory, and that could produce part at a reasonable price with respect to the traditional manufacturing techniques and metal additive manufacturing processes itself, that as we know show really high costs of production.
The collimator design and geometries have been defined in accordance with the BioEmission Technology Solution, based in Athens, with which we collaborated for this project. The new collimator has been defined after have seen and studied the traditional collimator that the scintigraphic system of the BIOEMTECH, $\gamma$-eye$^{TM}$, had on-board. The collimator was a traditional parallel hole lead collimator of 105x55 mm and 45 mm height, with hexagonal hole of 1,2 mm of diameter and spaced with a septa of 0,2 mm.
So, starting from the collimator geometry that was already mounted on the gamma camera and according to limitations imposed by the 3D printers used, we created a new geometry easily printable with these two manufacturing technologies.

## 6.1 Novel concept collimator and geometries

The limitations imposed by the additive manufacturing technologies used in this fabrication process, forced us to re-invent the parallel hole collimator. The first aspect we considered in this re-invention process concerned the material. Typically, the most common used material in the FDM process is the polylactic acid (PLA) in the form of extruded filament. This material shows a melting temperature around 180$^{\circ}$C up to 210$^{\circ}$C. Above this temperature the PLA start to burn and its mechanical properties

to loose. At the beginning we explored also some innovative materials proposed by the market. We found a valuable material called Rapid 3DShield Tungsten Filament [13] , from the Virtual Foundry company. This material is a PLA loaded with tungsten powder, containing between 92-95 % of metal component in weight, showing a density around 8g/cm$^3$. The filament is certified to be printed with any commercial FDM printer but only using nozzle with a minimum diameter of 0.4 mm and setting an extrusion of 225$^{\circ}$C and is also tested to be valuable for shielding the X-ray and gamma-ray.
So, we first decided to try printing the traditional collimator with this material. From the geometry of the collimator,at the time, on-board of the $\gamma$-eye$^{\text{TM}}$, we changed only the hole shape, from hexagonal to square in order to cover a larger area of the underneath detector. At the time the hole diameter of the collimator was 1.2 mm in diameter and separated by 0.2 mm septa. These showed to be really challenging specifications to be overcame using traditional FDM process using the Rapid 3DShield Tungsten Filament. Indeed, in order to be able to print holes with that dimension it was mandatory to use nozzle with diameter of 0.2 mm. However, this dimension, according to the dealer, and to the tests performed by us, resulted too small for printing the PLA loaded with tungsten, as well the 0.3 mm too, even if we were able to print with it for a little time with really high difficult (due to hole and septa dimensions) as can be seen in Figure 6.1. Furthermore, the material resulted too difficult to be

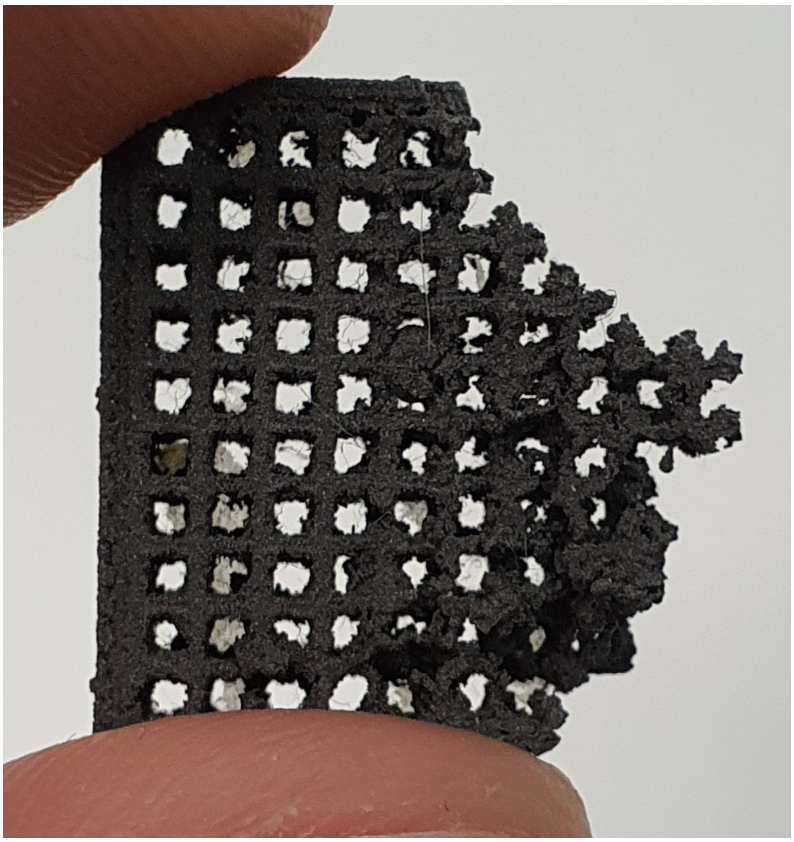

Figure 6.1: Rapid 3DShield Tungsten Filament collimator first printing attempt

printed also with bigger nozzle due to problem linked with its high meting temperature and to the fact that sometimes created clots along the extruder channel causing the filament to stop to be printed.
The difficult in printing holes and septa with the traditional dimensions using FDM processes and with materials valuable for the purpose of the work, pushed us in accordance with the BIOEMTECH, to reconsider the collimator geometry. The first thing we changed was the hole dimension passing from 1.2 mm to 1.5 mm. In this way we were more free to print using the 0.3 mm nozzle that guarantee a better flow of the extruded filament with respect to the 0.2 mm nozzle. The septa also has been modified up to 0.4 mm, while the height of the collimator has been left the same (45 mm). The new geometric parameters have been initially numerically tested in GATE software, in order to see how these new values and the new shape of the hole influenced the measurement characteristics of the imaging system, comparing the results, as we will see later in the results chapter, with the numerical and experimental data from the parallel hexagonal hole collimator on-board of the $\gamma$-eye$^{TM}$. Since, the results showed a good behavior of the new specification for septa and hole, we proceeded with them. The next step involved the overcome of the main problem, the material.
As we know a collimator in order to fulfill its aim letting pass only those photons that travel parallel with the holes, and blocking those that instead travel obliquely trying to penetrate the septa, needs to be made of dense metal (lead or tungsten). However, in accordance with the aforementioned problems linked to the FDM process as well for the SLS one, we proposed a simple as well innovative solution to the problem printing the "negative" of the traditional collimator.
What does it mean printing the negative of a traditional collimation system? It simply mean that instead of printing the septa extruded using metal material, we extrude the hole leaving the septa empty in order to be then filled with metal powder after the printing process done. This simple, but quite innovative solution, allowed us to use additive manufacturing technologies easily accessible and with low costs of maintenance and production if compared with metal 3D printing processes. The extrusion of the holes was possible without affecting in a compromising way the measurement characteristics of the imaging system because the density both of the PLA, used in the FDM process, and of the PA2200 (Nylon), used in the SLS process, is really low, respectively 1,24 g/cm$^3$ for PLA and around 0,95 g/cm$^3$ for the PA2200. Their density has been proved numerically to not degrade the spatial resolution of the imaging system, as we will see later, affecting only the sensitivity, in a small percentage, with respect to the traditional configuration of the collimator where the hole are empty and there is air (density = 0,00129 g/cm$^3$) instead of plastic material.

In Figure 6.2 it is possible to see the CAD model of the first collimator concept. The concept represents only a portion of the real collimator dimension (105x55x45 mm) because it is sufficient to test and validate the goodness of the proposed idea. In this way we were able to waste less material and at same time having available more printed part faster at a low cost. A bottom base has been created, larger than the area occupied by the extruded pixels, in order to have a support base for the case printed using the Rapid 3DShield Tungsten Filament. A base at the top has been created in order to guarantee stability between the extruded pixels avoiding the possibility that they break up due to the arrow created by the movement of the extruder. In Figure 6.3 it is possible to see a representation of the bending momentum. In our FDM process we didn't need the insertion of any grid at half of the CAD model, as instead we will see in an other concept printed in collaboration with MADE in order to avoid

the probability of an arrow, causing the flexion and consequently breaks of the pixel, due to the movement of the extruder traveling from one pixel to the neighbor pixel.

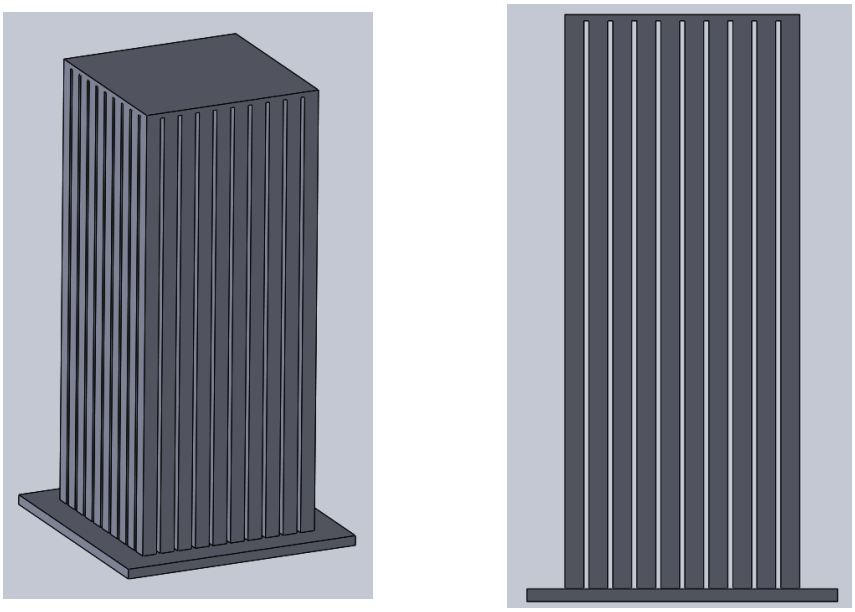

(a) (b)

Figure 6.2: First concept collimator CAD

### 6.1.1 First Collimator concept PLA-UNIVPM

In Figure 6.4 it is shown the collimator 3D printed using the ENDER 5 PLUS printer, supplied to our laboratory at the Department of Industrial Engineering and Mathematical Sciences (DIISM) at the Polytechnic University of Marche (UNIVPM). The nozzle diameter was 0.3 mm, the layer thickness was 0.2 mm and the printing speed was slowed down to 30 mm/s. The printing temperature was set to 210°C and the bed temperature at 60°C and the material used was a standard PLA filament.
The FDM process carried on with the ENDER 5 PLUS 3D printer, even if using all the properly parameters for the case, oozed some PLA during the traveling of the extruder, going to create a sort of webs, visible between the pixels in Figure 6.4 (b), that worked as supporting structure avoiding the above mentioned problem of the bending momentum.

The lack of cleanliness due to the presence of webs of the melted PLA between the pixels, make the filling procedure quite challenging. The printed part has been weighted before filling the empty space with tungsten powder and resulted to have a weight of 10,02 g. A phase of the filling procedure can be seen in Figure 6.5 (a) while in Figure 6.5 (b) it is possible to see a Scanning Electron Microscope (SEM) image of the tungsten powder. We did a SEM acquisition in order to confirm the dimension of the metal particle declared in the data sheet and it was confirmed that they have an average particle size of about 6 $\mu$m. The filling procedure consisted in the dispersion

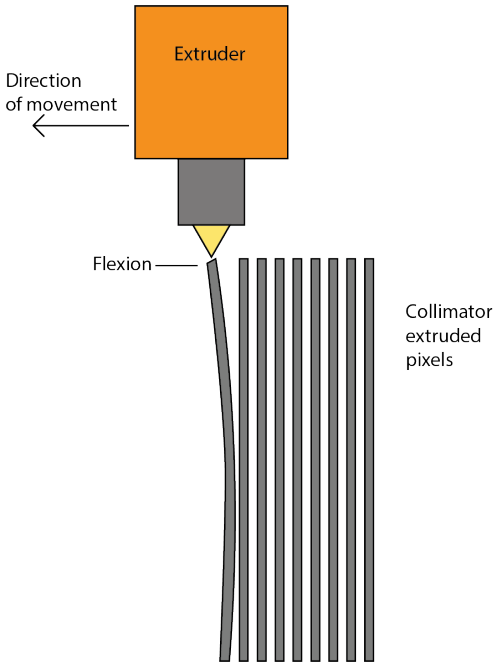


Figure 6.3: Flexion of the pixel due to the movement of the extruder

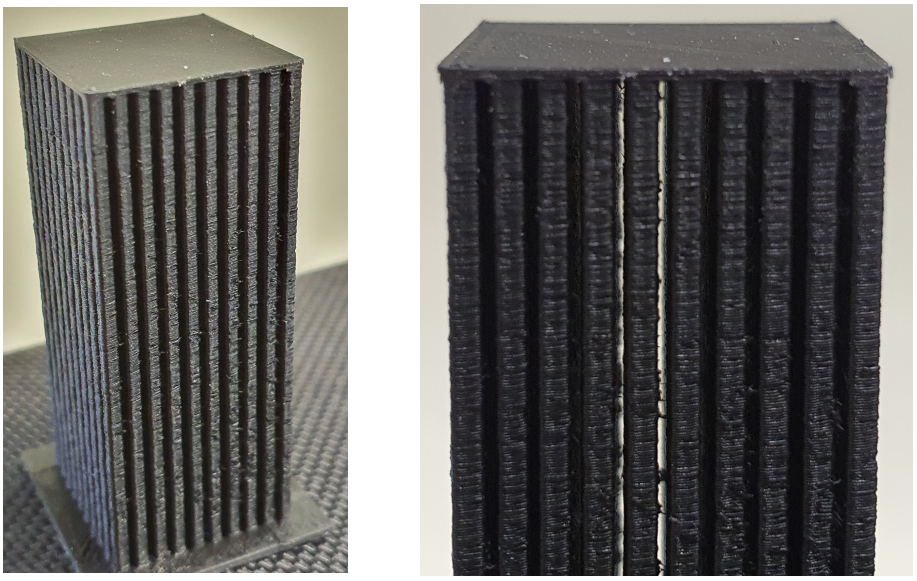

(a) (b)

Figure 6.4: PLA-UNIVPM 3D printed collimator

of a little of tungsten powder (Werth-Metall) between the empty septa and manually shaking the sample in order to homogeneously disperse the powder between all the empty space, as much as possible. This procedure has been replicated until the pow-

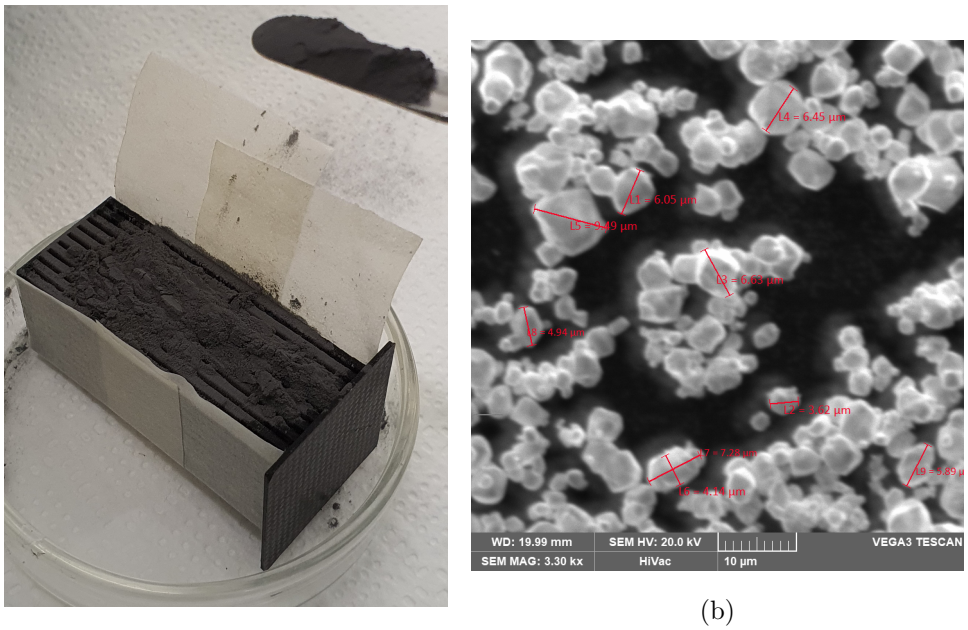


(a) (b)

Figure 6.5: PLA-UNIVPM filling process (a), SEM tungsten powder(b)

der seemed to have filled up all the empty space, as can be seen in Figure 6.6.

Figure 6.6: PLA-UNIVPM filled with tungsten powder

Unfortunately, even if looking at Figure 6.6 the tungsten powder seems perfectly dis-

tributed filling all the empty space, weighting the sample resulted that it weight only 41,83g, meaning that we filled up with only ∼31,81 g of tungsten powder on ∼104,99 g that we would have, reaching only ∼30% of its real filling. Failure to completely fill up the empty space (septa) with the needed tungsten powder it is attributable to the difficulties to properly distribute the powder and properly compress it to remove all the air particles trapped between the metal powder particles. After filled up the collimator sample, few CT images have been acquired to see how the tungsten powder was dispersed between the extruded septa and this allowed us also to verify experimentally, even if only using at first X-rays, the goodness of the idea proposed. In Figure 6.7 it is possible to see two different views of the PLA-UNIVPM collimator viewed at X-rays.

As it is possible to see in Figure 6.7(a) the filling process, that at first sight looked

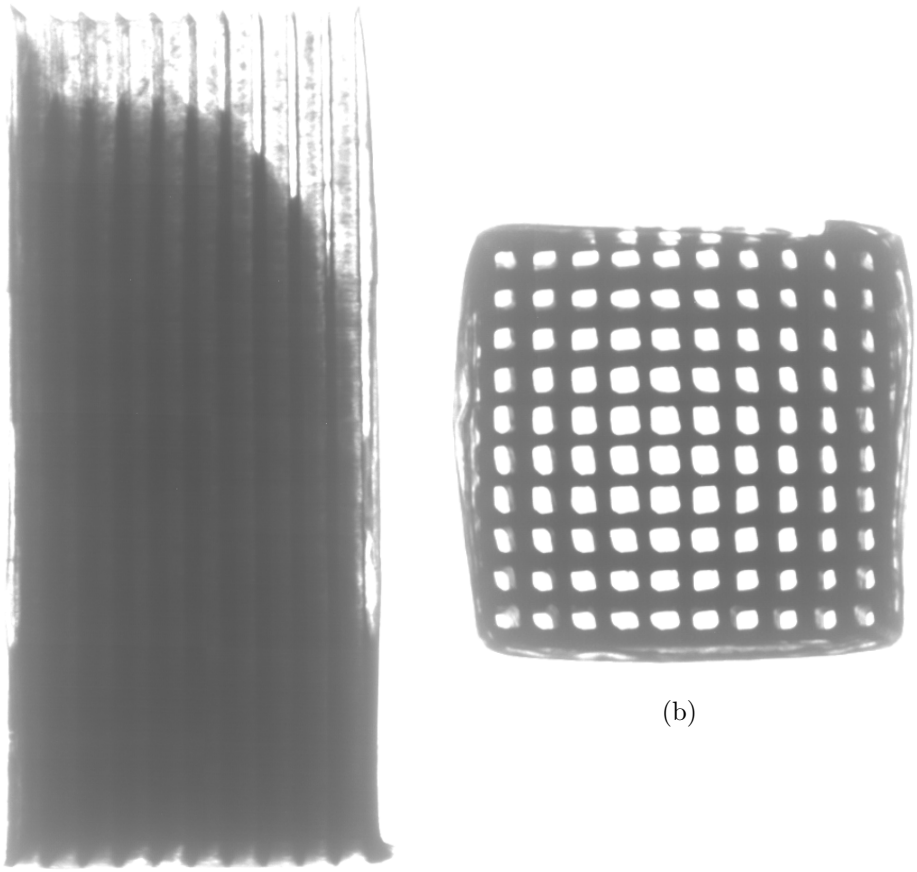

(a) (b)

Figure 6.7: PLA-UNIVPM CT side view (a), PLA-UNIVPM CT top view(b)

good, was in reality non complete at all as the deduced after weighting the sample. The area were no tungsten powder is present at all can be alleged to the presence of the dirty due to PLA webs between the extruded pixels that blocked the dispersion of material and to the difficulty in manually shaking the sample to homogeneously

disperse the powder in such small space. Figure 6.7(b) reports another view of the PLA-UNIVPM collimator placed orthogonally with its top face to the X-ray source. This view allowed us to determine if the radiation was able to pass through the extruded plastic pixels without being absorbed. Effectively the radiation traveled without being absorbed and the tungsten powder between the pixels is able to fulfill the blocking effects, absorbing the impinging radiation.

### 6.1.2 First Collimator concept PA2200-PROSILAS

Next to the collimator printed using the FDM printer supplied to our laboratory, we printed one using an SLS 3D printer from Prosilas Rapid Prototyping[6]. They have available different additive manufacturing technologies (FDM, SLS, SLA and DMLS), but due to the particularity of the object to be printed, the best solution wa the SLS technology, both in terms of production costs and material. The CAD model supplied to the Prosilas was the same used by us with the Ender 5 Plus, and the material used is a PA2200, a nylon for industry. In Figure 6.8 the 3D printed collimator sample is shown. The higher accuracy and precision of the SLS production technology allowed to have available a quite perfect 3D printed object. As it is possible to see from the images below between the septa no material left by the printing process is present creating those webs as occurred in the FDM sample.

We also didn't experience any bending moment because the system as already

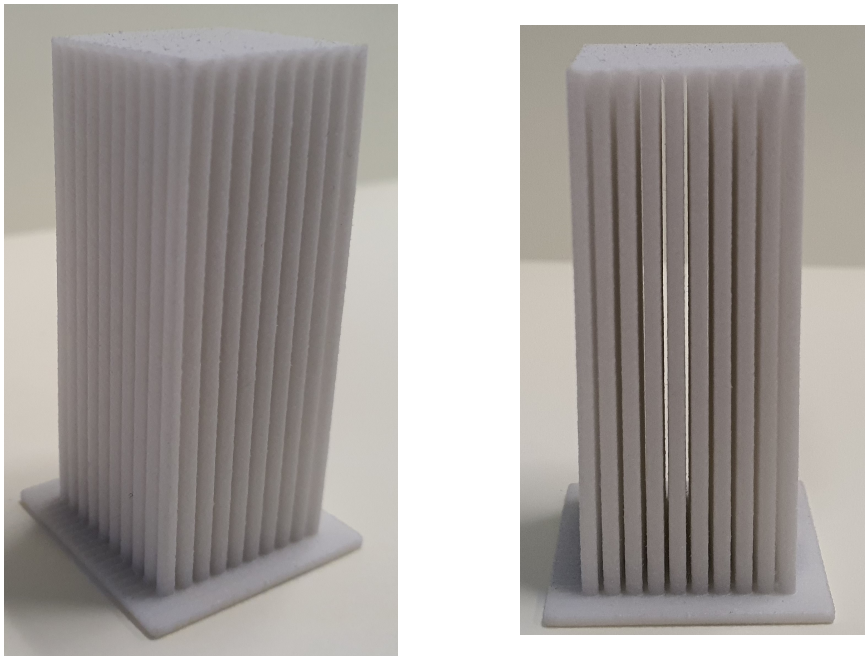

(a) (b)

Figure 6.8: SLS-PROSILAS 3D printed collimator

explained use a laser to fuse the powder and build the part. Furthermore, the powder not fused by the laser spot works as supporting material for the built parts, eliminating the necessity to build supporting structure allowing the printing also of parts that

with other manufacturing techniques (FDM in primis) would need supports to sustain themselves.
The cleanliness of the printing part allows the procedure of filling with the tungsten powder more easy to accomplish, even if the filling procedure is the most important aspect to upgrade due to the limitations of manual filling. In Figure 6.9 the filling up of the SLS-PROSILAS sample is shown. Here too we experienced difficulty in the filling process even if the sample was really clean. The weight of the empty SLS

Figure 6.9: PA2200-PROSILAS filling process

sample was 9,25g and after the filling process we reached 49,16g. We reached to fill the sample with only ∼39,91g of powder on ∼104,99g that it should be, reaching only ∼38% of the expected filling. The cleanliness of the printed part allowed to obtain a better dispersion of the tungsten powder with respect to the sample printed with the FDM process, but the difficulty in the homogeneously dispersion of the powder and the shaking procedure remain. Figure 6.10 shows the SLS sample observed with X-rays. Looking at Figure 6.10(a) it is possible to see how the powder is better dispersed with respect to the FDM sample, but some empty space still remain in addition to the empty space caused by the trapped air particles among the tungsten powder particles itself.
Figure 6.10(b) demonstrates that the PA2200 material of which the extruded pixels are made does not affect the transmission of the radiation letting it pass trough without been absorbed. Looking at this figure and comparing it with Figure 6.7(b) it is possible also to appreciate the printing difference using the FDM Ender 5 Plus and

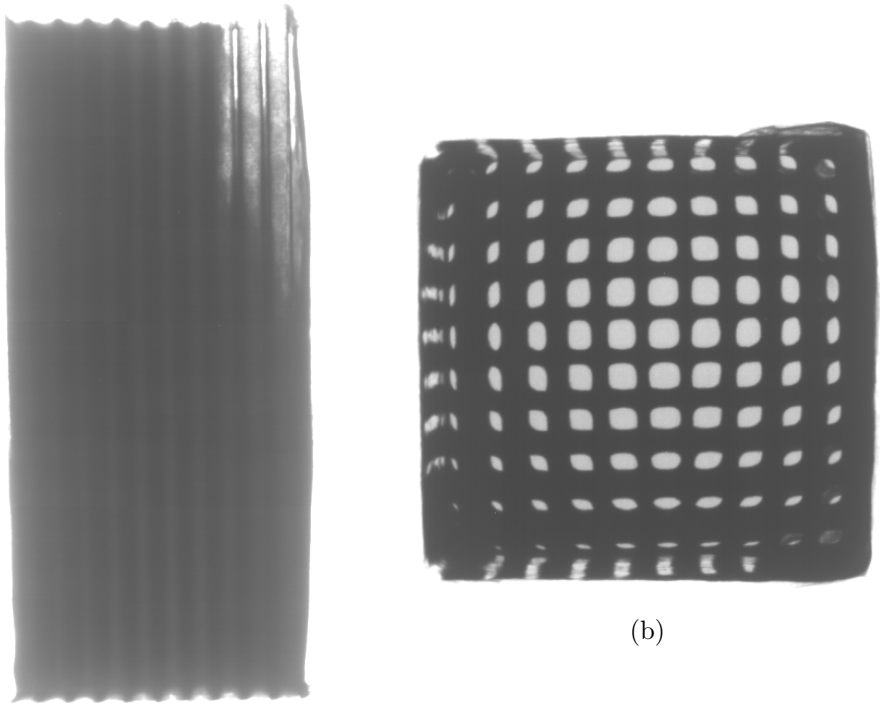

(a) (b)

Figure 6.10: PA2200-PROSILAS CT side view (a), PA2200-PROSILAS CT top view (b)

the SLS 3D printer by PROSILAS with regards to the square section of the extruded pixels.

### 6.1.3 First Collimator concept PLA-M.A.D.E Concept

As previously introduced we printed a third sample of this first concept of collimator in collaboration with an Italian reality called M.A.D.E Concept srl. They are a Spin-off of University Mediterranea of Reggio Calabria with a big know-how on additive manufacturing technologies, specially with regards to the FDM processes. The FDM printer they used to fabricate this first concept is an Original Prusa model I3 MK3S+, with excellent stepper motor able to provide the smallest movement of the extruder with really high precision and accuracy. The so fabricated sample can be seen in Figure 6.11. The collimator has been printed using PLA as material, but due to the elevated quality of the extruder motion and the quality of the printer overall, the printed sample was subjected to the bending moment problem lacking of the PLA webs that in our case worked as supporting material between the extruded pixels. In order to avoid this problem a small grid (0,3 mm thick) has been placed at half height of the part as can be seen in Figure 6.12. In this way, once the extruder reached to print and pass the half of the CAD model the 3D printed part worked as the PLA webs left by our 3D printer, supporting the extruded pixels and eliminating the bending moment that would cause the rupture of the pixels.

The collimator has been then filled up with the tungsten powder following the

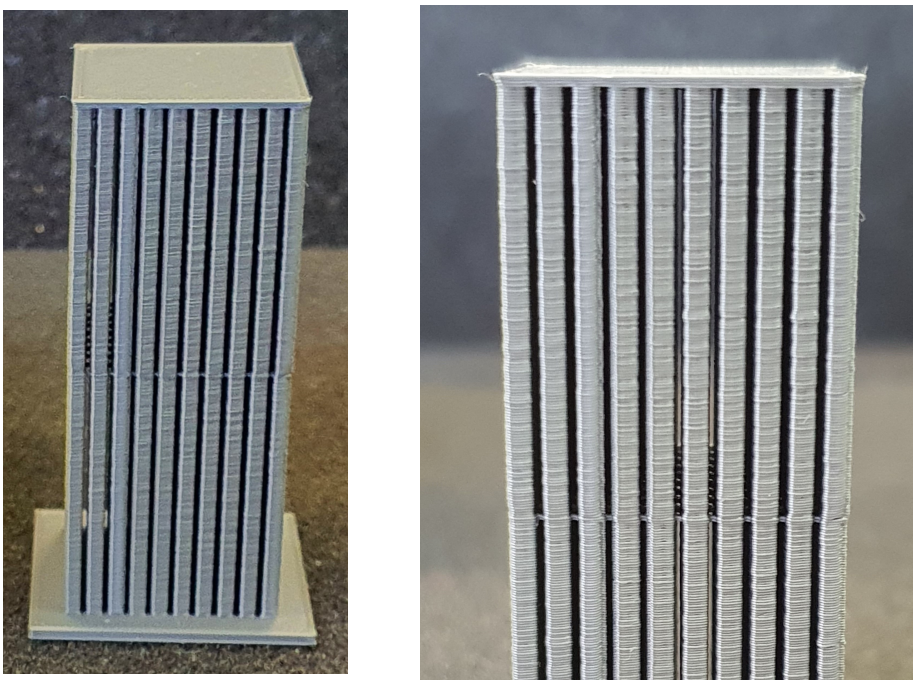

(a) (b)

Figure 6.11: PLA-M.A.D.E 3D printed collimator

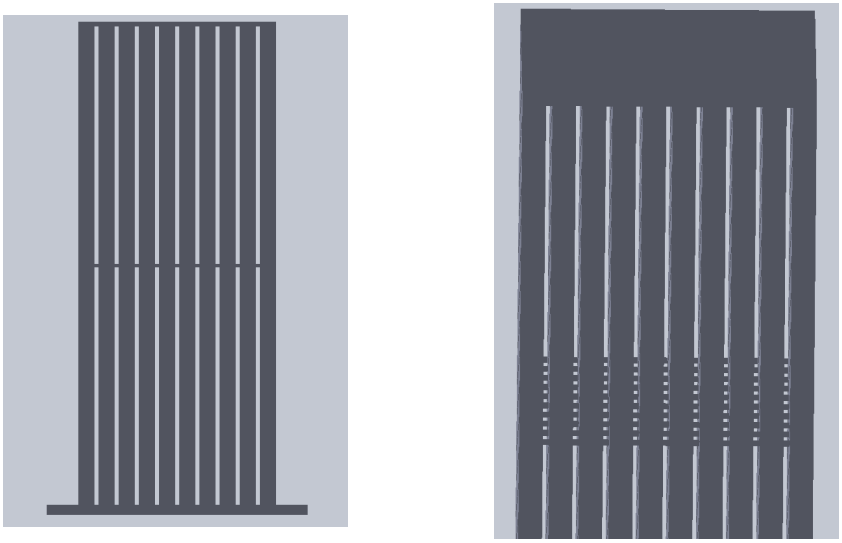

(a) (b)

Figure 6.12: PLA-M.A.D.E CAD with supporting grid

same procedure as for the previous two. The empty weight of this sample was 12,04 g. The total weight after the filling process was 47,66 g. This means that we got only

∼35,62 g of dispersed tungsten powder on ∼104 g, reaching a filling percentage of ∼33 % only. This sample too has been after the filling process viewed in the CT to observe how the powder dispersed between the pixels. The side and top view of the PLA-MADE sample can be seen in Figure 6.13. The samples have been all weighted using a Kern EW4200-2NM weight scale with an accuracy of ±0.02 g. Here too is

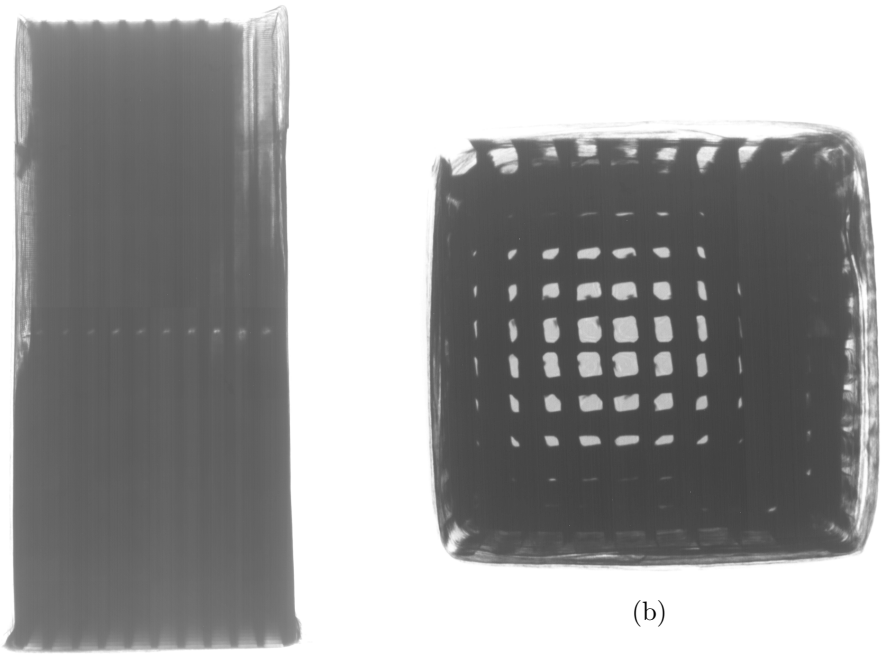

(a) (b)

Figure 6.13: PLA-M.A.D.E CT side view(a), PLA-M.A.D.E CT top view (b)

evident that the filling up of the sample is not homogeneous along all the volume of the sample, despite the cleanliness of the printed part. In Figure 6.13(a) it is possible to see a series of small white spot that are the grid structure components placed by MADE Concept at half height of the model.

In the Table 6.1 below are collected all the weight and filling percentage of the first concept collimators samples 3D printed.

Table 6.1: Collimators first concept tungsten powder filling percentage

| **Collimator Sample** | **EW(g)** | **FW(g)** | **FP(g)** | **EP(g)** | **Filling** % |
|---|---|---|---|---|---|
| PLA UNIVPM | 10,02 | 41,83 | 31,81 | 104,99 | 30 |
| PA2200 PROSILAS | 9,25 | 49,16 | 39,91 | 104,99 | 38 |
| PLA M.A.D.E Concept | 12,04 | 47,66 | 35,62 | 104,00 | 33 |

*EW = Empty weight *FW = Filled weight *FP= Filled powder *EP = Expected powder

## 6.2 Optimized Collimator concept

The first collimators concept filled with tungsten powder have been sent to BioEmission Technology Solution where they were experimentally evaluated, as we will see later in a specific chapter. After the evaluation, in accordance with the BIOEMTECH and with their needs, the collimator geometry has been updated and optimized. The height of the collimator has been lowered down to 30 mm, the hole square section increased up to 2 mm and the septa thickness increased up to 0,5 mm. The optimized concept CAD can be seen in Figure 6.14.

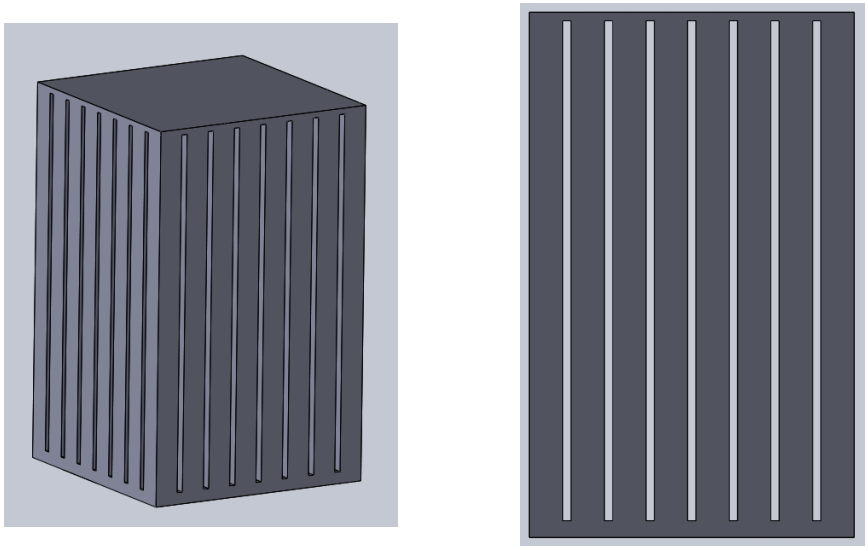

(a) (b)

Figure 6.14: Optimized concept collimator CAD

The new geometry has been chosen in order to results more efficient from the sensitivity point of view with respect to the spatial resolution. Indeed as we know from equation 3.11, lowering the length of the hole and increasing the hole diameter we will experience a decreasing in spatial resolution and an increasing in collimator efficiency. However, according to some preliminary tests they experimentally did, this new configuration worked well for the purpose of the pre-clinical investigations where they need the use of also of high energy radioisotopes (e.g. Lu177, In111 and Ga67) rather than only of Tc99m.

### 6.2.1 Optimized Collimator concept PLA-UNIVPM

In Figure 6.15 the optimized collimator sample fabricated using the 3D printer ENDER 5 PLUS located in our laboratory is shown. The height of the optimized geometry allows to avoid completely the problem related to the generation of the bending momentum as occurred for the first concept to M.A.D.E Concept in the case of a perfectly clean 3D printed part. However, the top base has been left in order to guarantee better stability between the extruded pixels when the filling procedure has been faced. Indeed, even if the lower height allowed to avoid the bending momentum


(a) (b)

Figure 6.15: Optimized concept collimator PLA-UNIVPM

of the pixels during the passage of the extruder, during the filling process and consequently during the warping with insulating material of the filled sample, the pixels without the presence of the top base could have incurred in misalignments and in breaks due to the exerted forces. The bigger septa thickness in conjunction with a bigger extruded pixel, allow our 3D printer to fabricate a better sample if compared to the first concept. Differences between the samples 3D printed and the respective CAD models will be evaluated in a specific section.
As can be seen in the above figure our 3D printer always left some material between the pixels; material that was then partly removed by means of a needle.
The optimized concept has been than filled with the tungsten powder as did before. The bigger septa and higher cleanliness of the printed components made us think that the previous method of filling could now work better, as can be see in Figure 6.16 where the powder after a long filling up seems to be dispersed homogeneously between the septa. Unfortunately the first filling method resulted to be poor also with the optimized geometry as can be seen in the below images (Figure 6.17). As can be seen in Figure 6.17(a) the powder didn't deposit in an homogeneous way and didn't compacted. The weight of the sample empty was 8,88 g, while the total weight after the filling up was 32,82 g. We got only ∼23,94 g of powder on ∼71,79 g reaching only the ∼33% of the total filling. Instead, looking at Figure 6.17(b) and comparing it with Figure 6.7(b) it is possible to see how increasing the hole dimension up to 2 mm from 1.5 mm of the first concept, allow to print square with higher accuracy. However, also in this case, visualizing the sample at the CT, the goodness of the proposed idea is confirmed.

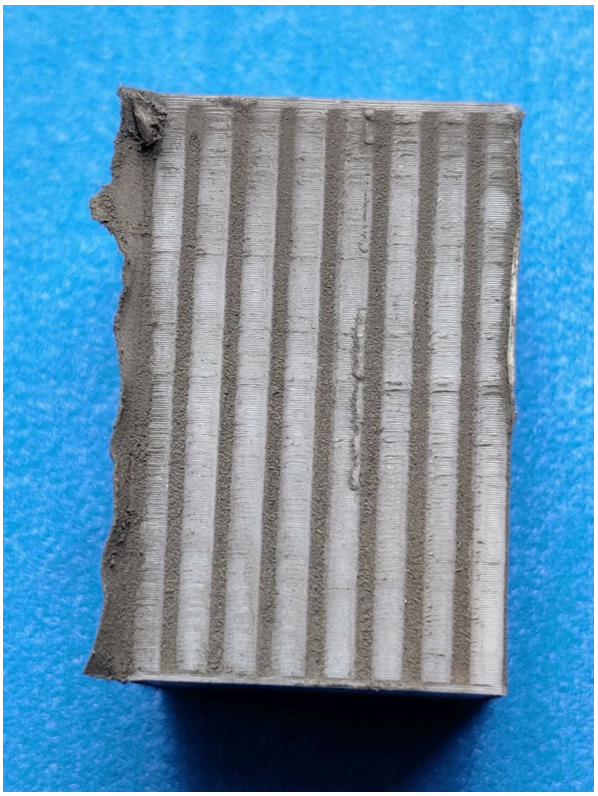

Figure 6.16: PLA-UNIVPM optimized geometry filling process

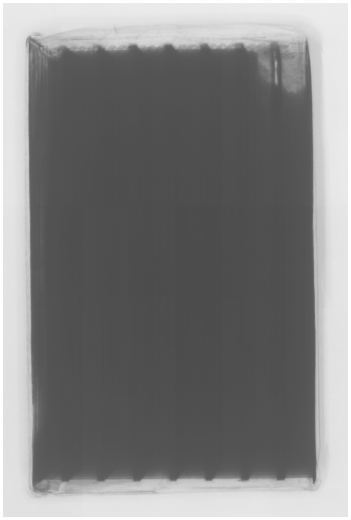

(a)

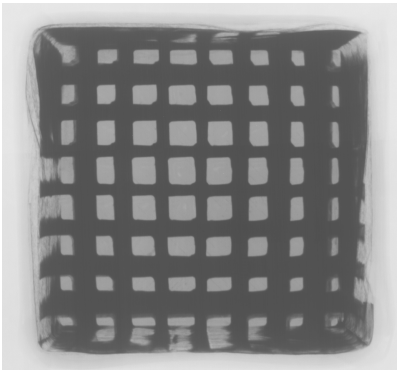

(b)

Figure 6.17: Optimized PLA-UNIVPM CT side view (a), PLA-UNIVPM CT top view(b)

### 6.2.2 Optimized Collimator concept PA2200-PROSILAS

The optimized collimator has been 3D printed, as for the first concept, also using the SLS printing process by PROSILAS srl. The fabricated sample can be seen in Figure 6.18. The accuracy and precision of the SLS printing process is appreciable, as for the first concept too, specially for the cleanliness of the space between the septa. The material used for the manufacturing process was always the PA2200. The printed sample has been then filled in the same manner as the previous one. The dispersion of the tungsten powder, also in this case where the septa were bigger and the space between the extruded pixels extremely clean, was not accomplished in the proper manner. Indeed, as can be seen in Figure 6.19(a) the powder didn't disperse homogeneously between the septa and we experienced the same problem of compacting the powder in order to remove all the air particles trapped between the powder particles itself. The empty septa volume that is visible refers to the back of the sample imaging to fill the sample itself from the left side of the Figure 6.19(a). This is evident also in the previous collimators filling processes, both for the first and optimized concept, meaning that even if shaking the samples seemed to properly distribute the tungsten powder, in reality the lack of compression of the powder itself and the impossibility to see how the powder distributes on every side, due to the fact that three out of four side of the sample were closed with duck-tape to avoid the exit of the powder, has made quite difficult to achieve a perfect filling up. The empty sample weighted 6,98 g and the total weight of the sample filled with the powder was 35,18 g. We got ∼28,2 g of powder dispersed on ∼71,79 g reaching only the ∼39% of the total filling. However, despite the low percentage of filling also this sample demonstrate the goodness of the proposed idea once viewed at the CT.

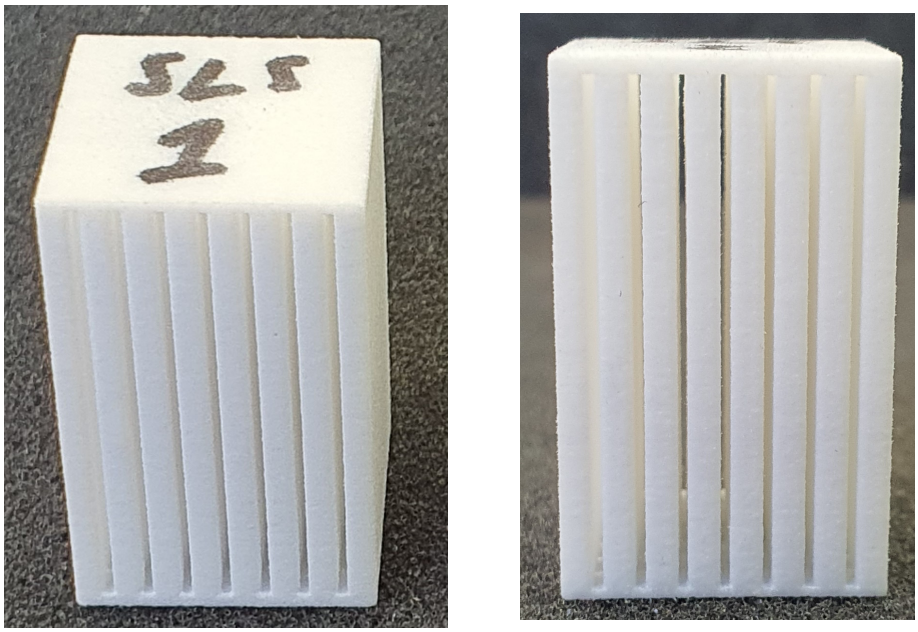


(a) (b)

Figure 6.18: Optimized concept collimator PA2200-PROSILAS

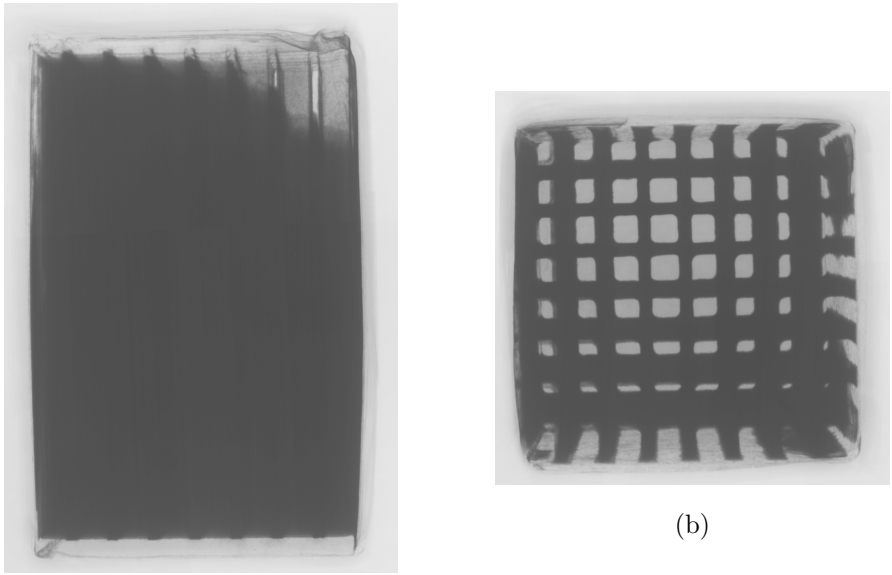

(a) (b)

Figure 6.19: Optimized PA2200-PROSILAS CT side view (a), PA2200-PROSILAS CT top view(b)

### 6.2.3 Optimized Collimator concept PLA-M.A.D.E Concept

The optimized geometry has been finally fabricated also using the FDM process provided by M.A.D.E Concept as for the first concept. The printed sample can be seen in Figure 6.20. The material used for the printing process was a PLA. The better printer quality, as already described when we present the first concept printed by M.A.D.E Concept, allow them to manufacture a quite perfect object with a really high quality. Comparing the M.A.D.E sample with that provided by PROSILAS is immediately clear, from qualitative point of view, the quality that FDM printer is able to reach at a much lower cost if compared to the SLS process (already of his own cheap). Unfortunately this last sample has arrived after the previous two were filled and sent to BioEmission Technology Solutions for the experimental tests. However, this unexpected event allows us to test a new filling process placing the sample inside a box a covering it with the tungsten powder. The sample has been then placed on the top of a shaker and white noise in the range 20-20000 Hz has been supplied for 30 minutes in order to apply a shaking movement to the powder to properly fill all the gap between the septa. The empty collimator weighted 9,43 g. The filled collimator using the new filling process instead weighted 24,67 g, much lower than that using the hand filling process. This can be addressed to the fact that when we hand filled the samples we also tried to compact and press the powder between the septa, while using the shaker this pressing component went to loose.

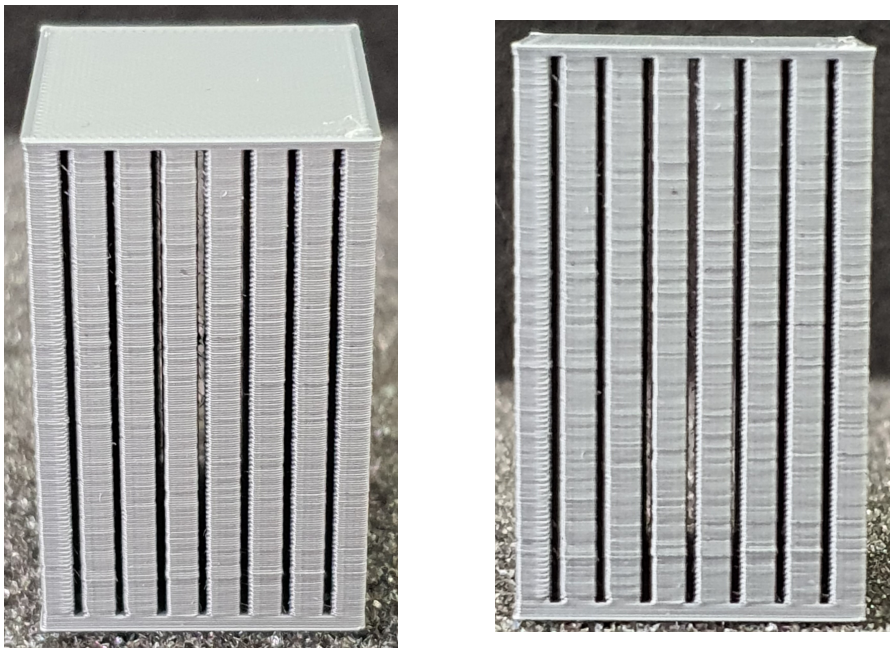

(a) (b)

Figure 6.20: Optimized PLA-M.A.D.E Concept collimator sample

In the Table 6.2 below are collected all the weight and filling percentage of the optimized concept collimators samples 3D printed.

Table 6.2: Collimators optimized concept tungsten powder filling percentage

| **Collimator Sample** | **EW(g)** | **FW(g)** | **FP(g)** | **EP(g)** | **Filling** % |
|---|---|---|---|---|---|
| PLA UNIVPM | 8,88 | 32,82 | 23,94 | 71,79 | 33 |
| PA2200 PROSILAS | 6,98 | 35,18 | 28,20 | 71,79 | 39 |
| PLA M.A.D.E Concept | 9,43 | 24,67 | 15,24 | 71,79 | 21 |

*EW = Empty weight *FW = Filled weight *FP= Filled powder *EP = Expected powder

## 6.3 Geometry comparison between CAD and printed object

The six printed sample have been then scanned using a Zeiss METROTOM CT and each sample have been scanned with a voxel size of 40$\mu$m. Once the samples have been scanned the cloud points were imported in a dedicated software of the CT machine itself in order to reconstruct the STL file from the CT slices. The meshes have been then imported in an open source software called MeshLab used for processing and editing 3D triangular meshes [2]. The imported meshes have been initially pre-processed in order to clean them. Indeed, even if the 3D printed sample were placed

on a styrofoam support that is practically transparent to the X-rays, some styrofoam still remained after the mesh reconstruction. In Meshlab software the meshes have been cleaned and all the styrofoam and other imperfections were removed. After that the meshes have been reconstructed using a reconstruction algorithm called "Screened Poisson" used to obtain watertight surface[20]. The cleaned and reconstructed meshes of the first 3D printed samples can be seen in Figure 6.21 Looking at Figure 6.21(a)

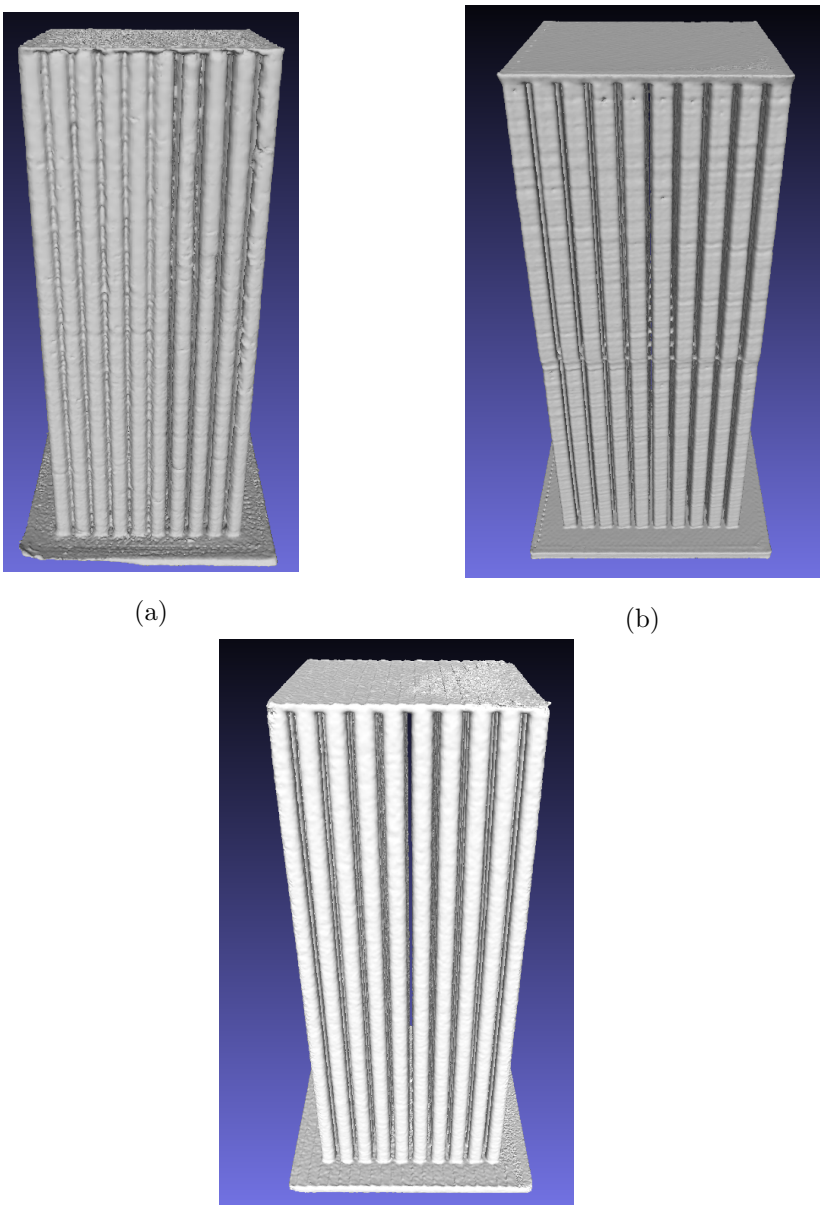

(a) (b)

(c)

Figure 6.21: First concept cleaned meshes PLA-UNIVPM (a), PLA-M.A.D.E (b), PA2200-PROSILAS(c)

is possible to see how, even if cleaned, the mesh still shows the PLA webs produced during the printing process done with the Ender 5 Plus printer. The webs are not present on every side, but there is a preferred direction along which the extruder produce this kind of defect. These defects were considered for the alignment process as we will see later.

Instead, in Figure 6.22 the processed meshes of the optimized samples are shown. The difficult encountered by our 3D printer (Ender 5 Plus) are not present instead in

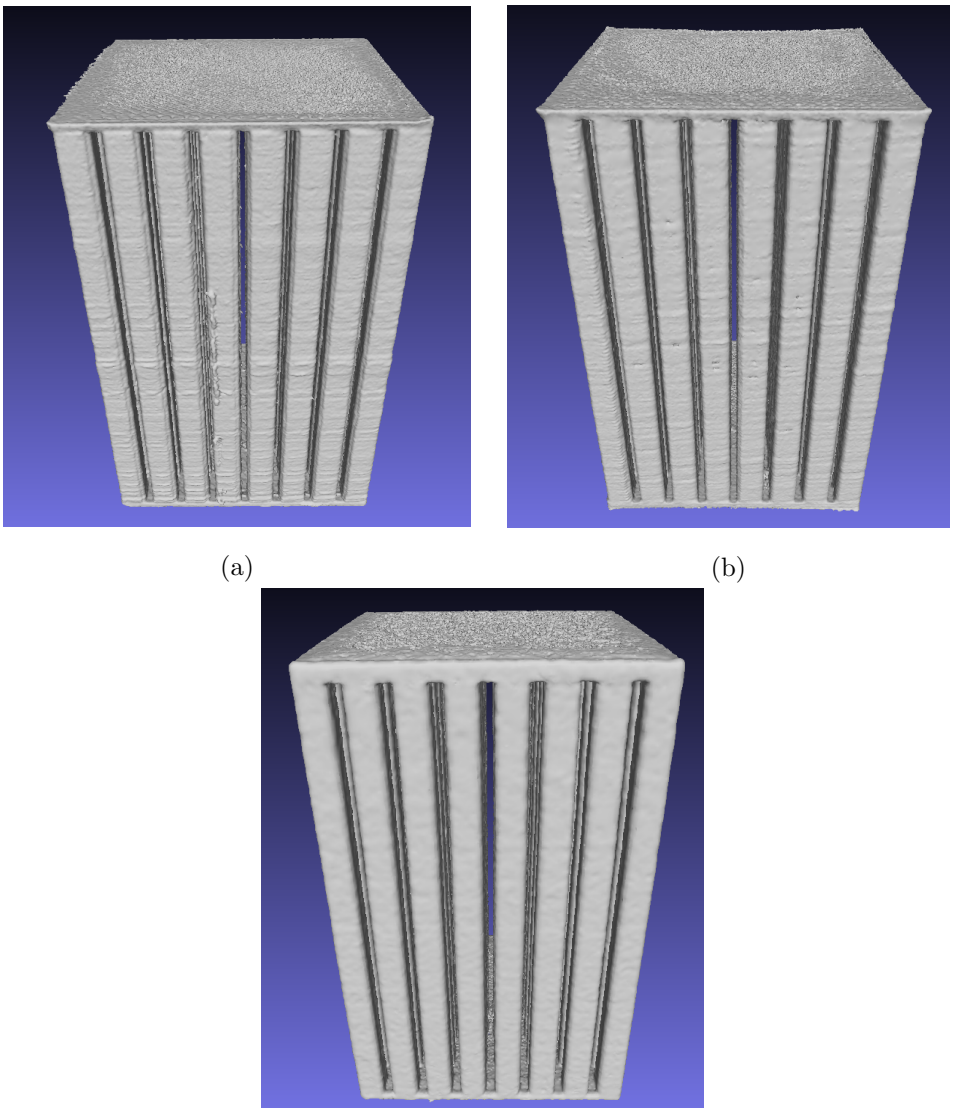

(a) (b)

(c)

Figure 6.22: Optimized concept cleaned meshes PLA-UNIVPM (a), PLA-M.A.D.E (b), PA2200-PROSILAS(c)

the printed optimized sample. But this is mainly due to the uncertainty of the printer to print object with high precision and repeatability as we will see later.

A qualitative and quantitative analysis to see how the printed samples differed with the CAD model have been performed in Meshlab. In this way we could have an idea of how much the 3D printed objects moved away, in terms of distance of the mesh point from the CAD models.
After cleaning the meshes the respective stl CAD models of the first and optimized concept have been imported in Mehslab software in order to proceed with the alignment of the meshes. The alignment process start with the "glueing" of the reference mesh and then we performed a point based glueing with the CT mesh. We defined ten points on the reference mesh covering all the surface, and then we manually redefine these points on the mesh to be aligned. After an initial pre-alignment we performed the ICP algorithm in order to produce a finer alignment between the two meshes. After that the Hausdorff distance between them has been computed. The Hausdorff distance samples one of the two meshes and finds the closest point over the other mesh. The last passage was to apply a quality mapper trough which is possible to observe where there are major differences in the distance.
The first alignment, before the application of the ICP algorithm, is manually performed going to pick at least four points on the reference mesh and then reports these points on the mesh to be aligned. This manual pick and place work is naturally subjected to uncertainty, even if really small, since it is quite impossible to be exactly precise in reporting the picked points from the reference mesh to the target one.

**Comparison first concept collimator PLA-UNIVPM & CAD**

In Figure 6.23 a comparison between the CT mesh of the PLA-UNIVPM first concept collimator and the CAD model is shown. The below images represent the four side of the PLA-UNIVPM CT mesh where the Hausdorff distance and the quality mapper have been applied. The left bar histogram represents the per vertex/face quality (in distance) of the PLA-UNIVPM. The red value refers to the verteces with higher distance from the reference CAD mesh, while the blue are those verteces that are closer to the CAD. The alignment process shows the problems we encountered printing this

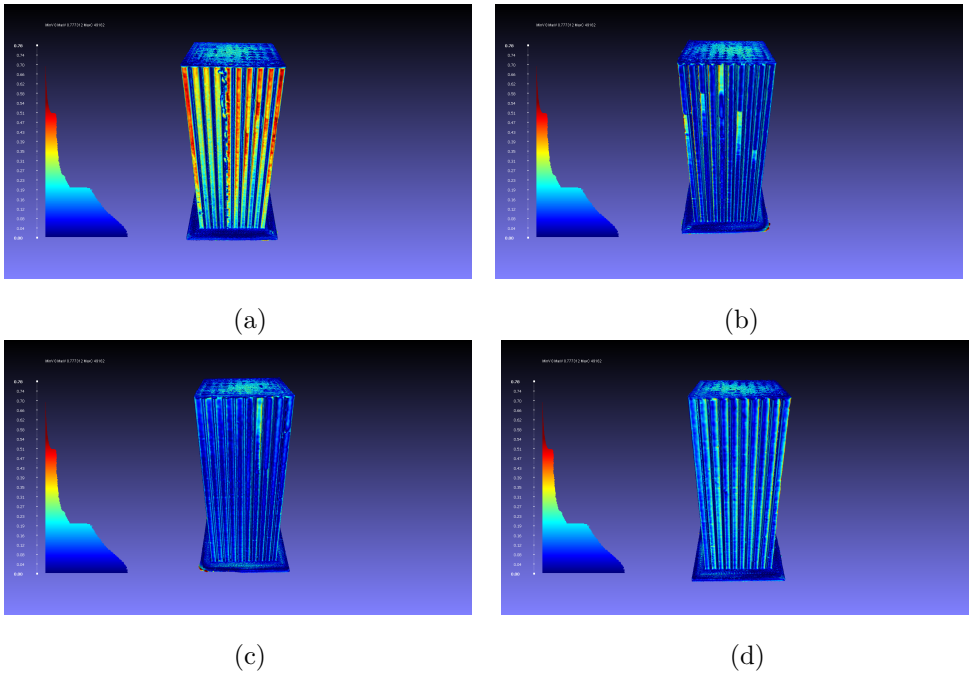

(a) (b)

(c) (d)

Figure 6.23: First concept collimator PLA-UNIVPM quality mapper

sample with our 3D printer. The error is mostly visible on the first side of the printed sample and between the extruded pixels itself, while are not so important on the other three side. The minimum error in distance computed after the alignment with the CAD model is 0.0021 mm, while the maximum achievable is 0.5446 mm with a mean distance between the mesh of 0.2733 mm. Comparing these values with those of the samples printed using the SLS process and the FDM process by M.A.D.E it is evident which are the differences between the printing technologies.

**Comparison first concept collimator PLA-M.A.D.E & CAD**

In Figure 6.24 a comparison between the CT mesh of the PLA-M.A.D.E first concept collimator and the CAD model is shown. The majority of the differences are

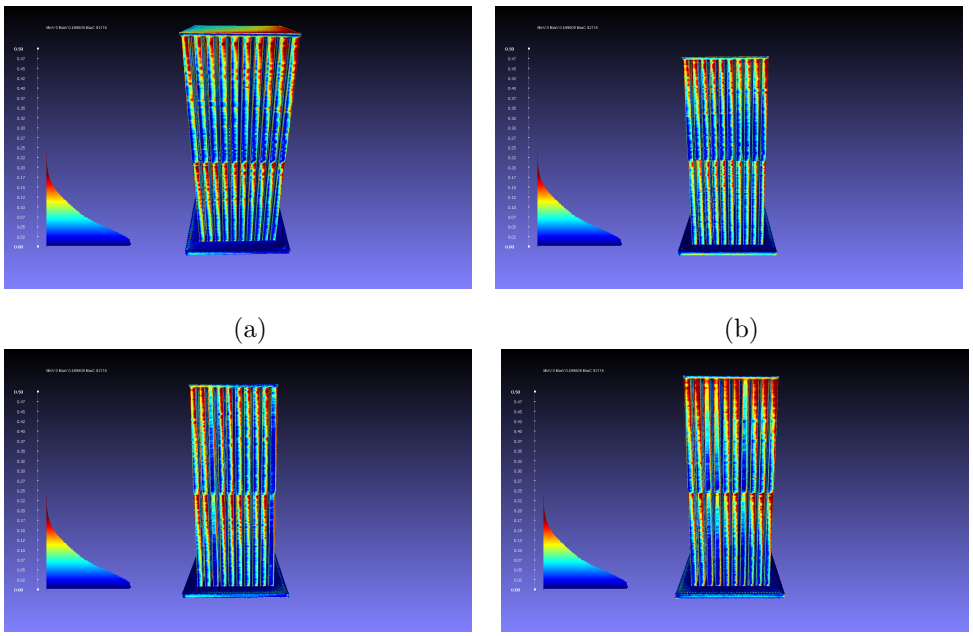

(a) (b)

(c) (d)

Figure 6.24: First concept collimator PLA-M.A.D.E quality mapper

observable looking at the extruded pixels that show a bigger distance with respect to the CAD. Furthermore, is quite evident the differences that arise at half of the model height too where M.A.D.E placed the grid to avoid the bending momentum of the pixels itself. After the alignment the minimum distance computed by the algorithm between the CT mesh and the CAD model is 0.0008 mm, while the maximum is 0.17780 mm with a computed mean distance of 0.0893 mm.

### Comparison first concept collimator PA2200-PROSILAS & CAD

In Figure 6.25 a comparison between the CT mesh of the PA2200-PROSILAS first concept collimator and the CAD model is shown. The greater difference is observable

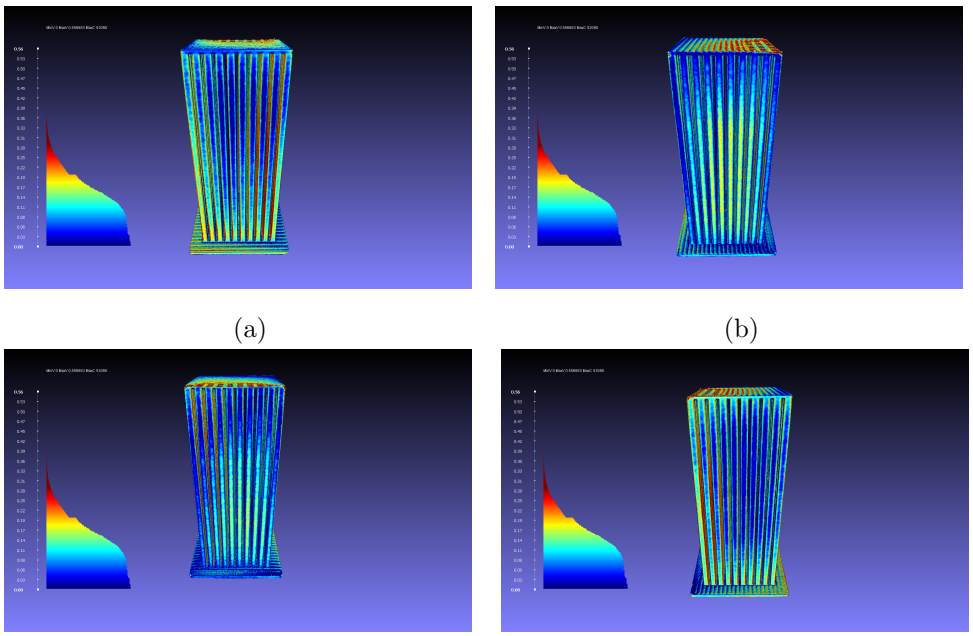

(a) (b)

(c) (d)

Figure 6.25: First concept collimator PA2200-PROSILAS quality mapper

looking at the top base that show the bigger distance with respect to the CAD and also the internal part of the extruded pixels show a high difference in distance with respect to the CAD. After the alignment the minimum distance computed by the algorithm between the CT mesh and the CAD model is 0.0017 mm, while the maximum is 0.2855 mm with a computed mean distance of 0.1436 mm.

### Comparison optimized concept collimator PLA-UNIVPM & CAD

In Figure 6.26 a comparison between the CT mesh of the PLA-UNIVPM optimized concept collimator and the CAD model is shown. The greater difference is observable

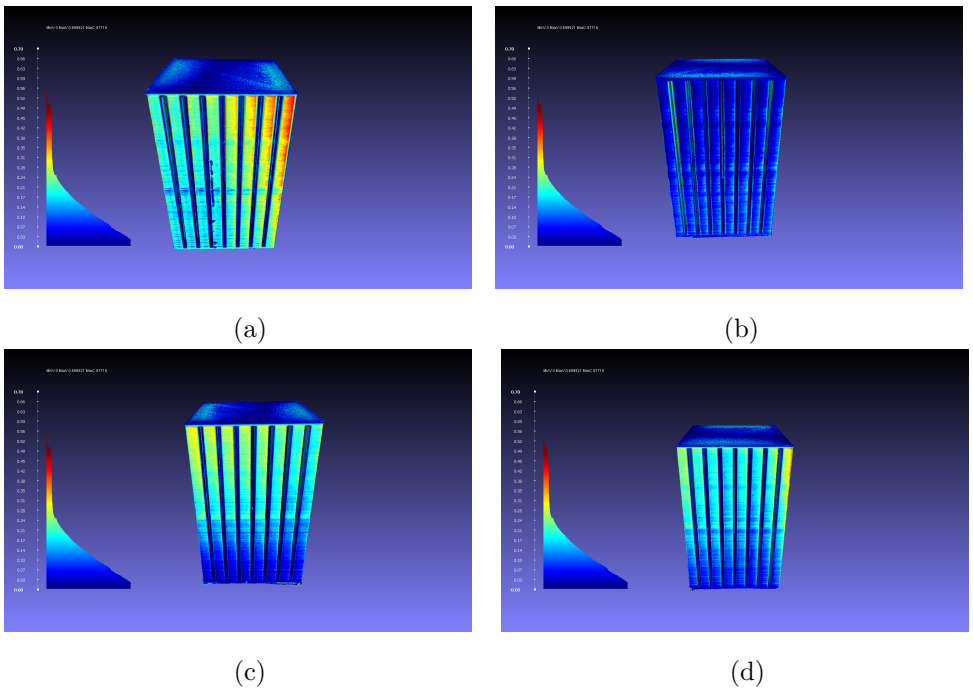

(a) (b)

(c) (d)

Figure 6.26: Optimized concept collimator PLA-UNIVPM quality mapper

looking at Figure 6.26(a) where the distance with respect to the CAD is higher specially in the top right corner. After the alignment the minimum distance computed by the algorithm between the CT mesh and the CAD model is 0.0015 mm, while the maximum is 0.4815 mm with a computed average distance of 0.2415 mm.

### Comparison optimized concept collimator PLA-M.A.D.E & CAD

In Figure 6.27 a comparison between the CT mesh of the PLA-M.A.D.E optimized concept collimator and the CAD model is shown. There are no remarkable differences

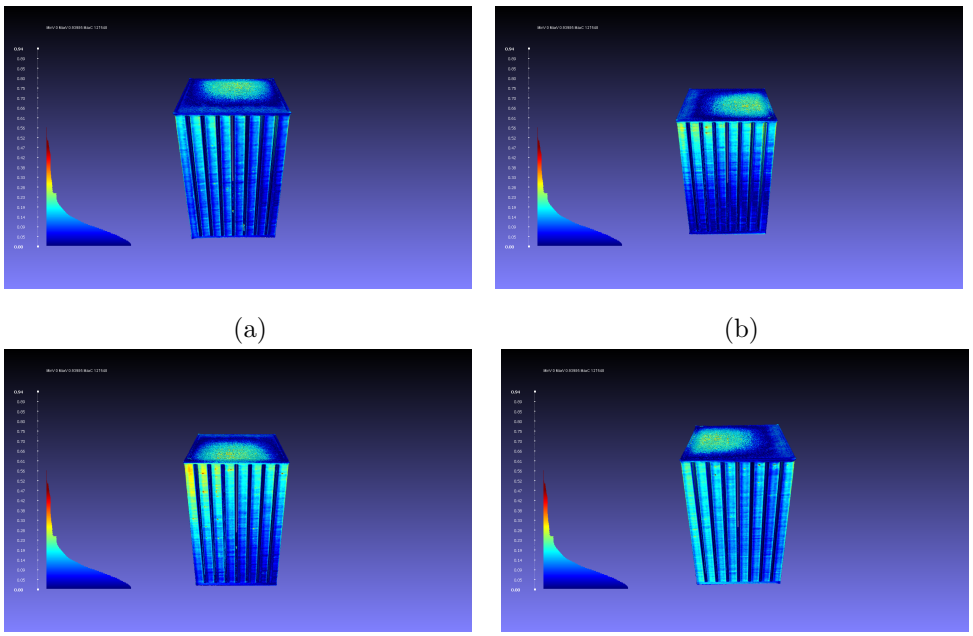

(a) (b)

(c) (d)

Figure 6.27: Optimized concept collimator PLA-M.A.D.E quality mapper

in distance with respect to the CAD. After the alignment the minimum distance computed by the algorithm between the CT mesh and the CAD model is 0.0013 mm, while the maximum is 0.4694 mm with a computed average distance of 0.2354 mm.

**Comparison optimized concept collimator PA2200-PROSILAS & CAD**

In Figure 6.28 a comparison between the CT mesh of the PA2200-PROSILAS optimized concept collimator and the CAD model is shown. The greater difference is

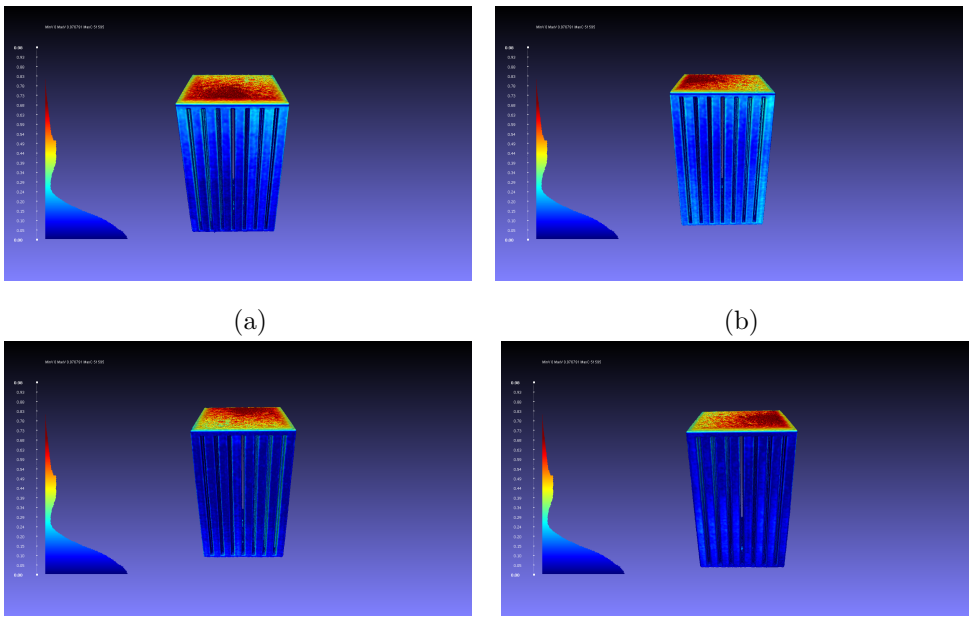

(a) (b)

(c) (d)

Figure 6.28: Optimized concept collimator PA2200-PROSILAS quality mapper

observable looking at the top base that show the bigger distance with respect to the CAD while the the extruded pixels, externally and internally does not show big error in distance with respect to the CAD . After the alignment the minimum distance computed by the algorithm between the CT mesh and the CAD model is 0.0013 mm, while the maximum is 0.4694 mm with a computed average distance of 0.2354 mm.

In the Table 6.3 below the distances between the scanned meshes and the relative CAD models are reported

Table 6.3: Distance comparison between CT meshes and CAD models of first concept (FC) and optimized concept (OC)

| Collimator Sample | Min(mm) | Max(mm) | Mean(mm) |
|---|---|---|---|
| PLA UNIVPM FC | 0.002 | 0.544 | 0.273 |
| PLA M.A.D.E FC | 0.001 | 0.177 | 0.089 |
| PA2200 PROSILAS FC | 0.002 | 0.285 | 0.143 |
| PLA UNIVPM OC | 0.001 | 0.481 | 0.241 |
| PLA M.A.D.E OC | 0.001 | 0.469 | 0.235 |
| PA2200 PROSILAS OC | 0.002 | 0.689 | 0.345 |

The results of the distance measurement show that all the 3D printed objects,

except for the first concept sample printed by UNIVPM in PLA, and considering the mean distance values, have been printed with high accuracy with respect to the CAD model. Looking at the histograms of the single meshes it is evident that the typical distribution of the error in distance is of the type exponential. The only difference is remarkable for what concern the PA2200-PROSILAS samples (first and optimized concept) where we have a distribution non exponential with a huge dispersion specially if we look at the optimized PA2200-PROSILAS sample. Here we get a huge dispersion relative to the top of the sample that derive most from the CAD. This is sensed also touching that surface that is highly rough. This non-exponential distribution is highly remarkable also and more for the PLA-UNIVPM first collimator concept.
These curves of distribution are relative to a single 3D printed object meaning that in this case we achieved a high accuracy but this does not guarantee that printing the sample again will produce the same results. This is true specially for the printing process exerted by our 3D printer (Ender 5 PLus) that in three successive printing processes gave different results. In particular, in Figure 6.29(a) where three new optimized collimator samples 3D printed with the Ender 5 Plus are shown, it is possible to see how different they appear if compared with the first sample printed and reported in Figure 6.15. Particularly evident is the printing error for what concern the two in the middle extruded pixels that have been printed, specially in the second and third sample, practically fused. We found that using cheap FDM printer does not

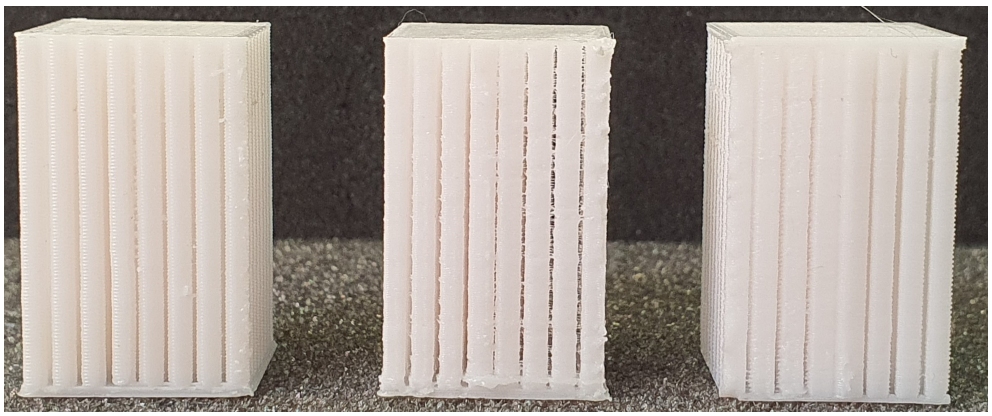

Figure 6.29: Three consecutive printed samples with Ender 5 PLus FDM printer

guarantee at all precision and so repeatability of the printing process. This is mainly due to the fact that the hardware the printer is made is cheap and need continuous attentions in order to properly work. This is not evident instead using the other two technology specially the SLS that being an industrial machine is able to guarantee excellent reproducibility of the printed object. The Original Prusa model I3 MK3S+ printer used by M.A.D.E Concept, having a much better and improved hardware with respect to our FDM printer, is able to achieve a good repeatability and precision in the printing process. The capacity of the SLS and M.A.D.E FDM printer to fabricate sample with a good repeatability is shown in Figure 6.30.

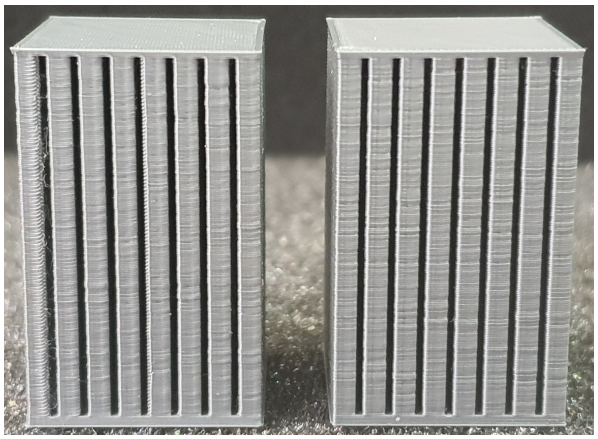

(a)

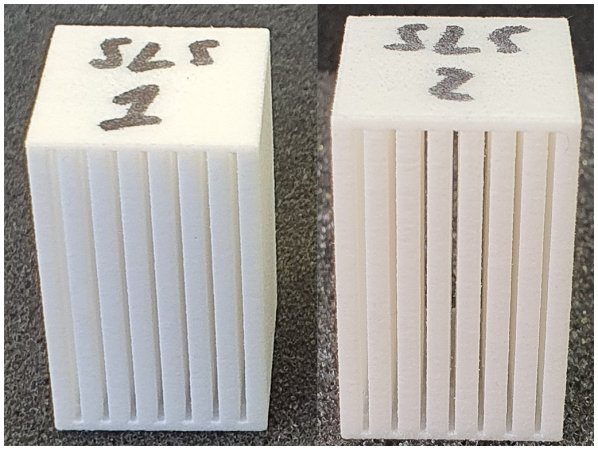


(b)

Figure 6.30: Optimized concept collimator PA2200-PROSILAS quality mapper

# Chapter 7

# Development of an imaging system for collimator 3D printing assessment

Considering all the difficulties in printing with accuracy and repeatability using the FDM printer Ender 5 Plus in use in our laboratory, we decided to implement an imaging system directly on-board of the 3D printer itself. This imaging system has been used in order to acquire an image of every printed layer of the collimator sample and then all the images, through a python algorithm, have been assembled and the 3D model of the printed object has been created. We can think to this imaging system as a sort of primitive CT scan.

### 7.0.1 Rationale

Why should we need a such imaging system?
Cheap FDM printers as the Ender 5 Plus we used for our task are not eligible to assure good accuracy and repeatability, specially in those prints were small features are needed. This is evident looking at the lack of repeatability and accuracy we experienced both for the first and optimized collimator concept. However, suppose someone wants to print its own custom collimator at low cost, without using expensive hardware or avoiding the use of middlemen like PROSILAS. As already said a cheap 3D printer is subject to a series of problems, mainly related to the quality of the hardware that make it not reliable in terms of accuracy and precision of printing. In the case of a collimator, as we know having septa with a specific thickness and holes with the exact specified dimension according to the clinical investigations needed, is really important in order to have reliable spatial resolution and sensitivity of the imaging system. Another really important aspect to consider is also the linearity of the extruded pixel that define the path through which the photons will travel. So, it is really important to assure a print were the hole are all parallel among them as much as possible and avoid misalignment of the layers during the print. So, could be it possible to have an errors in the printing process such that the final imaging performance of the system is not so greatly affected? Obviously, the printing errors could be easily studied and analyzed by means of CT scanner, as we did for the comparison of the printed sample and its relative CAD model. But, using a CT scanner has its

cost, really high costs and not everyone can afford them. Furthermore, using cheap FDM printers, as already stated, does not assure repeatability and precision of the printed samples and so it could be more important to see if and how much the printed sample, with all its errors and geometry non uniformity, could be reliable and could give useful information in terms of spatial resolution and sensitivity if compared to the reference geometry.
So, with the proposed imaging system, that we are going to present, we want to provide a low cost and effective alternative solution to CT scanner, in order to recreate a 3D model of the printed sample and use this reconstructed model to investigate, from the numerical point of view, how much the small variations, in terms of dimension of holes and holes linearity and parallelism, will affect the imaging performance of the printed collimator.

### 7.0.2 Hardware and configuration

The imaging system has been mounted on-board of the Ender 5 Plus 3D printer. It is composed of three red line lasers, an APSC camera (Nikon D7200) with a 60 mm focal length lens and a Raspberry Pi 4 module used to control the printing process and the acquisition algorithm. The assembled system can be seen in Figure 7.1.

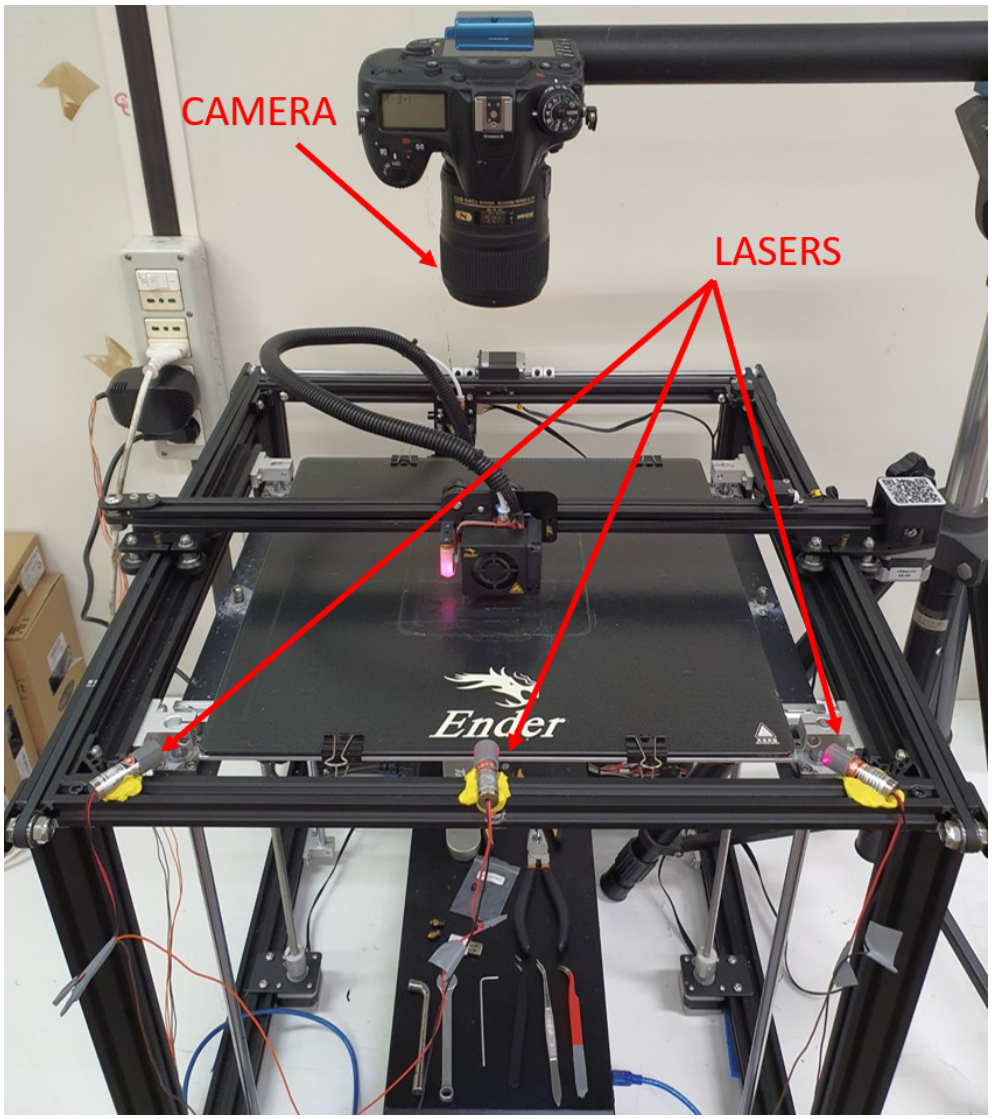


Figure 7.1: 3D printer imaging system

In Figure 7.2 the Raspberry module and the laser used are shown. The laser has been encapsulated using a small 3D printed cylinder to avoid that the red line of the laser will diffuse laterally too much causing non wanted reflections and eyes problem to the operator that want to approach the printer in order to see how the printing process is working. Furthermore, in this way we get a much more collimated laser blade on the layer of the printed obeject.

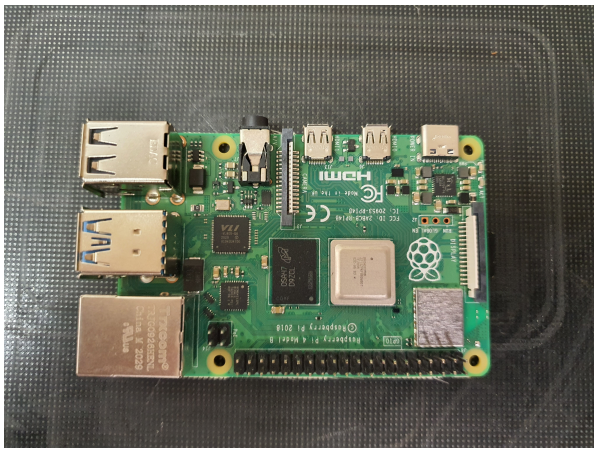

(a)

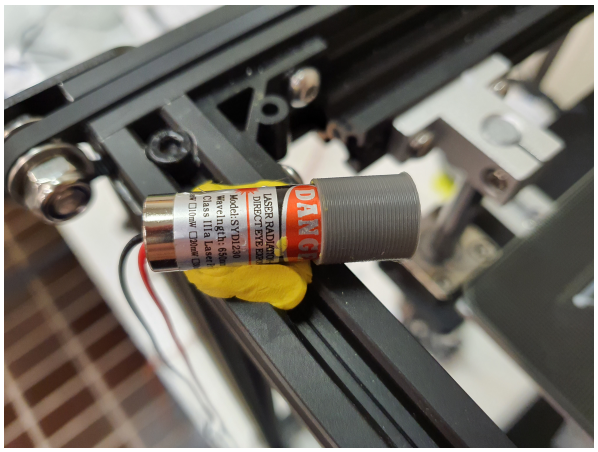

(b)

Figure 7.2: Raspberry module(a), laser(b)

We have chosen to use only three laser because of printer configuration. Indeed, looking at Figure 7.1 the only side free of mechanical parts in movement or cables is the front profile. The three lasers have been placed in order to light up the printed object from different angles in order ot have a lighting up as much uniform as possible. The lasers so placed, have been then angled in the vertical direction by means of some play dough as it can be seen in the previous image. Using the play dough let us be more free on the choice of the preferred angle for the illumination that using spherical bulky systems.

### 7.0.3 Working concept

The working flow of the algorithm used can be seen in Figure 7.3.

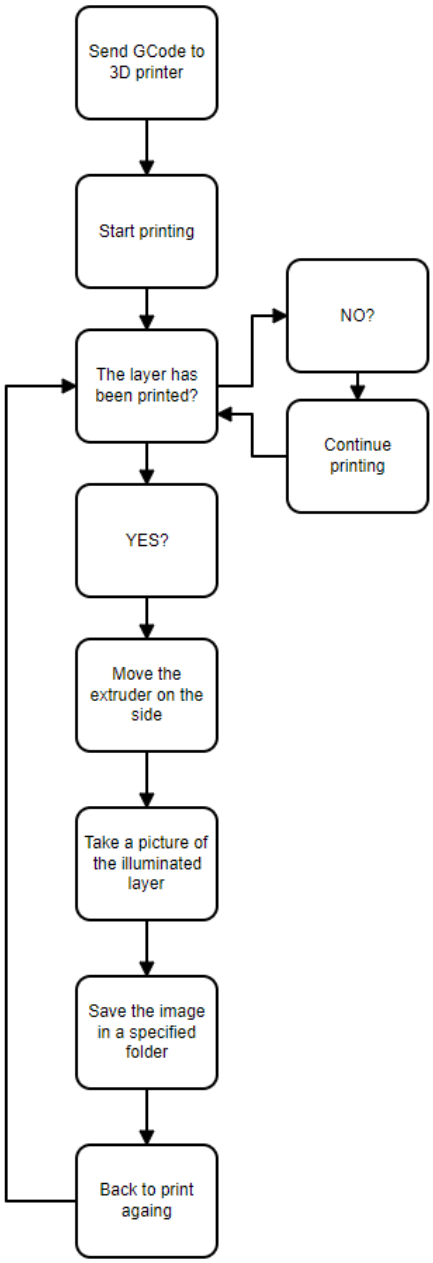


Figure 7.3: Flow chart of image system acquisition

The STL file of the CAD model is sliced and then sent through the python algorithm to the 3D printer. The printer start printing the model and once the first layer is finally reached the algorithm pause the printing process, move the extruder on one

side of the building plate in order to be far from the printed object until that moment, and then controls the connected camera to take a photo from above of the printed layer. After this, the algorithm send the command in order to start printing again until a new layer is printed and the process start again. All the images taken are then stores inside a folder and then used to reconstruct the 3D model by stacking them as if they were CT slices. The all process from the start of the print till the end must be done completely in the darkness. This is mandatory because in this way we are able to obtain a quite uniform illumination of the printed layer by means of the three lasers. I say "quite uniform" because the printing process, due to its non-accuracy and repeatability could print some extruded pixels higher than the neighbors causing the light to be stopped and so not reaching the pixels behind them.
In Figure 7.4 it is possible to see the system on and in its working condition (except for the ambient light that for photo purposes was high).

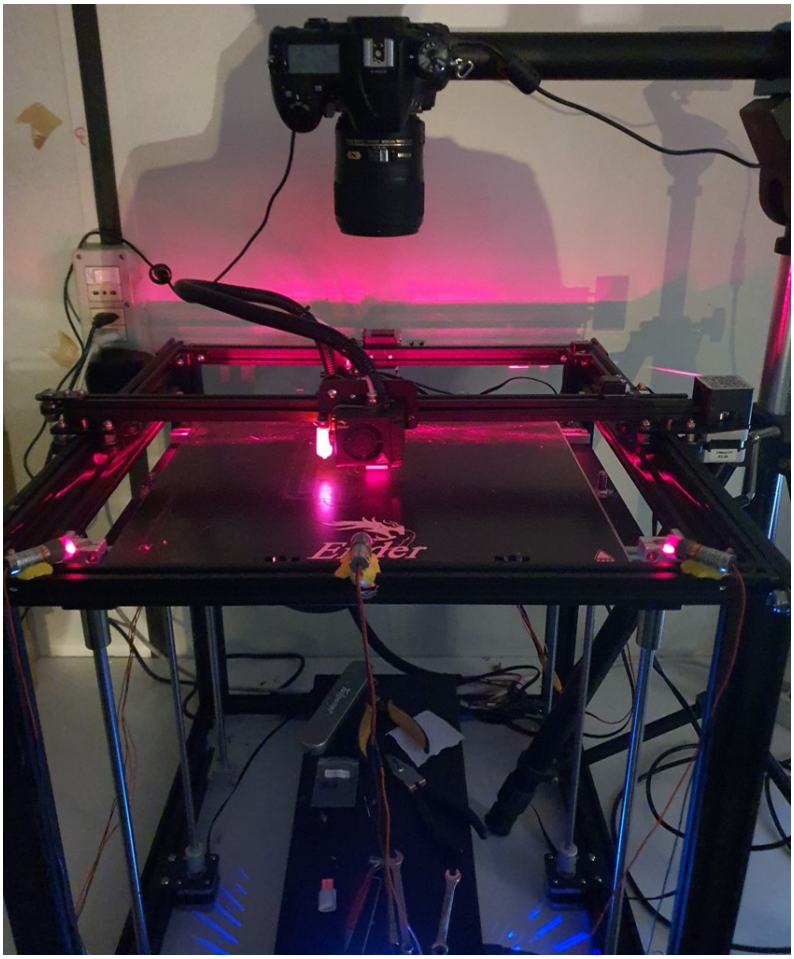

Figure 7.4: Imaging system working conditions

As previously introduced when we spoke about our 3D printer, the Ender 5 Plus even if lack in accuracy and repeatability when printing small features, has an important advantage that rely on the fact that it is the building plate to move in the Z

direction and not the extruder, meaning that each time a new layer has been printed the building plate will move down of a step in millimeters equal to the height of the layer itself, maintaining the illuminated layer always at the same distance from the camera sensor. This aspect made it possible to maintain both the illumination and the camera focus fixed without incurring in illumination or camera related problems. Indeed, the three lasers have been angled and collimated in order to light up as uniform as possible the printed layer, trying to avoid as much as possible the problems due to the different height of the extruded pixels. The camera has been fixed orthogonal to the building plate by means of its internal level and the one placed on the tripod head, and fixed at distance equal to 35 cm from the top layer of the printed part.

Instead in Figure 7.5(a) it is possible to see the working flow with no ambient light and in Figure 7.5(b) the photo of a printed layer used then for the reconstruction of the 3D printed model. The pink square visible in Figure 7.5(a) is the illuminated layer of the printed object. The main problem we faced using this approach relates to the first layers, depending on the height of the base and on the number of the layer set in the slicing software, that being close to the building plate when we take the photo we got also a lot of backscatter light from the building plate itself. Looking at Figure 7.5(b) is possible to appreciate the difference in the illumination previously highlighted. Indeed, some pixels appear to be less lighted than other, and this is due to multiple factors like that the first in the front and second rows are lower in height, due to printer accuracy and precision problems, with respect to the one in the third row causing the illumination to properly reach only them. This occurs also for other pixels in the matrix. This problems resulted in a tuning of the python algorithm used for the 3D reconstruction starting from the photo of the single layers. From the above image is then also possible to highlight all the printing errors. Some pixels resulted fused together, some are bigger than other, the square shape is practically never guaranteed and it is also possible to highlight a repetitive error of the extruder movement for some rows when it moves from left to right in the photo, visible as a sort of "tail" that the extruder create when moving from one pixel to the next. However, this acquisition setup allows to have practically a slice of the printed object. Indeed, the surrounding ambient darkness and the collimated light on the layer permits to highlight perfectly all the features of the printed object; printing errors that could be studied and investigated by means of dedicated algorithms for the image processing.

(a)

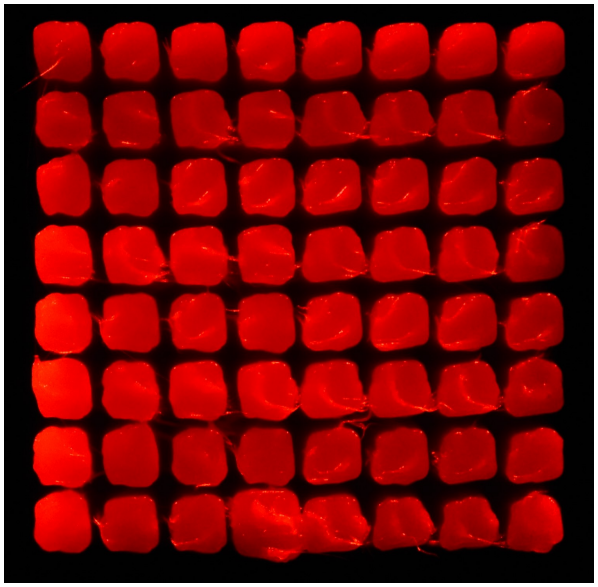

(b)

Figure 7.5: Real working conditions(a), 3D printed layer image(b)

### 7.0.4 Python reconstruction algorithm

The images obtained throughout the imaging system have been then processed using a dedicated python algorithm using OpenCV algorithms[29] [31]. The algorithm load all the images, less those images that refer to the bottom and top base. After the images have been loaded we proceeded to convert the RGB image into an HSV color space because we need it in order to work with threshold in the proper way. After the conversion we apply an Otsu threshold. This algorithm returns a single intensity threshold that separate pixels into two classes, foreground and background as can be seen in Figure 7.6[4]. After the Otsu's thresholding we proceeded applying a

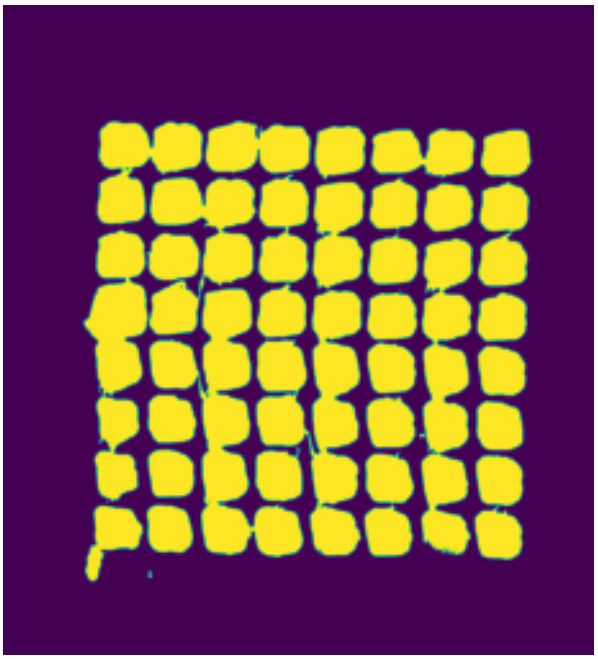

Figure 7.6: Otsu's thresholding

morphological closing/erosion filter in order to close small holes inside the foreground objects and we then apply the distance transform algorithm and we define the shape of the kernel to be used (rectangular in this case). The result of the transform is a gray level image that looks similar to the input image, except that the gray level intensities of points inside the foreground regions are changed to show the distance to the closest boundary from each point as shown in Figure 7.7[3]. In this way we get all the distance also between the centroid of each square hole. After this we apply a template matching cross correlation, that is a technique for finding areas of an image that are similar to a patch (template)[5] and using the correlation matrix obtained we apply an algorithm to find the peaks of the centroids previously found as visible in Figure 7.8. Finally, we proceeded to the identification of the contours of the printed pixels. In Figure 7.9 the contours have been highlighted and shown correctly. This process has been repeated then for every image obtained and then a marching cube algorithm has been applied in order to reconstruct the 3D model of the printed sample, as can be seen in Figure 7.10[7] [24]. Looking at the reconstructed collimator sample is immediately evident all the printing errors and defects (non parallelism between the extruded holes, fused holes, bigger holes) that now can be imported and used in

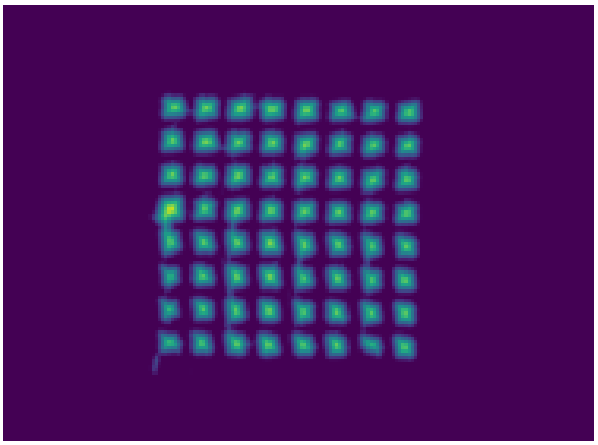

Figure 7.7: Distance transform

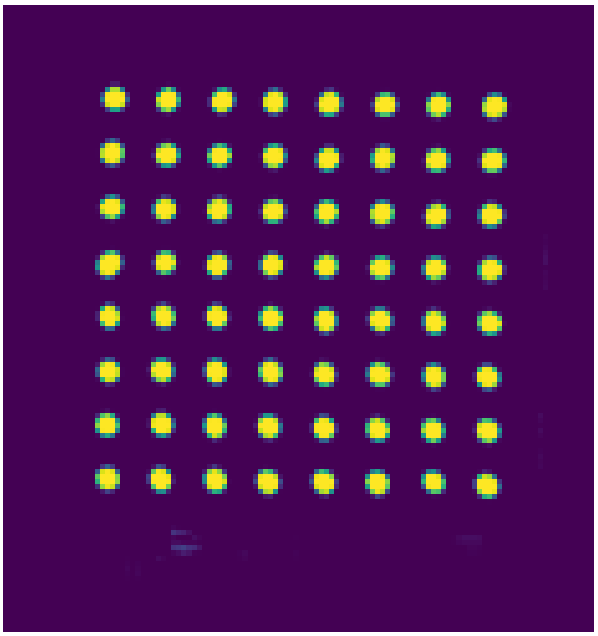

Figure 7.8: Centroid peaks

GATE in order to see how and if these defects interfere with the optical performance of an imaging system.

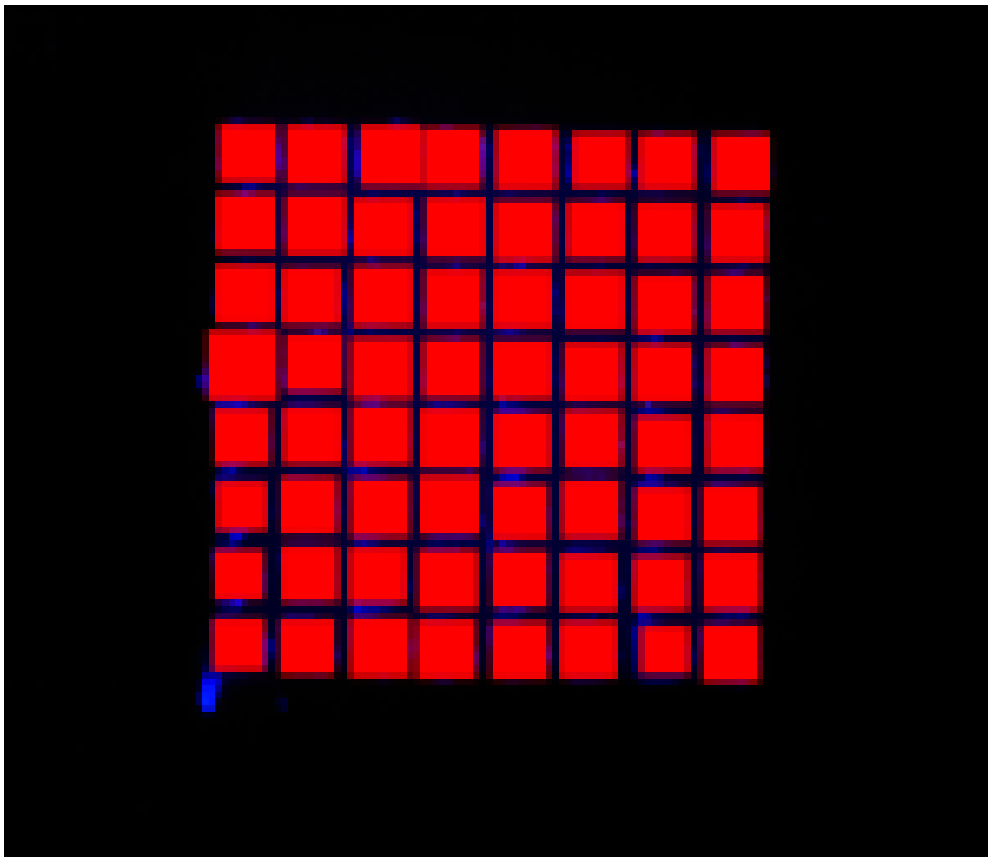

Figure 7.9: Holes contours

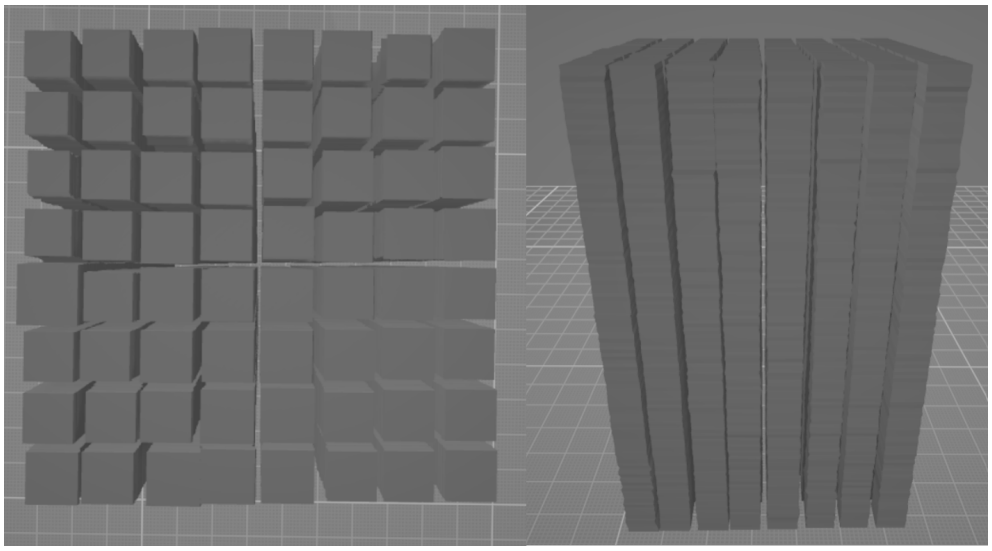

Figure 7.10: Reconstructed collimator sample

# Chapter 8

# Numerical results

The numerical results obtained by the simulations made in GATE are now presented. The results are presented in terms of spatial resolution and sensitivity both for the first and optimized collimator concept. The differences among the different collimators configurations have been evaluated highlighting the variations due to the extruded pixels with respect to the standard configuration.

## 8.1 First collimator concept

For the evaluation of the first collimator concept as radioactive source has been used the $^{99}$Tc. Indeed, this first concept of collimator, due to its geometric characteristics, can be considered a low-energy collimator, specially the reference configuration with a septa thickness of 0.2 mm. In Figure 8.1 the graph for the spatial resolution is reported, while in Figure 8.2 is reported the graph for the sensitivity.

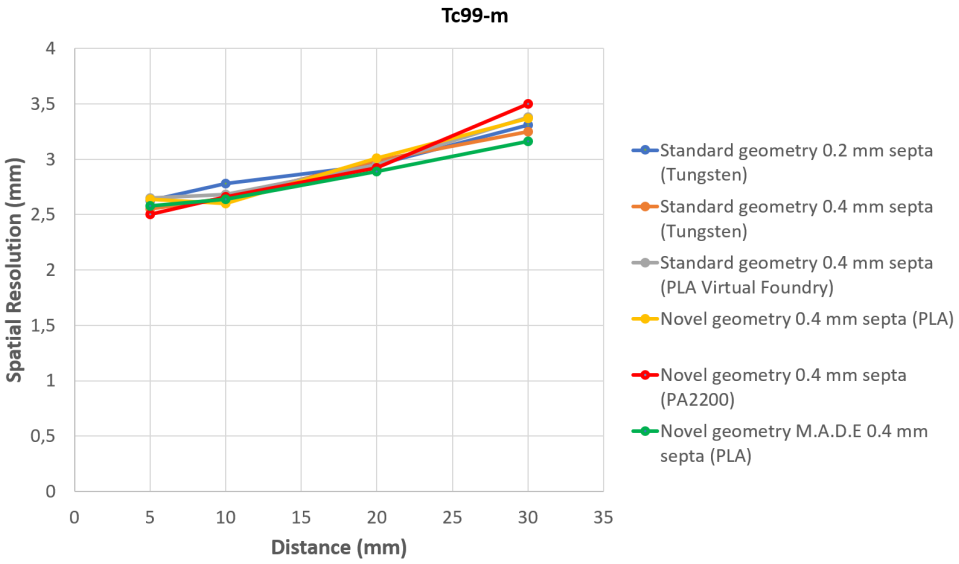


Figure 8.1: Spatial resolution as function of source to collimator distance

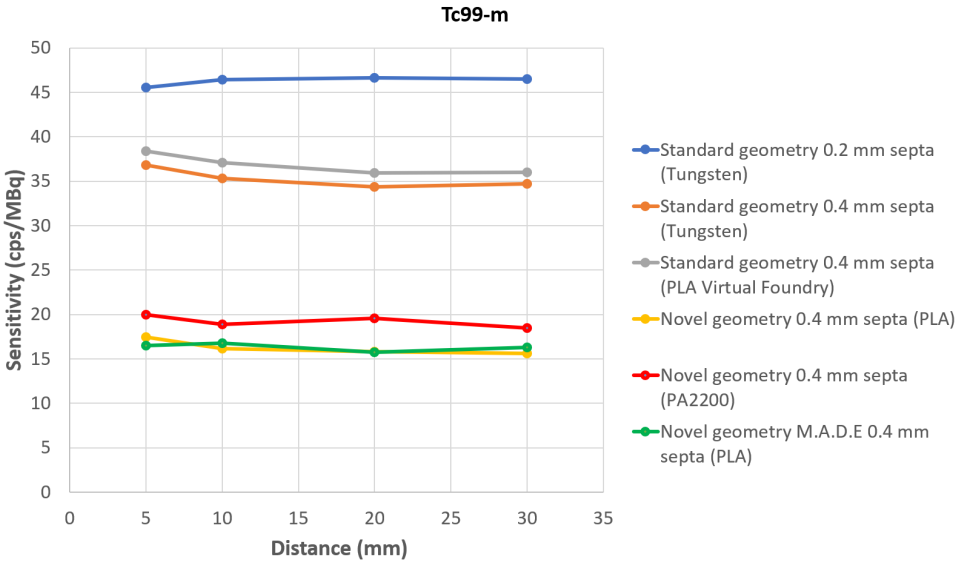


Figure 8.2: Sensitivity as function of source to collimator distance

In table 8.1 and 8.2 the values of the spatial resolution and sensitivity have been reported.

a) Standard geometry 0.2 mm septa (Tungsten)

b) Standard geometry 0.4 mm septa (Tungsten)

c) Standard geometry 0.4 mm septa (PLA Virtual Foundry)

d) Novel geometry 0.4 mm septa (PLA)

e) Novel geometry 0.4 mm septa (PA2200)

f) Novel geometry M.A.D.E 0.4 mm septa (PLA)

Table 8.1: Simulated spatial resolution (SR) at different source to collimator distances

| **Spatial Resolution (mm)** | | | | | | |
|---|---|---|---|---|---|---|
| **Distance (mm)** | **SR (a) mm** | **SR (b) mm** | **SR (c) mm** | **SR(d) mm** | **SR(e) mm** | **SR(f) mm** |
| 5 | 2,63 | 2,55 | 2,65 | 2,64 | 2,50 | 2,58 |
| 10 | 2,78 | 2,65 | 2,68 | 2,60 | 2,66 | 2,64 |
| 20 | 2,95 | 2,99 | 2,95 | 3,01 | 2,92 | 2,89 |
| 30 | 3,31 | 3,25 | 3,38 | 3,37 | 3,50 | 3,16 |

Observing the simulated results, what is immediately evident is that the spatial resolution is not greatly affected by the novel concept geometry of the collimator. We do not experience variations so important due to the presence of PLA and PA2200 used for the extruded pixels in the novel concept geometry. Considering the spatial resolutions computed at 5 mm source to collimator distance for the different configurations, we get a $\mu$ of 2,591 mm with a $\sigma$ of $\pm$0,059 mm.

Table 8.2: Simulated sensitivity (S) at different source to collimator distances

| Sensitivity (cps/MBq) | | | | | | |
|---|---|---|---|---|---|---|
| **Distance (mm)** | **S (a)** | **S (b)** | **S (c)** | **S (d)** | **S (e)** | **S (f)** |
| 5 | 45,54 | 36,81 | 38,35 | 17,47 | 19,94 | 16,48 |
| 10 | 46,41 | 35,33 | 37,11 | 16,18 | 18,88 | 16,75 |
| 20 | 46,61 | 34,36 | 35,93 | 15,83 | 19,55 | 15,72 |
| 30 | 46,49 | 34,70 | 35,97 | 15,59 | 18,44 | 16,27 |

The other mean and standard deviation values according to the other distances are reported in Table 8.3. Instead, looking at the sensitivity values, is clear that as we

Table 8.3: Spatial resolution mean and standard deviation at different source to collimator distances of the simulated configurations

| **Distance (mm)** | $\mu$ | $\pm\sigma$ |
|---|---|---|
| 5 | 2,591 | 0,059 |
| 10 | 2,668 | 0,060 |
| 20 | 2,951 | 0,046 |
| 30 | 3,328 | 0,117 |

supposed, the PLA and the PA2200 tend to affect, in a really important way, the measurement characteristics of the imaging device. As stated before, the PLA and PA2200 show a density equal to ∼1.24 g/cm$^3$ for PLA and ∼0.95 g/cm$^3$ for PA2200. This density, higher than the air density (∼0.0012 g/cm3) tends to create an absorbing path for gamma-rays, reducing the number of those photons impacting onto the detector.
The 0.4 mm septa collimator configuration with real tungsten shows the 80% of sensitivity with respect to the standard one at 5 mm source to collimator distance. The configuration with 0.4 mm septa with the Virtual Foundry's PLA shows the 84% in sensitivity. The two configurations with the simulated extruded holes in PLA and PA2200 show respectively ∼38% and ∼43% at 5 mm, with respect to the reference configuration with 0.2 mm septa. Lastly, the configuration with the PLA grid at half of its height and with the holes extruded in PLA shows a ∼36% with respect to the reference configuration.
The decrease in sensitivity we experienced is due to the higher density of the plastic materials used in the additive manufacturing process in combination with the increase of the septa thickness. Indeed, increasing the septa, as we have seen in Figure 5.3, we get that the septa tends to cover active area of the underneath crystals causing a decrease in efficiency and so in the record of the incoming photons.
In table 8.4 the sensitivity percentage at all the source to collimator distances are reported. In the images below (Figure 8.3) have been reported the energy spectrum of $^{99}$Tc obtained using the different collimator configurations at a source to collimator distance equal to 5 mm.
As it is possible to see from the images below, where the energy spectrum of $^{99}$Tc is reported, according to the material used for the collimator we get a big decrease in the number of entries and so in the number of recorded photons. It is appreciable also the effect of increasing the septa thickness or the presence of the PLA grid at half of the height of the printed sample.

Table 8.4: Sensitivity percentage of simulated collimators with respect to the reference one

| **Sensitivity percentage Tc99m** | | | | | |
|---|---|---|---|---|---|
| **Distance (mm)** | **% (b)** | **% (c)** | **% (d)** | **% (e)** | **% (f)** |
| 5 | 80,83 | 84,21 | 38,36 | 43,79 | 36,19 |
| 10 | 76,13 | 79,96 | 34,86 | 40,68 | 36,09 |
| 20 | 73,72 | 77,09 | 33,96 | 41,94 | 33,73 |
| 30 | 74,64 | 77,37 | 33,53 | 39,66 | 35,00 |

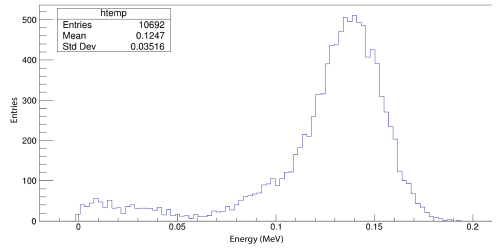


(a) SG 0.2 mm septa

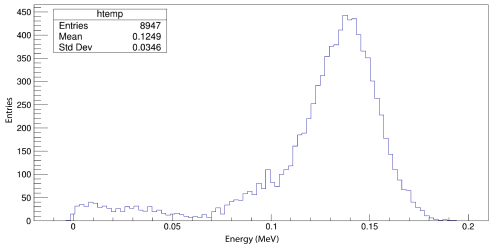


(b) SG 0.4 mm septa

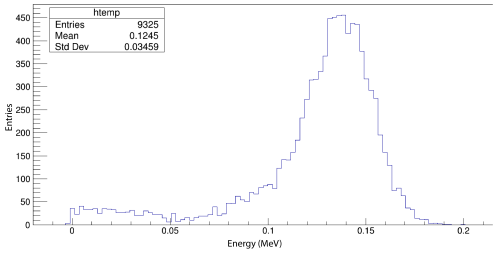


(c) SG 0.4 mm septa PLA Virtual Foundry

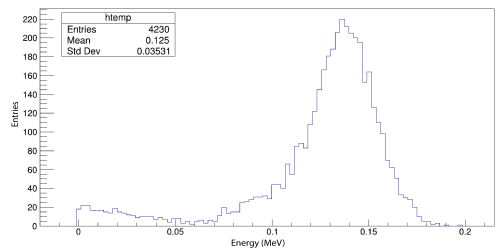


(d) NG 0.4 mm septa PLA

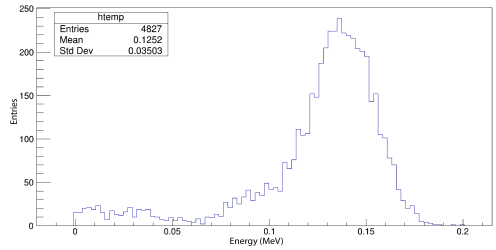


(e) NG 0.4 mm septa PA2200

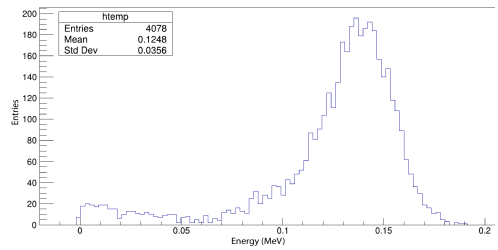


(f) NG 0.4 mm septa PLA M.A.D.E

Figure 8.3: Energy spectrum $^{99}$Tc. SG = Standard geometry and NG = Novel geometry concept

In Figure 8.4 the radioactive capillary source as viewed by the different collimators configurations is reported. The capillary source has been visualized after applying an energy window of ±20% around the energy peak of 140 keV. In this way we are able to remove part of the background foggy disturb created by the backscatter radiation.

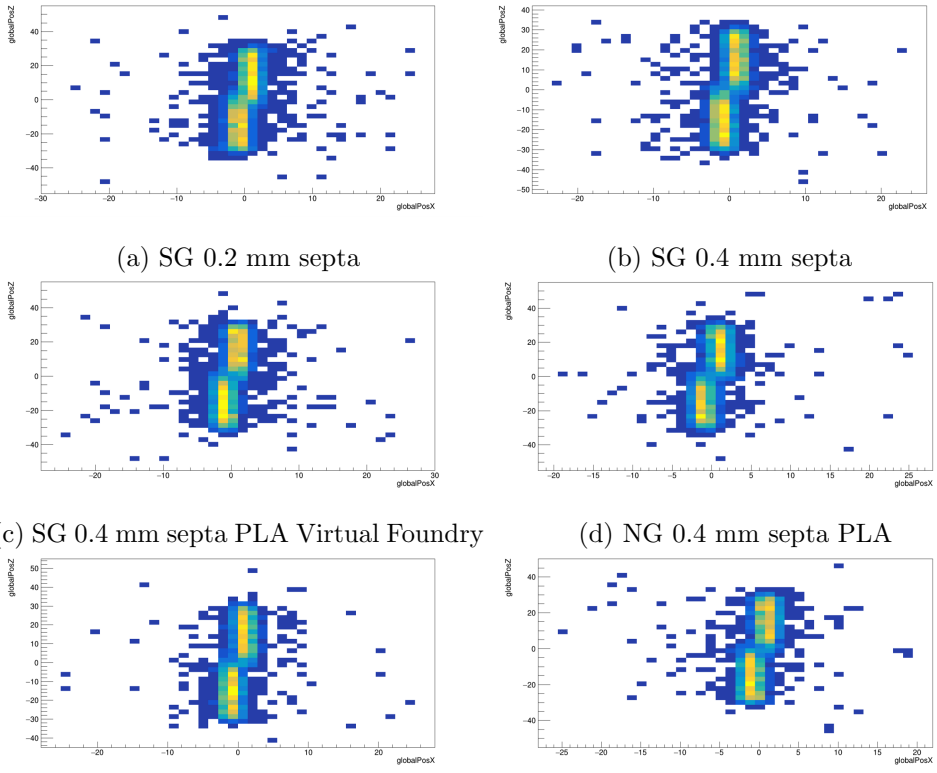


(a) SG 0.2 mm septa

(b) SG 0.4 mm septa

(c) SG 0.4 mm septa PLA Virtual Foundry

(d) NG 0.4 mm septa PLA

(e) NG 0.4 mm septa PA2200

(f) NG 0.4 mm septa PLA M.A.D.E

Figure 8.4: Capillary radiocative source $^{99}$Tc. SG = Standard geometry and NG = Novel geometry concept

Finally, in Figure 8.5 the gaussian fitting computed for each capillary source is reported.

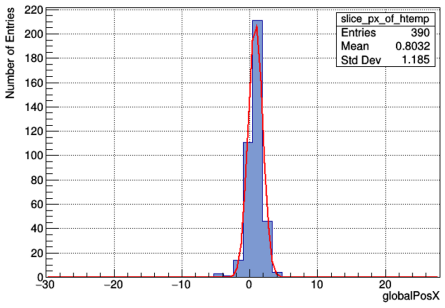


(a) SG 0.2 mm septa

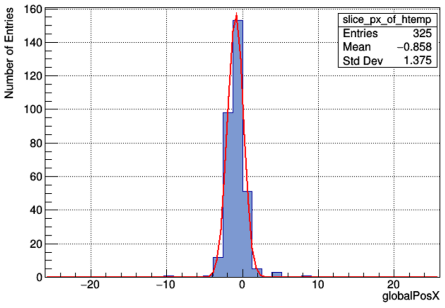


(b) SG 0.4 mm septa

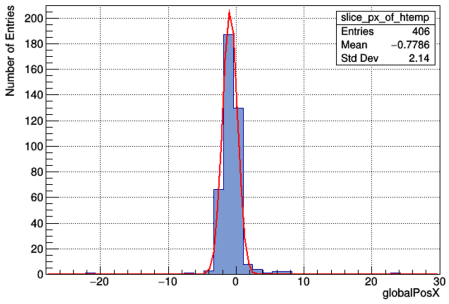


(c) SG 0.4 mm septa PLA Virtual Foundry

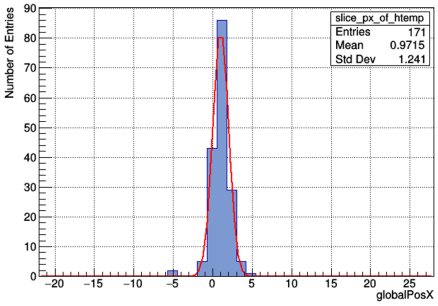


(d) NG 0.4 mm septa PLA

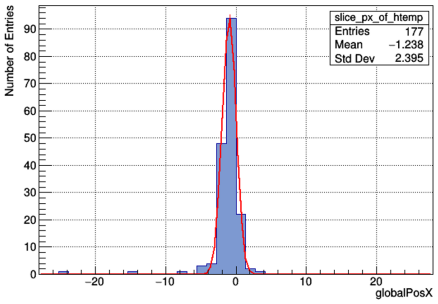


(e) NG 0.4 mm septa PA2200

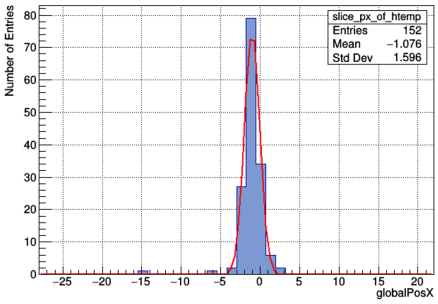


(f) NG 0.4 mm septa PLA M.A.D.E

Figure 8.5: Capillary radiocative source $^{99}$Tc curve fitting. SG = Standard geometry and NG = Novel geometry concept. The inset of each figure is referred to relative histogram

The sigma values obtained by fitting the histogram with the gaussian curve are reported in the table 8.5. The values have been rounded at the second decimal place. These sigma values have been then used, as explained previously, to compute the spatial resolution multiplying it by 2,35.

Table 8.5: Gaussian fitting *sigma* at different source to collimator distances

| **Gaussian Fit Sigma for Tc99m** | | | | | | |
|---|---|---|---|---|---|---|
| **Distance (mm)** | $\sigma$ **(a)** | $\sigma$ **(b)** | $\sigma$ **(c)** | $\sigma$**(d)** | $\sigma$**(e)** | $\sigma$**(f)** |
| 5 | 1,12 | 1,08 | 1,13 | 1,12 | 1,06 | 1,10 |
| 10 | 1,18 | 1,13 | 1,14 | 1,10 | 1,13 | 1,12 |
| 20 | 1,25 | 1,27 | 1,25 | 1,28 | 1,24 | 1,23 |
| 30 | 1,41 | 1,38 | 1,44 | 1,43 | 1,48 | 1,34 |

## 8.2 Optimized collimator concept

The numerical simulation set-up for the optimized collimator concept has been defined using always the $\gamma$-eye$^{TM}$ system GATE configuration. The optimized collimator geometry has been then inserted and the measurement characteristics of the imaging system have been evaluated. In this case we simulated directly the optimized reference geometry and then we proceeded to evaluate the measurement properties of the optimized collimator additively manufactured in PLA and PA2200. We also evaluate the performance of the 3D model reconstructed by means of the imaging system mounted on-board of the Ender 5 Plus 3D printer, in order to see how and if the printing error, effectively reproduced and imported in GATE software, influenced the performance of the nuclear imaging device. We simulated three different radioisotopes in GATE; $^{99}$Tc, Lu177, Ga67 and In111. The computation of spatial resolution and sensitivity for the Lu177 and In111 and Ga67 radioisotopes have been done considering the principal photon emission peaks.

### 8.2.1 Tc99 isotope simulation

In Figure 8.6 the spatial resolution for the three simulated configurations of the optimized collimator concept are reported. We defined a simulation also for the 3D reconstructed model as previously said. The reconstructed model represents a small portion of the real collimator and for this reason we got, as we will see later, less entries in terms of photons recording, but this does not affect the spatial resolution computation. Instead in Figure 8.7 the sensitivity is reported.

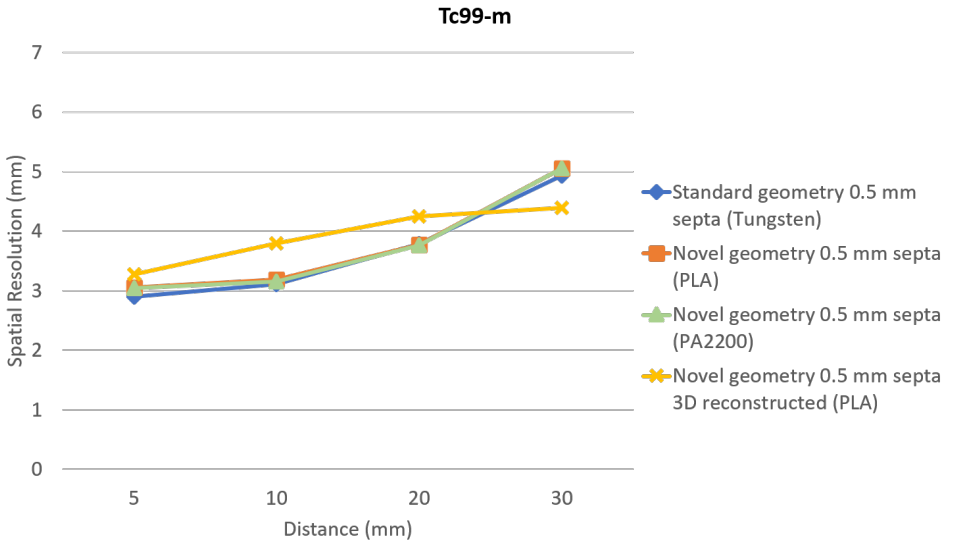


Figure 8.6: Spatial resolution as function of source to collimator distance

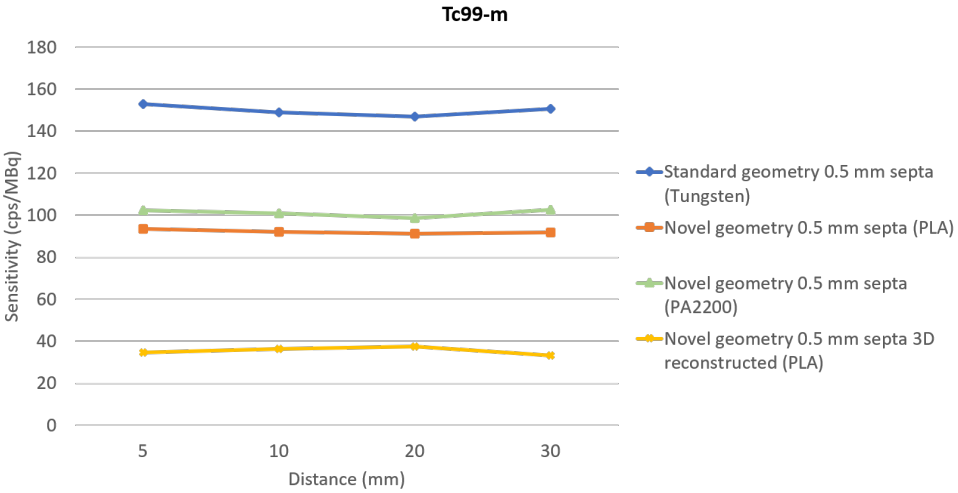


Figure 8.7: Sensitivity as function of source to collimator distance

Looking at the spatial resolution graph it is possible to highlight immediately how the standard geometry collimator and the PLA and PA2200 novel concept show the same behavior in terms of spatial resolution attesting around the same values. This trend demonstrate that, as for the first concept collimator, the introduction of plastic extruded pixels do not affect the spatial resolution. However, as already introduced in the description of the optimized collimator concept, reducing the hole length and increasing the hole diameter and septa tend to increase the measured value of spatial resolution, meaning a worsening of spatial resolution itself. But, on the other hand we experienced an important increase in photons recording passing from 45,54 cps/MBq for the reference configuration at 5 mm source to collimator distance, to

153,05 cps/MBq for the optimized reference geometry always at 5 mm source to collimator distance. We got now ∼70% more recording photons than what we achieved with the first concept collimator. Indeed, as already said, increasing the hole diameter and decreasing the hole length we worsening the spatial resolution but at the same time we greatly increase the efficiency of the system in acquiring a bigger percentage of incoming photons.
Instead, the yellow line refers to the values simulated for the 3D reconstructed model. The model imported in GATE and simulated, reports all the printing defects such as fused extruded pixels that became one, non parallelism betweeen the pixels, bigger pixel in diameter with respect to other and non-square section of the printed pixel itself. All these defects, hard to reproduce in GATE, allow us to see how effectively the printed sample would behave. The first thing we can see looking at Figure 8.6 is that we experience a worsening in the spatial resolution not indifferent if compared to the optimized geometries created directly in GATE. The sensitivity, on the other hand, as already said, has a much lower value with respect to the PLA and PA2200 samples, specially because having printed only a small portion of the real collimator system, in GATE we imported and simulated only it.

In table 8.6 and 8.7 the values of the spatial resolution and sensitivity for the optimized collimator concept have been reported.

a) Standard geometry 0.5 mm septa (Tungsten)

b) Novel geometry 0.5 mm septa (PLA)

c) Novel geometry 0.5 mm septa (PA2200)

d) Novel geometry 0.5 mm septa 3D reconstructed collimator (PLA)

Table 8.6: Simulated spatial resolution (SR) at different source to collimator distances for Tc99

| **Spatial resolution (mm)** | | | | |
|---|---|---|---|---|
| **Distance (mm)** | **SR (a) mm** | **SR (b) mm** | **SR (c) mm** | **SR (d) mm** |
| 5 | 2,90 | 3,05 | 3,04 | 3,28 |
| 10 | 3,11 | 3,19 | 3,15 | 3,79 |
| 20 | 3,78 | 3,77 | 3,76 | 4,25 |
| 30 | 4,93 | 5,06 | 5,05 | 4,39 |

Table 8.7: Simulated sensitivity (S) at different source to collimator distances for Tc99

| **Sensitivity (cps/MBq)** | | | | |
|---|---|---|---|---|
| **Distance (mm)** | **S (a)** | **S (b)** | **S (c)** | **S (d)** |
| 5 | 153,05 | 93,52 | 102,33 | 34,57 |
| 10 | 148,89 | 92,11 | 101,01 | 36,41 |
| 20 | 147,02 | 91,21 | 98,58 | 37,44 |
| 30 | 150,61 | 91,90 | 102,64 | 33,29 |

The optimized collimator concept show a good behavior in terms of spatial resolution with respect to the reference one, also the simulated model from the 3D reconstruction with all its defects. Considering the spatial resolutions computed at 5 mm source to collimator distance for the different configurations, we get a $\mu$ of 3,067 mm with a $\sigma$ of $\pm$0,157 mm.
For what concern the sensitivity we experienced the same behavior as previously experienced with the first collimator concept. This confirm the effects of the plastic extruded pixels on the efficiency in recording the impacting photons. The two configurations with the simulated extruded holes in PLA and PA2200 show respectively $\sim$61% and $\sim$66% of sensitivity at 5 mm, with respect to the reference configuration with 0.5 mm septa. In table 8.9 the sensitivity percentage at all the source to collimator distances are reported. The values regarding the reconstructed model show so big difference because, as previously explained, we printed only a small portion of the real collimator and so we got only a small model to test in GATE, resulting in a lower sensitivity due to the smaller active area.

In Table 8.8 the other mean and standard deviation at different source to collimator distances have been reported.

Table 8.8: Spatial resolution mean and standard deviation at different source to collimator distances of the simulated configurations

| **Distance (mm)** | $\mu$ | $\pm\sigma$ |
|---|---|---|
| 5 | 3,067 | 0,157 |
| 10 | 3,31 | 0,321 |
| 20 | 3,89 | 0,240 |
| 30 | 4,857 | 0,317 |

Table 8.9: Sensitivity percentage of optimized simulated collimators with respect to the reference one

| **Sensitivity percentage Tc99m** | | | |
|---|---|---|---|
| **Distance (mm)** | **% (b)** | **% (c)** | **% (d)** |
| 5 | 61,10 | 66,86 | 22,59 |
| 10 | 61,86 | 67,84 | 24,45 |
| 20 | 62,04 | 67,05 | 25,47 |
| 30 | 61,02 | 68,15 | 22,10 |

In the images below (Figure 8.8) have been reported the energy spectrum of $^{99}$Tc obtained using the different optimized collimator configurations at a source to collimator distance equal to 5 mm.

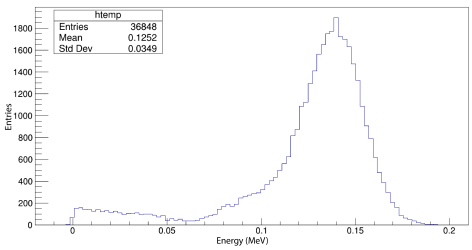


(a) SG 0.5 mm septa

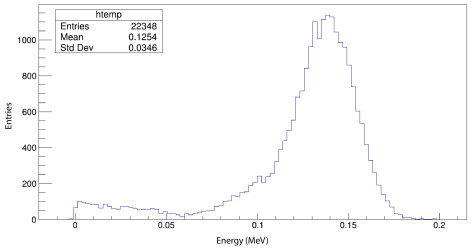


(b) NG 0.5 mm septa PLA

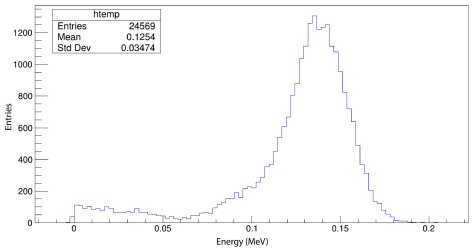


(c) NG 0.5 mm septa PA2200

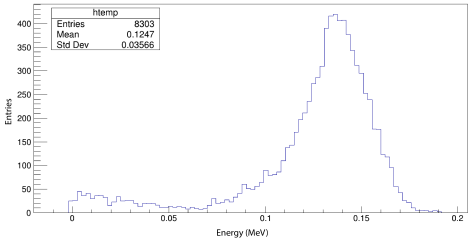


(d) NG 0.5 mm septa 3D model PLA

Figure 8.8: Energy spectrum $^{99}$Tc. SG = Standard geometry and NG = Novel geometry concept

In Figure 8.9 the radioactive capillary source as viewed by the different collimators configurations is reported. The capillary source has been visualized after applying an energy window of ±20% around the energy peak of 140 keV. In this way we are able to remove part of the background foggy disturb created by the backscatter radiation.

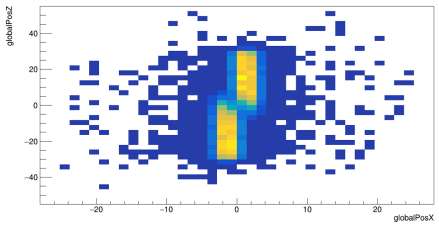


(a) SG 0.5 mm septa

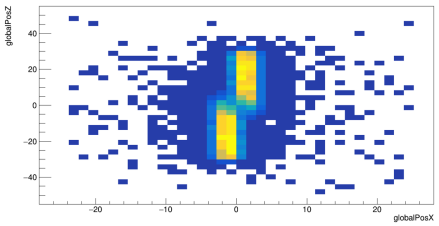


(b) NG 0.5 mm septa PLA

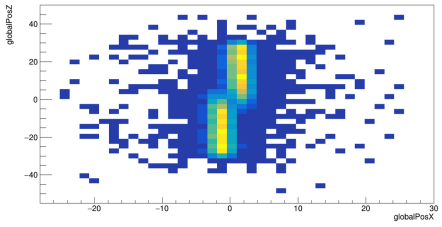


(c) NG 0.5 mm septa PA2200

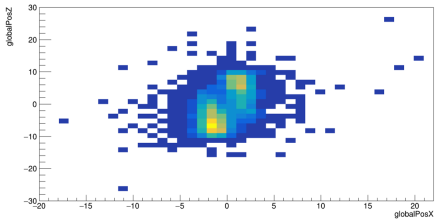


(d) NG 0.5 mm septa 3D model PLA

Figure 8.9: Capillary radioactive source $^{99}$Tc. SG = Standard geometry and NG = Novel geometry concept

The capillary viewed by the 3D reconstructed model is, as previously said, only a portion of the actual capillary viewed using the other configurations simulated because the reconstructed model is only a portion of the real one.

In Figure 8.10 the curve fitting computed for each capillary source are reported.

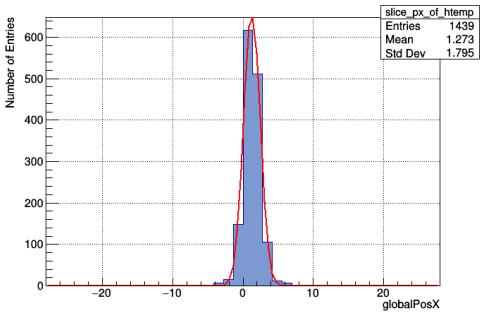


(a) SG 0.5 mm septa

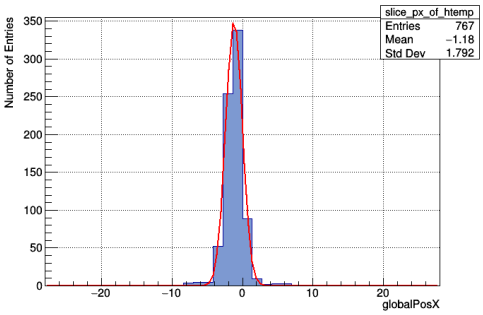


(b) NG 0.5 mm septa PLA

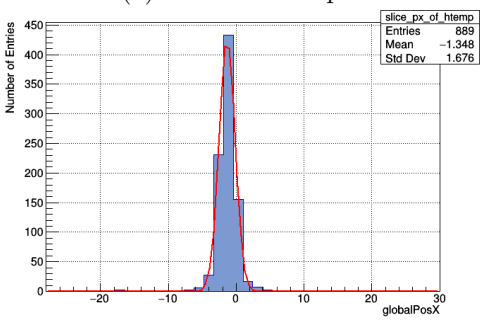


(c) NG 0.5 mm septa PA2200

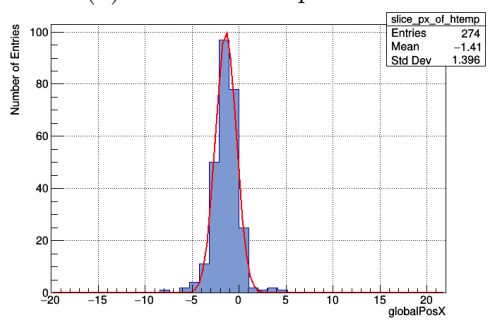


(d) NG 0.5 mm septa 3D model PLA

Figure 8.10: Gaussian fit $^{99}$Tc. SG = Standard geometry and NG = Novel geometry concept. The inset of each figure is referred to relative histogram

The sigma values obtained by fitting the histogram with the gaussian curve are reported in the table 8.10. The values have been rounded at the second decimal place. These sigma values have been then used, as explained previously, to compute the spatial resolution multiplying it by 2,35.

Table 8.10: Gaussian fitting sigma values at different source to collimator distances

| **Gaussian Fit Sigma for Tc99m** | | | | |
|---|---|---|---|---|
| **Distance (mm)** | $\sigma$ **(a)** | $\sigma$ **(b)** | $\sigma$ **(c)** | $\sigma$ **(d)** |
| 5 | 1,23 | 1,30 | 1,30 | 1,40 |
| 10 | 1,32 | 1,36 | 1,34 | 1,61 |
| 20 | 1,61 | 1,60 | 1,60 | 1,81 |
| 30 | 2,10 | 2,15 | 2,15 | 1,87 |

### 8.2.2 Lu177 isotope simulation

For the Lu177 as for the other higher energy isotopes, we defined simulation highlighting each time the energy of reference to consider in the simulation macro. This energy of reference is dependent on the energy peak where we got the principal photons emission.

#### Lu177 - 113 keV

In Figure 8.11 the spatial resolution for the three simulated configurations of the optimized collimator concept are reported. Instead in Figure 8.12 the sensitivity is reported. The below figures refers to the simulation of Lu177 with energy of reference of 113 keV.

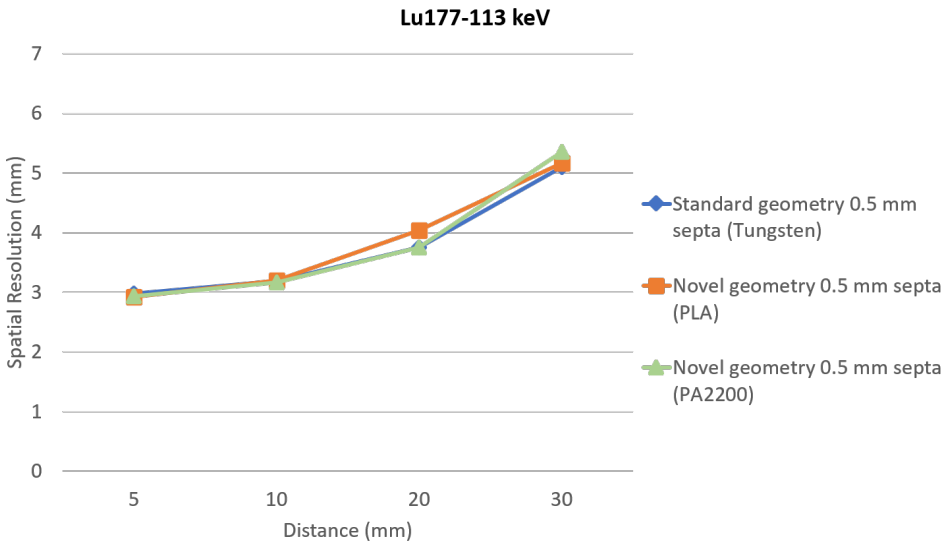


Figure 8.11: Spatial resolution as function of source to collimator distance

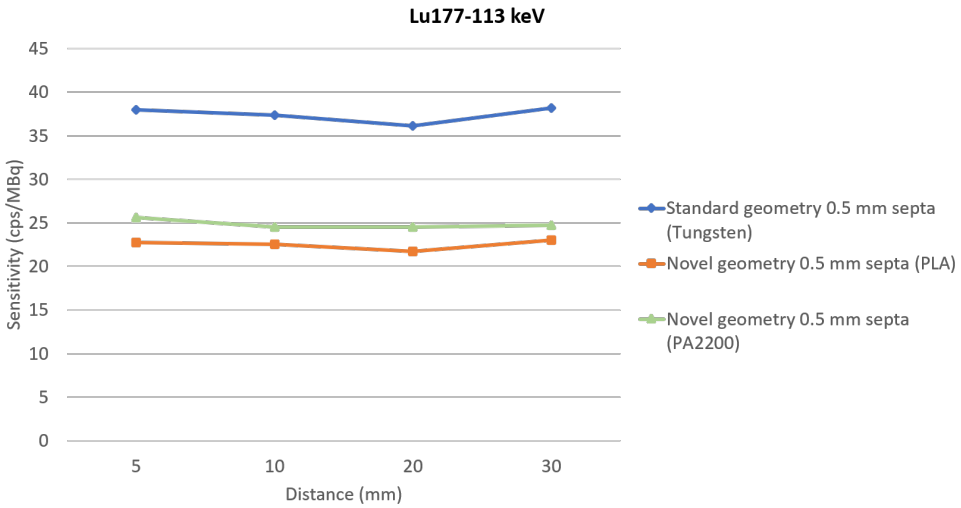


Figure 8.12: Sensitivity as function of source to collimator distance

Looking at the spatial resolution graph it is possible to highlight immediately that, as for the $^{99}$Tc, the standard geometry collimator and the PLA and PA2200 novel concept have values of resolution similar among them. The sensitivity graph instead show an important decrease in photons recording if compared to the sensitivity measured with $^{99}$Tc. This is due to the fact that the intensity of the 140 keV of $^{99}$Tc has an energy emission percentage of almost ∼90%. The Lu177 instead at 113 keV and 208 keV has a really low emission percentage of almost ∼6% and ∼10% respectively. So, simulating the same activity for all the isotopes we experienced in this case a low record of entries with respect to $^{99}$Tc or In111 for example.

In table 8.11 and 8.12 the values of the spatial resolution and sensitivity for the optimized collimator concept have been reported.

a) Standard geometry 0.5 mm septa (Tungsten)

b) Novel geometry 0.5 mm septa (PLA)

c) Novel geometry 0.5 mm septa (PA2200)

Table 8.11: Simulated spatial resolution (SR) at different source to collimator distances for Lu177 - 113 keV

| **Spatial resolution (mm)** | | | |
|---|---|---|---|
| **Distance (mm)** | **SR (a) mm** | **SR (b) mm** | **SR (c) mm** |
| 5 | 2,98 | 2,92 | 2,93 |
| 10 | 3,19 | 3,20 | 3,17 |
| 20 | 3,75 | 4,04 | 3,75 |
| 30 | 5,10 | 5,17 | 5,35 |

Table 8.12: Simulated sensitivity (S) at different source to collimator distances for Lu177 - 113 keV

| **Sensitivity (cps/MBq)** | | | |
|---|---|---|---|
| **Distance (mm)** | **S (a) mm** | **S (b) mm** | **S (c) mm** |
| 5 | 38,00 | 22,76 | 25,63 |
| 10 | 37,37 | 22,52 | 24,53 |
| 20 | 36,17 | 21,74 | 24,50 |
| 30 | 38,19 | 23,04 | 24,75 |

The optimized collimator concept show a good behavior in terms of spatial resolution with respect to the reference one. Considering the spatial resolutions computed at 5 mm source to collimator distance for the different configurations, we get a $\mu$ of 2,943 mm with a $\sigma$ of $\pm$0,032 mm. For what concern the sensitivity we experienced the same behavior as previously experienced. The PA2200 material, having a lower density ($\sim$0.95g/cm$^3$) with respect to the PLA ($\sim$1.24g/cm$^3$) guarantees a better transmissibility of the incoming photons, resulting in a better sensitivity. Indeed, we achieved almost $\sim$59% for the PLA collimator concept and almost $\sim$67% for the PA2200 of sensitivity at 5 mm source to collimator distance, with respect to the reference configuration with 0.5 mm septa. In table 8.14 the sensitivity percentage at all the source to collimator distances are reported.

In Table 8.13 the other mean and standard deviation for all the source to collimator distances are reported.

Table 8.13: Spatial resolution mean and standard deviation at different source to collimator distances of the simulated configurations for Lu177 - 113 keV

| **Distance** | $\mu$ | $\pm\sigma$ |
|---|---|---|
| 5 | 2,943 | 0,032 |
| 10 | 3,186 | 0,015 |
| 20 | 3,846 | 0,167 |
| 30 | 5,206 | 0,128 |

Table 8.14: Sensitivity percentage of optimized simulated collimators with respect to the reference one

| **Sensitivity percentage Lu177-113 keV** | | |
|---|---|---|
| **Distance (mm)** | **% (b)** | **% (c)** |
| 5 | 59,89 | 67,45 |
| 10 | 60,26 | 65,64 |
| 20 | 60,11 | 67,74 |
| 30 | 60,33 | 64,81 |

In Figure 8.13 has been reported the energy spectrum of Lu177 obtained setting the reference energy at 113 keV at a source to collimator distance equal to 5 mm. In Figure 8.14 instead the capillary source as viewed by the three configuration is reported.

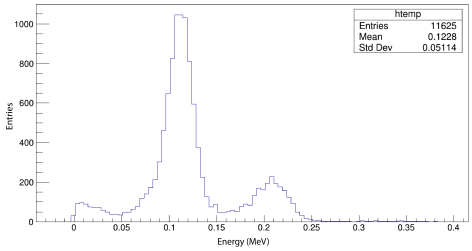


(a) SG 0.5 mm septa

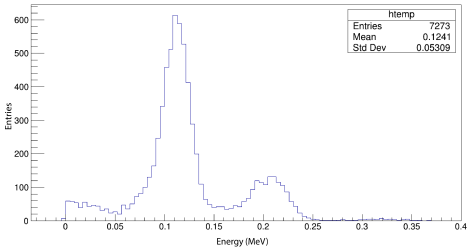


(b) NG 0.5 mm septa PLA

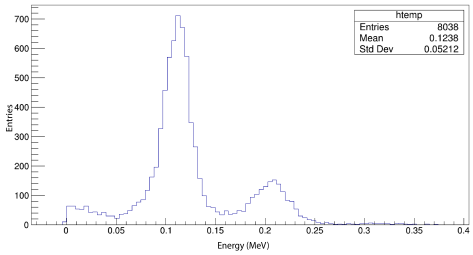


(c) NG 0.5 mm septa PA2200

Figure 8.13: Energy spectrum of Lu177 - 113 keV. SG = Standard geometry and NG = Novel geometry concept

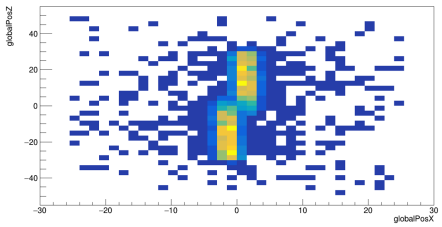


(a) SG 0.5 mm septa

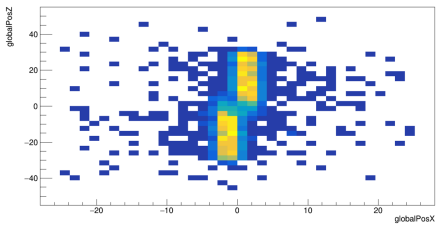


(b) NG 0.5 mm septa PLA

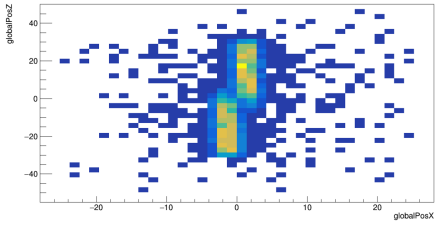


(c) NG 0.5 mm septa PA2200

Figure 8.14: Capillary radioactive source Lu177 - 113 keV. SG = Standard geometry and NG = Novel geometry concept

Finally, in Figure 8.15 the gaussians fit of the capillary source profile for the computation of the spatial resolution are reported.

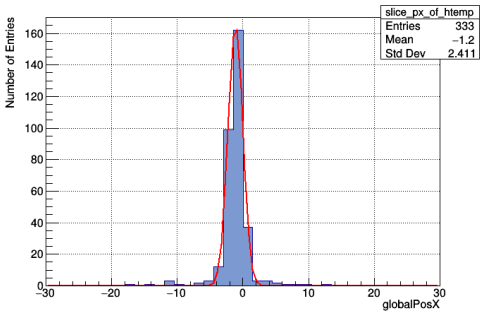


(a) SG 0.5 mm septa

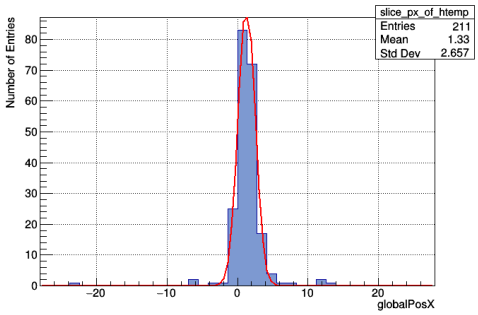


(b) NG 0.5 mm septa PLA

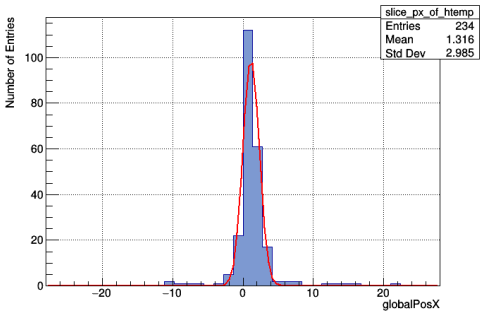


(c) NG 0.5 mm septa PA2200

Figure 8.15: Gaussian fit Lu177 - 113 keV. SG = Standard geometry and NG = Novel geometry concept. The inset of each figure is referred to relative histogram

The sigma values obtained by fitting the histogram with the gaussian curve are reported in the table 8.15. The values have been rounded at the second decimal place. These sigma values have been then used, as explained previously, to compute the spatial resolution multiplying it by 2,35.

Table 8.15: Gaussian fitting sigma values at different source to collimator distances

| **Gaussian Fit Sigma for Lu177-113 keV** | | | |
|---|---|---|---|
| **Distance (mm)** | $\sigma$ **(a)** | $\sigma$ **(b)** | $\sigma$ **(c)** |
| 5 | 1,27 | 1,24 | 1,25 |
| 10 | 1,36 | 1,36 | 1,35 |
| 20 | 1,60 | 1,72 | 1,60 |
| 30 | 2,17 | 2,20 | 2,28 |

### Lu177 - 208 keV

We then simulated the same isotope using as energy of reference the 2008 keV energy peak. In Figure 8.16 and 8.17 respectively the spatial resolution and the sensitivity are reported. In Table 8.16 and 8.17 are reported respectively the spatial resolution and sensitivity computed using the the above mentioned energy reference peak.

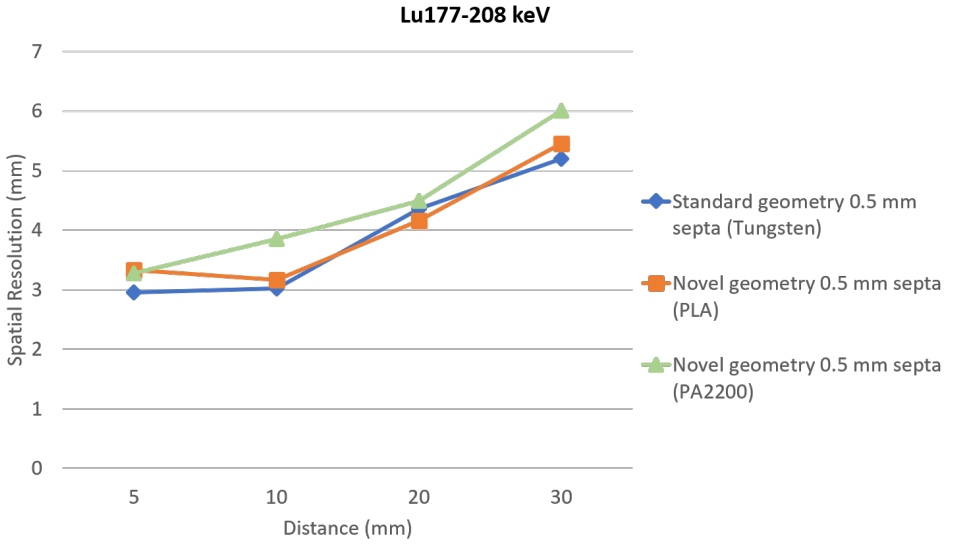


Figure 8.16: Spatial resolution as function of source to collimator distance

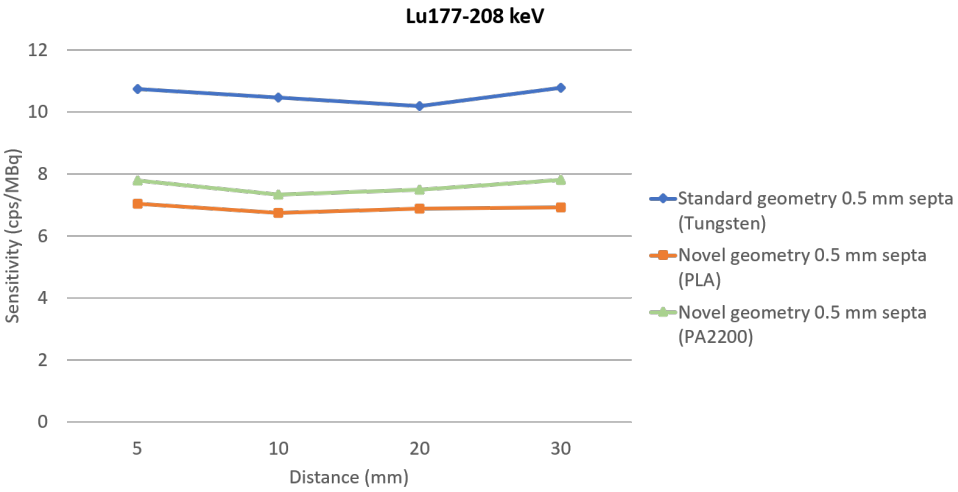


Figure 8.17: Sensitivity as function of source to collimator distance

Table 8.16: Simulated spatial resolution (SR) at different source to collimator distances for Lu177 - 208 keV

| **Spatial resolution (mm)** | | | |
|---|---|---|---|
| **Distance (mm)** | **SR (a) mm** | **SR (b) mm** | **SR (c) mm** |
| 5 | 2,96 | 3,33 | 3,28 |
| 10 | 3,02 | 3,16 | 3,85 |
| 20 | 4,36 | 4,16 | 4,49 |
| 30 | 5,20 | 5,45 | 6,01 |

Table 8.17: Simulated sensitivity (S) at different source to collimator distances for Lu177 - 208 keV

| **Sensitivity (cps/MBq)** | | | |
|---|---|---|---|
| **Distance (mm)** | **S (a) mm** | **S (b) mm** | **S (c) mm** |
| 5 | 10,73 | 7,04 | 7,79 |
| 10 | 10,47 | 6,74 | 7,33 |
| 20 | 10,19 | 6,89 | 7,50 |
| 30 | 10,78 | 6,91 | 7,81 |

The spatial resolutions computed at 5 mm source to collimator distance for the different configurations gave us a $\mu$ of 3,19 mm with a $\sigma$ of $\pm$0,200 mm. For what concern the sensitivity instead, the PLA sample showed almost $\sim$65% with respect to the reference configuration while the PA2200 almost $\sim$72%. In table 8.19 the sensitivity percentage at all the source to collimator distances are reported.

In Table 8.18 the other mean and standard deviation values are reported.

Table 8.18: Spatial resolution mean and standard deviation at different source to collimator distances of the simulated configurations for Lu177 - 208 keV

| **Distance** | $\mu$ | $\pm\sigma$ |
|---|---|---|
| 5 | 3,190 | 0,200 |
| 10 | 3,343 | 0,444 |
| 20 | 4,336 | 0,166 |
| 30 | 5,553 | 0,414 |

Table 8.19: Sensitivity percentage of optimized simulated collimators with respect to the reference one

| **Sensitivity percentage Lu177-208 keV** | | |
|---|---|---|
| **Distance (mm)** | **% (b)** | **% (c)** |
| 5 | 65,61 | 72,60 |
| 10 | 64,37 | 70,01 |
| 20 | 67,62 | 73,60 |
| 30 | 64,10 | 72,45 |

In Figure 8.18 the energy spectrum for Lu177 with energy of reference of 208 keV is reported.

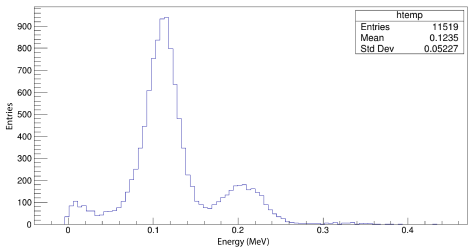


(a) SG 0.5 mm septa

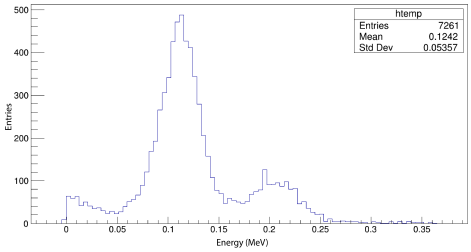


(b) NG 0.5 mm septa PLA

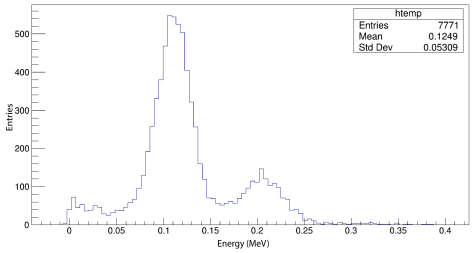


(c) NG 0.5 mm septa PA2200

Figure 8.18: Energy spectrum Lu177 - 208 keV. SG = Standard geometry and NG = Novel geometry concept

In Figure 8.19 and 8.20 the capillary source and the gaussian fit for Lu177 with energy of reference of 208 keV at 5 mm source to collimator distance are reported.

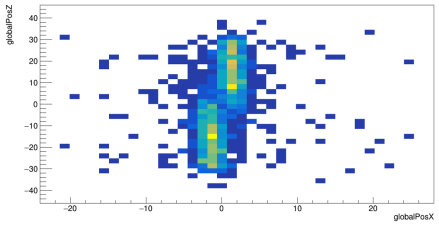


(a) SG 0.5 mm septa

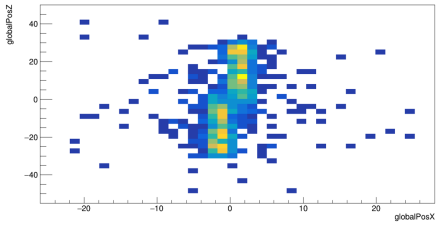


(b) NG 0.5 mm septa PLA

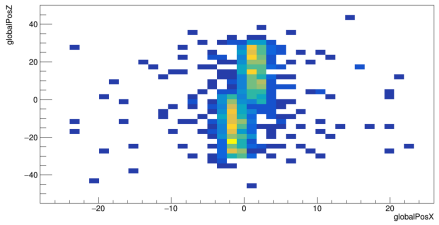


(c) NG 0.5 mm septa PA2200

Figure 8.19: Capillary radioactive source Lu177 - 208 keV. SG = Standard geometry and NG = Novel geometry concept

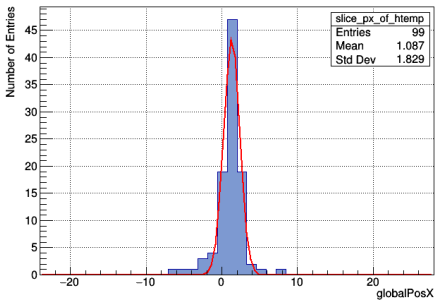


(a) SG 0.5 mm septa

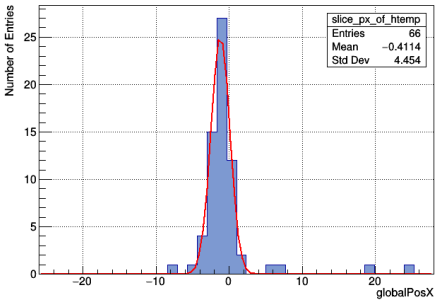


(b) NG 0.5 mm septa PLA

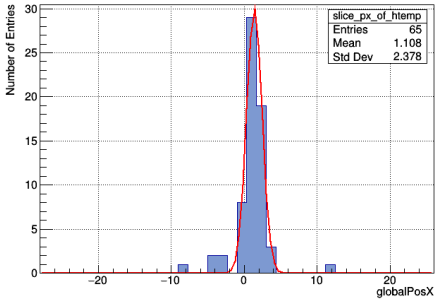


(c) NG 0.5 mm septa PA2200

Figure 8.20: Gaussian fit Lu177 - 208 keV. SG = Standard geometry and NG = Novel geometry concept. The inset of each figure is referred to relative histogram

The sigma values obtained by fitting the histogram with the gaussian curve are reported in the table 8.20. The values have been rounded at the second decimal place. These sigma values have been then used, as explained previously, to compute the spatial resolution multiplying it by 2,35.

Table 8.20: Gaussian fitting sigma values at different source to collimator distances

| **Gaussian Fit Sigma for Lu177-208 keV** | | | |
|---|---|---|---|
| **Distance (mm)** | **$\sigma$ (a)** | **$\sigma$ (b)** | **$\sigma$ (c)** |
| 5 | 1,26 | 1,42 | 1,40 |
| 10 | 1,28 | 1,34 | 1,64 |
| 20 | 1,85 | 1,77 | 1,91 |
| 30 | 2,21 | 2,32 | 2,55 |

### 8.2.3 In111 isotope simulation

For the In111 we have two different energy of reference to take in consideration tat are 171 keV and 245 keV that show respectively almost ∼91% and ∼94% of photon emission.

#### In111 - 171 keV

In Figure 8.21 the spatial resolution for the three simulated configurations of the optimized collimator concept are reported using In111 as isotope. Instead in Figure 8.22 the sensitivity is reported.

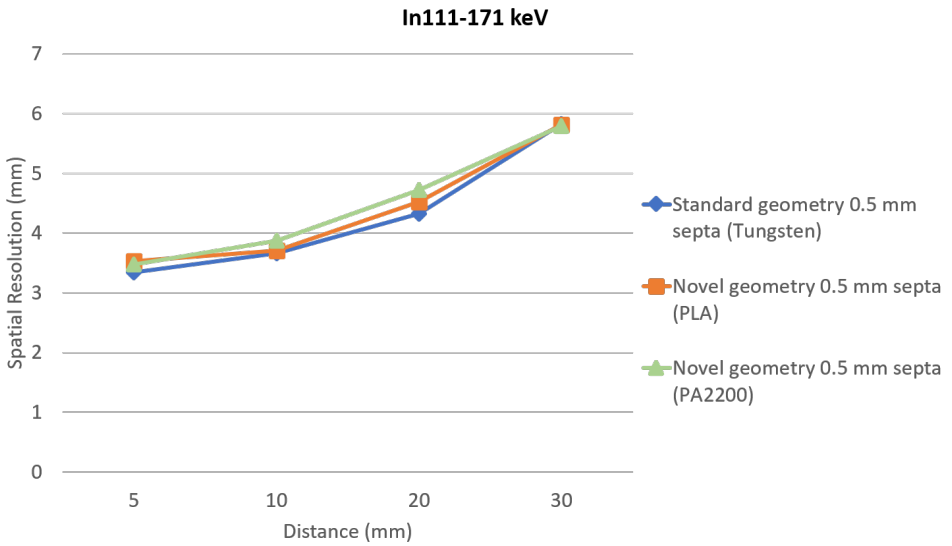


Figure 8.21: Spatial resolution as function of source to collimator distance

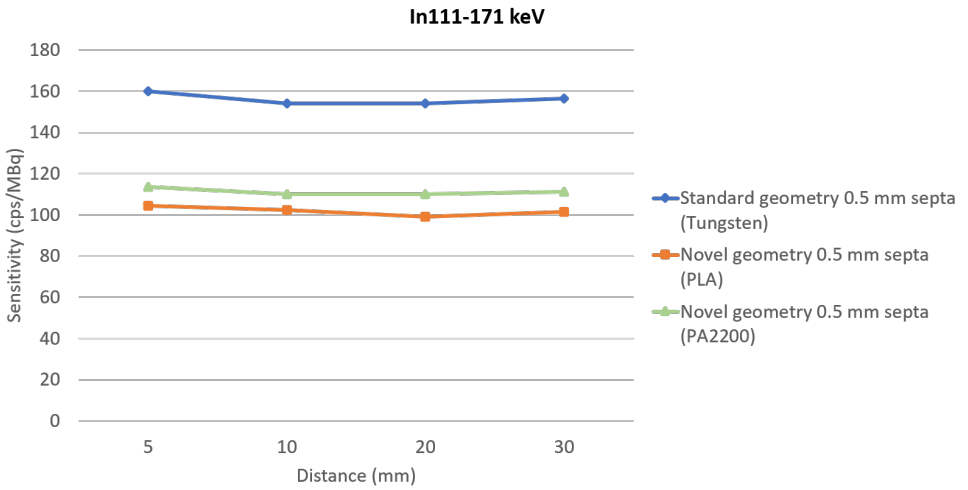


Figure 8.22: Sensitivity as function of source to collimator distance

In Table 8.21 the spatial resolution values are highlighted, while in Table 8.22 the sensitivity is reported. For the spatial resolution at 5 mm source to collimator distance we get a $\mu$ of 3,446 mm and a $\sigma$ of $\pm$0,097. The sensitivity showed by the two novel concept collimator with the extruded plastic pixels is respectively almost $\sim$65% for the PLA concept and almost $\sim$71% for the PA2200 concept. In table 8.24 the sensitivity percentage at all the source to collimator distances are reported.

In Table 8.23 the other values of mean and standard deviation are reported.

Table 8.21: Simulated spatial resolution (SR) at different source to collimator distances for In111 - 171 keV

| **Spatial resolution (mm)** | | | |
|---|---|---|---|
| **Distance (mm)** | **SR (a) mm** | **SR (b) mm** | **SR (c) mm** |
| 5 | 3,34 | 3,53 | 3,47 |
| 10 | 3,66 | 3,71 | 3,87 |
| 20 | 4,33 | 4,52 | 4,72 |
| 30 | 5,83 | 5,82 | 5,79 |

Table 8.22: Simulated sensitivity (S) at different source to collimator distances for In111 - 171 keV

| **Sensitivity (cps/MBq)** | | | |
|---|---|---|---|
| **Distance (mm)** | **S (a)** | **S (b)** | **S (c)** |
| 5 | 160,02 | 104,48 | 113,70 |
| 10 | 153,94 | 102,27 | 109,96 |
| 20 | 154,10 | 98,95 | 110,01 |
| 30 | 156,40 | 101,41 | 111,21 |

Table 8.23: Spatial resolution mean and standard deviation at different source to collimator distances of the simulated configurations for In111 - 171 keV

| **Distance (mm)** | $\mu$ | $\pm\sigma$ |
|---|---|---|
| 5 | 3,446 | 0,097 |
| 10 | 3,746 | 0,109 |
| 20 | 4,523 | 0,195 |
| 30 | 5,813 | 0,020 |

Table 8.24: Sensitivity percentage of optimized simulated collimators with respect to the reference one

| **Sensitivity percentage In111-171 keV** | | |
|---|---|---|
| **Distance (mm)** | **% (b)** | **% (c)** |
| 5 | 65,29 | 71,05 |
| 10 | 66,43 | 71,43 |
| 20 | 64,21 | 71,39 |
| 30 | 64,84 | 71,11 |

In Figure 8.23 the energy spectrum for Lu177 with energy of reference of 208 keV is reported.

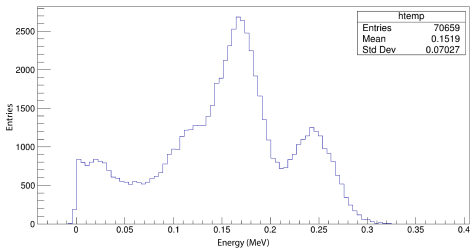


(a) SG 0.5 mm septa

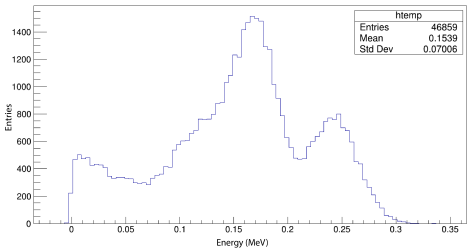


(b) NG 0.5 mm septa PLA

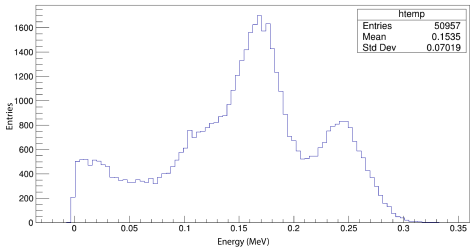


(c) NG 0.5 mm septa PA2200

Figure 8.23: Energy spectrum In111 - 171 keV. SG = Standard geometry and NG = Novel geometry concept

In Figure 8.24 and 8.25 the capillary source and the gaussian fit for In111 with energy of reference of 171 keV at 5 mm source to collimator distance are reported.

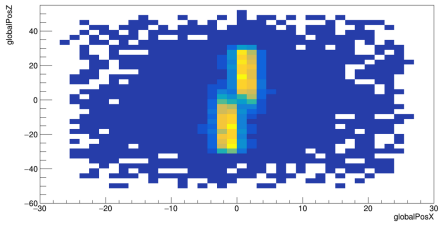


(a) SG 0.5 mm septa

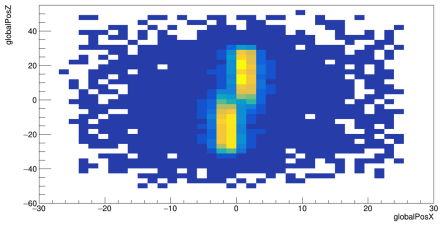


(b) NG 0.5 mm septa PLA

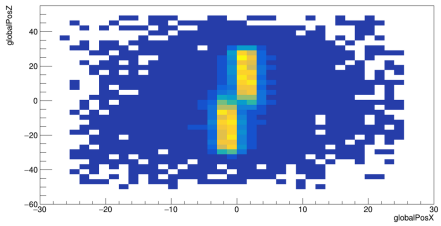


(c) NG 0.5 mm septa PA2200

Figure 8.24: Capillary radioactive source In111 - 171. SG = Standard geometry and NG = Novel geometry concept

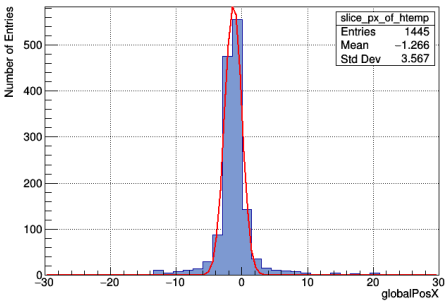


(a) SG 0.5 mm septa

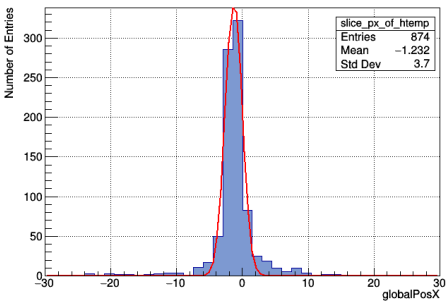


(b) NG 0.5 mm septa PLA

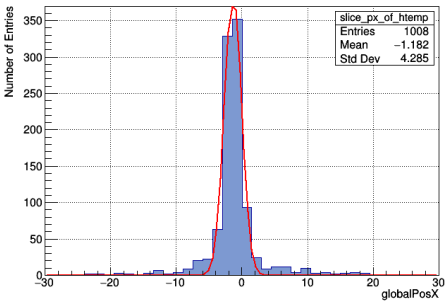


(c) NG 0.5 mm septa PA2200

Figure 8.25: Gaussian fit In111 - 171. SG = Standard geometry and NG = Novel geometry concept. The inset of each figure is referred to relative histogram

The sigma values obtained by fitting the histogram with the gaussian curve are

reported in the table 8.25. The values have been rounded at the second decimal place. These sigma values have been then used, as explained previously, to compute the spatial resolution multiplying it by 2,35.

Table 8.25: Gaussian Fit Sigma values at different source to collimator distances

| **Gaussian Fit Sigma for In111-171 keV** | | | |
|---|---|---|---|
| **Distance (mm)** | $\sigma$ **(a)** | $\sigma$ **(b)** | $\sigma$ **(c)** |
| 5 | 1,42 | 1,50 | 1,48 |
| 10 | 1,56 | 1,58 | 1,65 |
| 20 | 1,84 | 1,92 | 2,01 |
| 30 | 2,48 | 2,47 | 2,46 |

### In111 - 245 keV

In Figure 8.26 the spatial resolution for the three simulated configurations of the optimized collimator concept are reported using In111 as isotope. Instead in Figure 8.27 the sensitivity is reported.

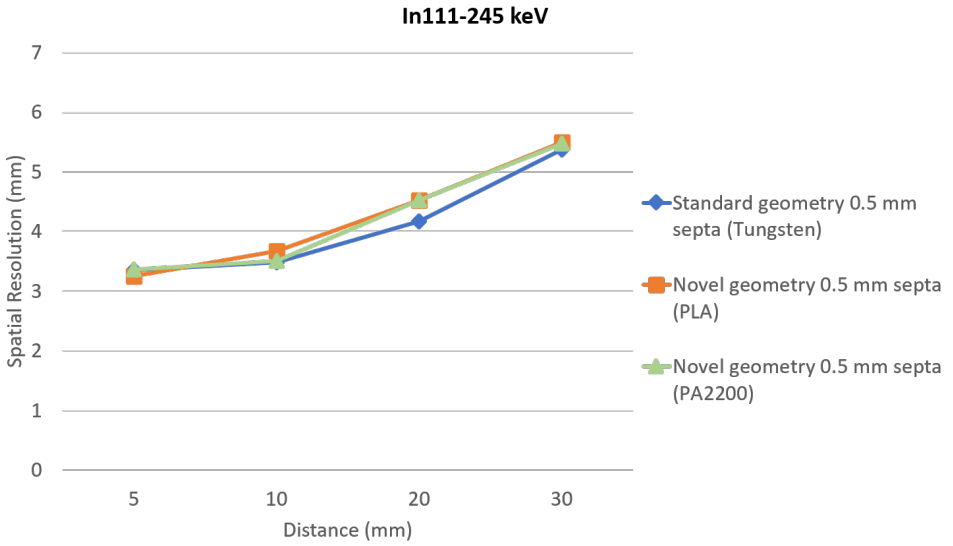


Figure 8.26: Spatial resolution as function of source to collimator distance

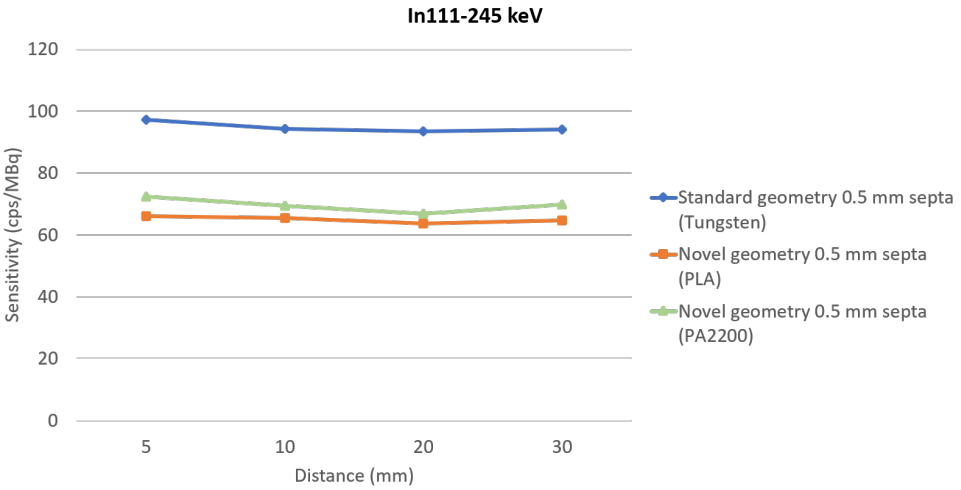


Figure 8.27: Sensitivity as function of source to collimator distance

In Table 8.26 the spatial resolution values are highlighted, while in Table 8.27 the sensitivity is reported. For the spatial resolution at 5 mm source to collimator distance we get a $\mu$ of 3,32 mm and a $\sigma$ of $\pm$0,06. The sensitivity showed by the

two novel concept collimator with the extruded plastic pixels is respectively almost ∼68% for the PLA concept and almost ∼74% for the PA2200 concept. In table **??** the sensitivity percentage at all the source to collimator distances are reported.

In Table 8.28 the other values of mean and standard deviation are reported.

Table 8.26: Simulated spatial resolution (SR) at different source to collimator distances for In111 - 245 keV

| **Spatial resolution (mm)** | | | |
|---|---|---|---|
| **Distance (mm)** | **SR (a) mm** | **SR (b) mm** | **SR (c) mm** |
| 5 | 3,35 | 3,25 | 3,36 |
| 10 | 3,49 | 3,67 | 3,51 |
| 20 | 4,17 | 4,53 | 4,52 |
| 30 | 5,38 | 5,50 | 5,47 |

Table 8.27: Simulated sensitivity (S) at different source to collimator distances for In111 - 245 keV

| **Sensitivity (cps/MBq)** | | | |
|---|---|---|---|
| **Distance (mm)** | **S (a)** | **S (b)** | **S (c)** |
| 5 | 97,19 | 65,98 | 72,29 |
| 10 | 94,22 | 65,55 | 69,33 |
| 20 | 93,44 | 63,65 | 66,95 |
| 30 | 94,02 | 64,64 | 69,88 |

Table 8.28: Spatial resolution mean and standard deviation at different source to collimator distances of the simulated configurations for In111 - 245 keV

| **Distance (mm)** | $\mu$ | $\pm\sigma$ |
|---|---|---|
| 5 | 3,32 | 0,06 |
| 10 | 3,55 | 0,09 |
| 20 | 4,40 | 0,20 |
| 30 | 5,45 | 0,06 |

Table 8.29: Sensitivity percentage of optimized simulated collimators with respect to the reference one

| **Sensitivity percentage In111-245 keV** | | |
|---|---|---|
| **Distance (mm)** | **% (b)** | **% (c)** |
| 5 | 67,89 | 74,38 |
| 10 | 69,57 | 73,58 |
| 20 | 68,12 | 71,65 |
| 30 | 68,75 | 74,32 |

In Figure 8.28, 8.29 and 8.30 the energy spectrum, capillary source and gaussian fitting using as energy of reference the 245 keV are reported.

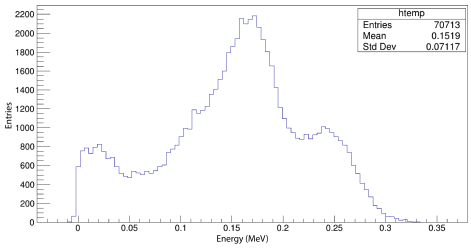


(a) SG 0.5 mm septa

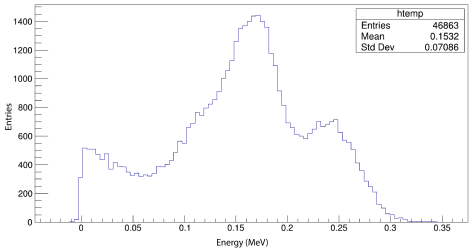


(b) NG 0.5 mm septa PLA

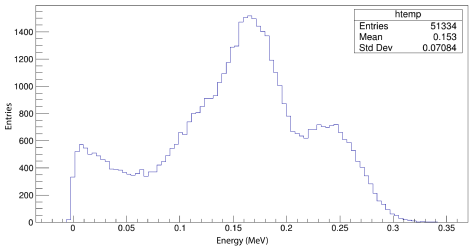


(c) NG 0.5 mm septa PA2200

Figure 8.28: Energy spectrum In111 - 245 keV. SG = Standard geometry and NG = Novel geometry concept

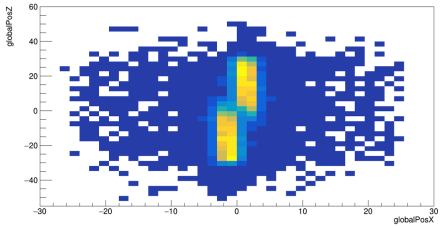


(a) SG 0.5 mm septa

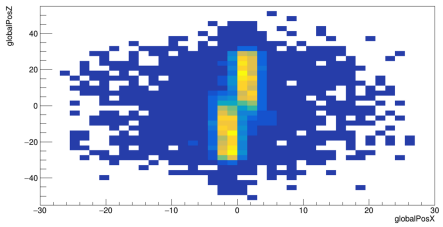


(b) NG 0.5 mm septa PLA

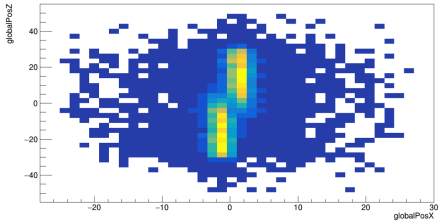


(c) NG 0.5 mm septa PA2200

Figure 8.29: Capillary radioactive source In111 - 245. SG = Standard geometry and NG = Novel geometry concept

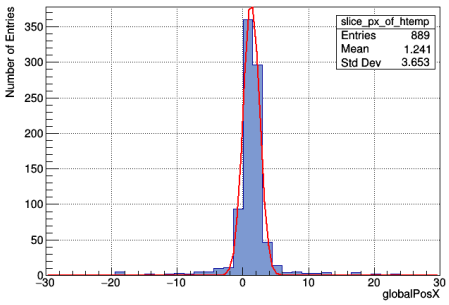


(a) SG 0.5 mm septa

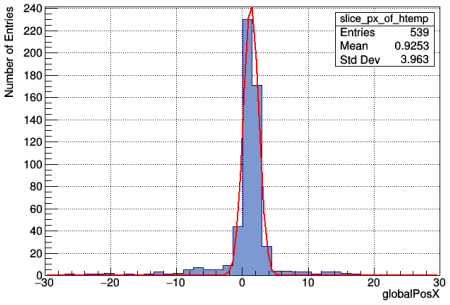


(b) NG 0.5 mm septa PLA

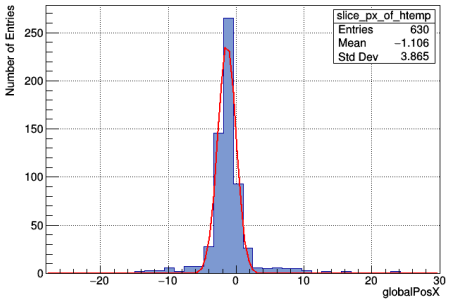


(c) NG 0.5 mm septa PA2200

Figure 8.30: Gaussian fit In111 - 245. SG = Standard geometry and NG = Novel geometry concept. The inset of each figure is referred to relative histogram

The sigma values obtained by fitting the histogram with the gaussian curve are reported in the table 8.30. The values have been rounded at the second decimal place. These sigma values have been then used, as explained previously, to compute the spatial resolution multiplying it by 2,35.

Table 8.30: Gaussian fitting sigma values at different source to collimator distances

| **Gaussian Fit Sigma for In111-245 keV** | | | |
|---|---|---|---|
| **Distance (mm)** | $\sigma$ **(a)** | $\sigma$ **(b)** | $\sigma$ **(c)** |
| 5 | 1,42 | 1,38 | 1,43 |
| 10 | 1,50 | 1,56 | 1,50 |
| 20 | 1,77 | 1,92 | 1,92 |
| 30 | 2,29 | 2,34 | 2,33 |

### 8.2.4 Ga67 isotope simulation

Finally we simulate the three novel concept collimator geometry also with Ga67 isotope. Ga67 has three major emission energy peak that are at 93, 184 and 293 keV with a probability of photons to be emitted respectively of almost ∼40%, ∼28% and ∼16%.

#### Ga67 - 93 keV

In Figure 8.31 and 8.32 the spatial resolution and sensitivity computed using the three novel collimator concept are reported.

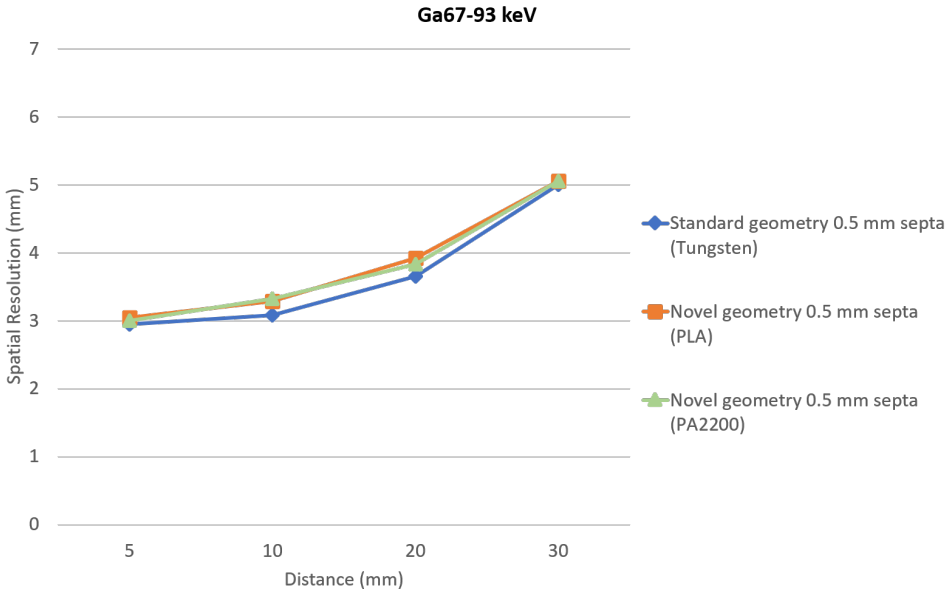


Figure 8.31: Spatial resolution as function of source to collimator distance

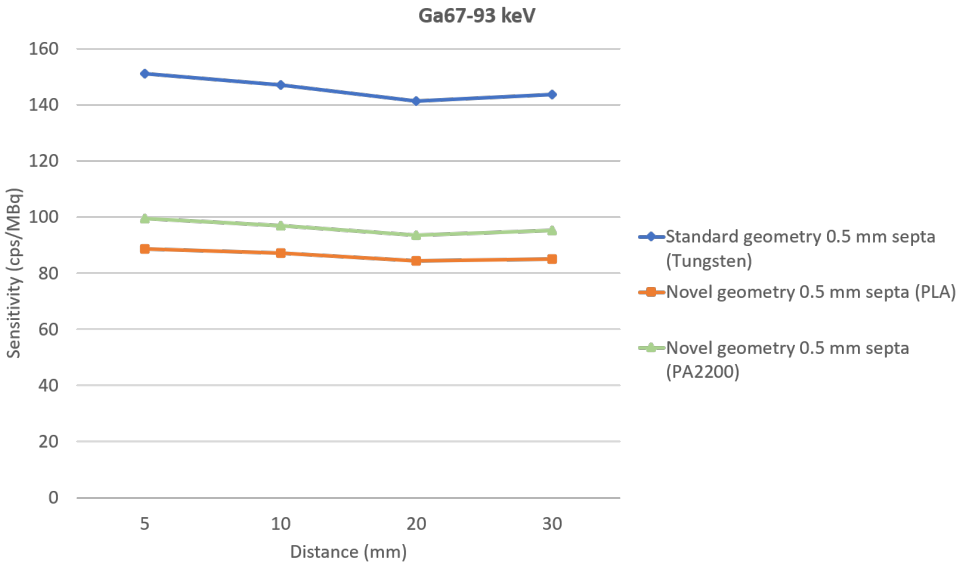


Figure 8.32: Sensitivity as function of source to collimator distance

In Table 8.31 the spatial resolution values are highlighted, while in Table 8.32 the sensitivity is reported. For the spatial resolution at 5 mm source to collimator distance we get a $\mu$ of 2,993 mm and a $\sigma$ of $\pm$0,050. The sensitivity showed by the two novel concept collimator with the extruded plastic pixels is respectively almost $\sim$58% for the PLA concept and almost $\sim$65% for the PA2200 concept. In table **??** the sensitivity percentage at all the source to collimator distances are reported.

In Table 8.33 the other values of mean and standard deviation are reported.

Table 8.31: Simulated spatial resolution (SR) at different source to collimator distances for Ga67 - 93 keV

| **Spatial resolution (mm)** | | | |
|---|---|---|---|
| **Distance (mm)** | **SR (a) mm** | **SR (b) mm** | **SR (c) mm** |
| 5 | 2,94 | 3,04 | 3,00 |
| 10 | 3,08 | 3,28 | 3,32 |
| 20 | 3,65 | 3,92 | 3,83 |
| 30 | 5,00 | 5,05 | 5,05 |

Table 8.32: Simulated sensitivity (S) at different source to collimator distances for Ga67 - 93 keV

| **Sensitivity (cps/MBq)** | | | |
|---|---|---|---|
| **Distance (mm)** | **S (a)** | **S (b)** | **S (c)** |
| 5 | 151,16 | 88,55 | 99,58 |
| 10 | 146,98 | 87,17 | 96,86 |
| 20 | 141,37 | 84,38 | 93,54 |
| 30 | 143,69 | 84,97 | 95,24 |

Table 8.33: Spatial resolution mean and standard deviation at different source to collimator distances of the simulated configurations for Ga67 - 93 keV

| **Distance (mm)** | $\mu$ | $\pm\sigma$ |
|---|---|---|
| 5 | 2,993 | 0,050 |
| 10 | 3,226 | 0,128 |
| 20 | 3,800 | 0,137 |
| 30 | 5,033 | 0,028 |

Table 8.34: Sensitivity percentage of optimized simulated collimators with respect to the reference one

| **Sensitivity percentage Ga67-93 keV** | | |
|---|---|---|
| **Distance (mm)** | **% (b)** | **% (c)** |
| 5 | 58,58 | 65,88 |
| 10 | 59,31 | 65,90 |
| 20 | 59,69 | 66,17 |
| 30 | 59,13 | 66,28 |

In Figure 8.33 and 8.34 and 8.35 the energy spectrum, capillary source and gaussian fit of Ga67 with energy of reference set at 93 keV are reported.

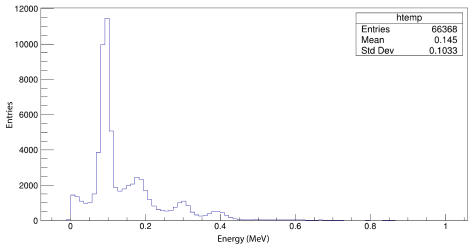


(a) SG 0.5 mm septa

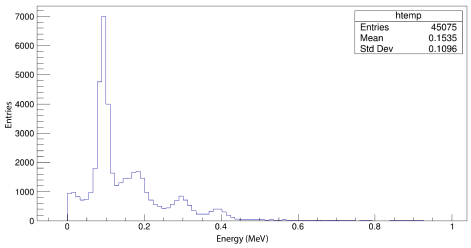


(b) NG 0.5 mm septa PLA

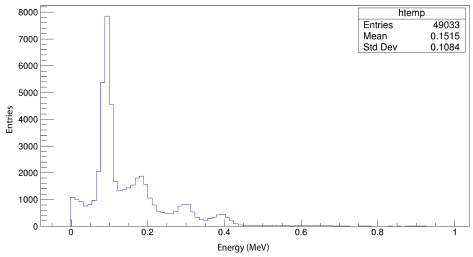


(c) NG 0.5 mm septa PA2200

Figure 8.33: Energy spectrum Ga67 - 93 keV. SG = Standard geometry and NG = Novel geometry concept

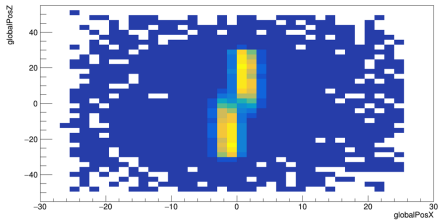


(a) SG 0.5 mm septa

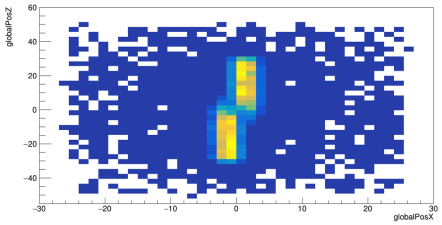


(b) NG 0.5 mm septa PLA

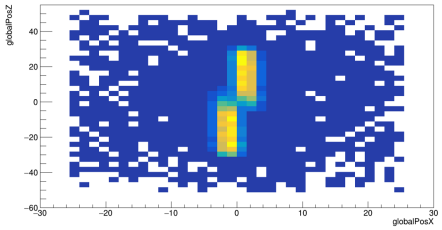


(c) NG 0.5 mm septa PA2200

Figure 8.34: Capillary radioactive source Ga67 - 93 keV. SG = Standard geometry and NG = Novel geometry concept

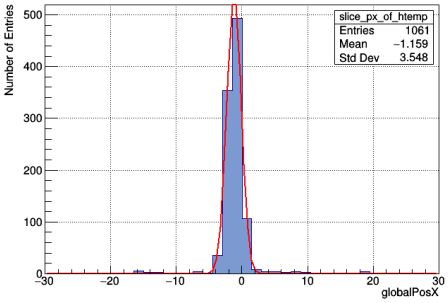


(a) SG 0.5 mm septa

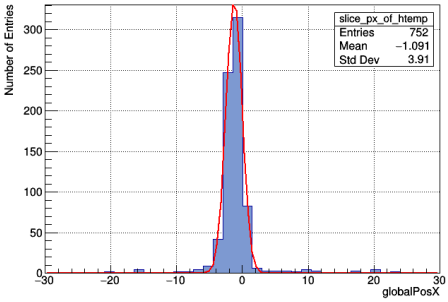


(b) NG 0.5 mm septa PLA

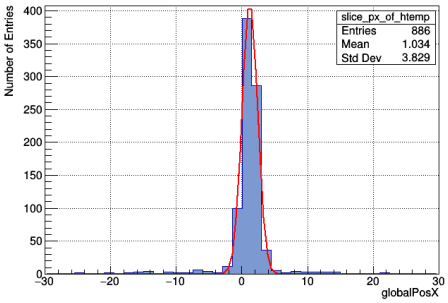


(c) NG 0.5 mm septa PA2200

Figure 8.35: Gaussian fit Ga67 - 93 keV. SG = Standard geometry and NG = Novel geometry concept. The inset of each figure is referred to relative histogram

The sigma values obtained by fitting the histogram with the gaussian curve are reported in the table 8.35. The values have been rounded at the second decimal place. These sigma values have been then used, as explained previously, to compute the spatial resolution multiplying it by 2,35.

Table 8.35: Gaussian fitting sigma values at different source to collimator distances

| **Gaussian Fit Sigma for Ga67-184 keV** | | | |
|---|---|---|---|
| **Distance (mm)** | $\sigma$ **(a)** | $\sigma$ **(b)** | $\sigma$ **(c)** |
| 5 | 1,25 | 1,30 | 1,28 |
| 10 | 1,31 | 1,40 | 1,41 |
| 20 | 1,55 | 1,67 | 1,63 |
| 30 | 2,13 | 2,15 | 2,15 |

### Ga67 - 184 keV

In Figure 8.36 and 8.37 the spatial resolution and sensitivity computed using the three novel collimator concept are reported.

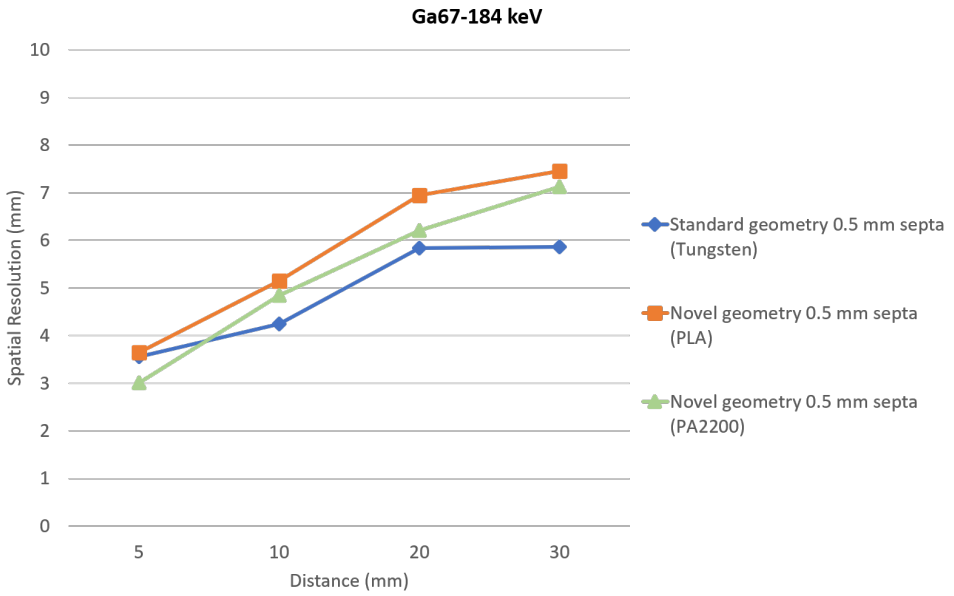


Figure 8.36: Spatial resolution as function of source to collimator distance

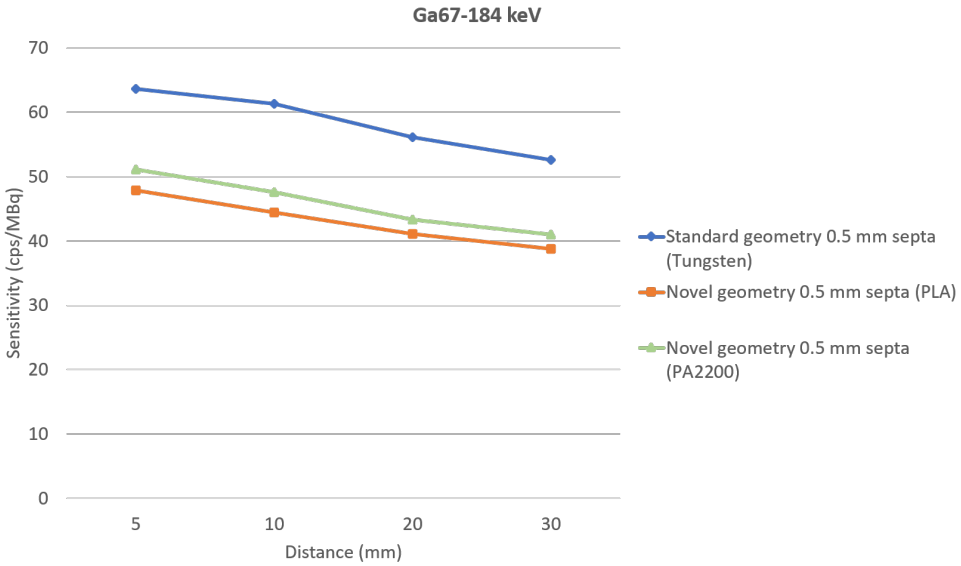


Figure 8.37: Sensitivity as function of source to collimator distance

In Table 8.36 the spatial resolution values are highlighted, while in Table 8.37 the sensitivity is reported. For the spatial resolution at 5 mm source to collimator distance we get a $\mu$ of 3,403 mm and a $\sigma$ of $\pm$0,349. The sensitivity showed by the two novel concept collimator with the extruded plastic pixels is respectively almost $\sim$75% for the PLA concept and almost $\sim$80% for the PA2200 concept. In table **??** the sensitivity percentage at all the source to collimator distances are reported.

In Table 8.38 the other values of mean and standard deviation are reported.

Table 8.36: Simulated spatial resolution (SR) at different source to collimator distances for Ga67 - 93 keV

| **Spatial resolution (mm)** | | | |
|---|---|---|---|
| **Distance (mm)** | **SR (a) mm** | **SR (b) mm** | **SR (c) mm** |
| 5 | 3,56 | 3,64 | 3,01 |
| 10 | 4,25 | 5,15 | 4,84 |
| 20 | 5,84 | 6,95 | 6,21 |
| 30 | 5,86 | 7,46 | 7,13 |

Table 8.37: Simulated sensitivity (S) at different source to collimator distances for Ga67 - 184 keV

| **Sensitivity (cps/MBq)** | | | |
|---|---|---|---|
| **Distance (mm)** | **S (a)** | **S (b)** | **S (c)** |
| 5 | 63,66 | 47,89 | 51,15 |
| 10 | 61,33 | 44,40 | 47,64 |
| 20 | 56,16 | 41,09 | 43,35 |
| 30 | 52,60 | 38,82 | 40,98 |

Table 8.38: Spatial resolution mean and standard deviation at different source to collimator distances of the simulated configurations for Ga67 - 184 keV

| **Distance (mm)** | $\mu$ | $\pm\sigma$ |
|---|---|---|
| 5 | 3,403 | 0,342 |
| 10 | 4,746 | 0,457 |
| 20 | 6,333 | 0,565 |
| 30 | 6,816 | 0,844 |

Table 8.39: Sensitivity percentage of optimized simulated collimators with respect to the reference one

| **Sensitivity percentage Ga67-184 keV** | | |
|---|---|---|
| **Distance (mm)** | **% (b)** | **% (c)** |
| 5 | 75,23 | 80,35 |
| 10 | 72,40 | 77,68 |
| 20 | 73,17 | 77,19 |
| 30 | 73,80 | 77,91 |

In Figure 8.38 and 8.39 and 8.40 the energy spectrum, capillary source and gaussian fit of Ga67 with energy of reference set at 184 keV are reported.

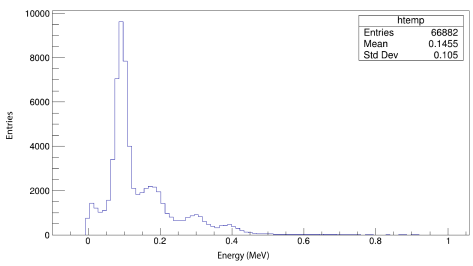


(a) SG 0.5 mm septa

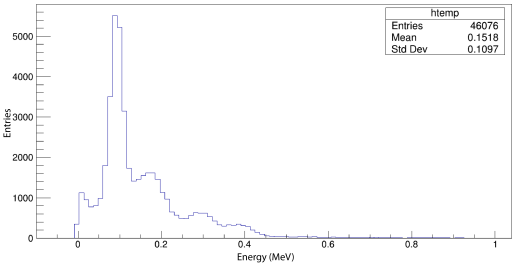


(b) NG 0.5 mm septa PLA

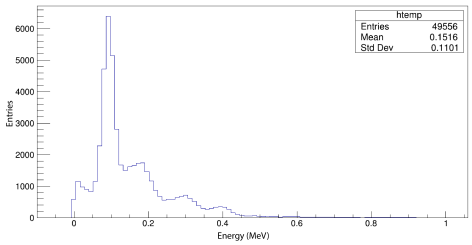


(c) NG 0.5 mm septa PA2200

Figure 8.38: Energy spectrum Ga67 - 184 keV. SG = Standard geometry and NG = Novel geometry concept

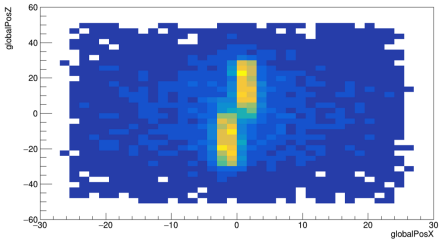


(a) SG 0.5 mm septa

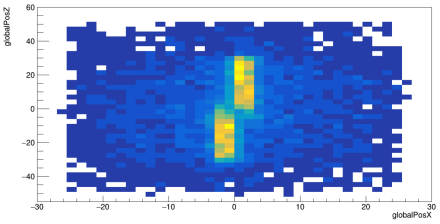


(b) NG 0.5 mm septa PLA

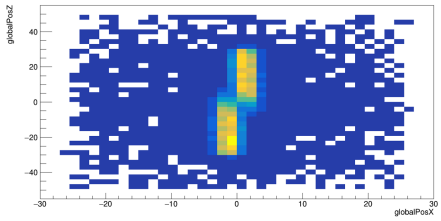


(c) NG 0.5 mm septa PA2200

Figure 8.39: Capillary radioactive source Ga67 - 184 keV. SG = Standard geometry and NG = Novel geometry concept

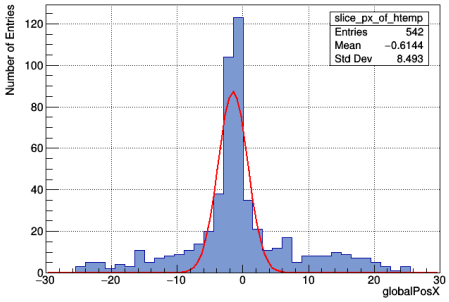


(a) SG 0.5 mm septa

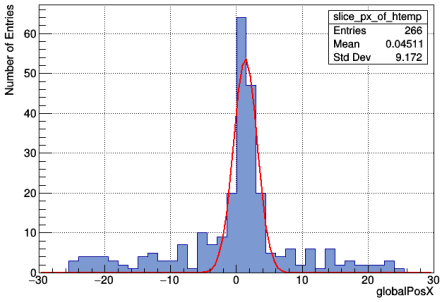


(b) NG 0.5 mm septa PLA

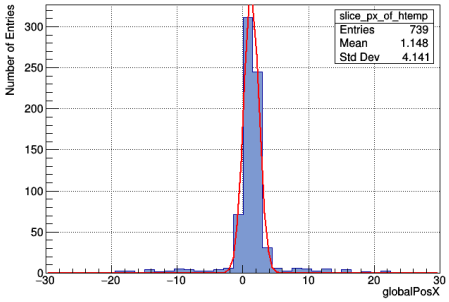


(c) NG 0.5 mm septa PA2200

Figure 8.40: Gaussian fit Ga67 - 184 keV. SG = Standard geometry and NG = Novel geometry concept. The inset of each figure is referred to relative histogram

The sigma values obtained by fitting the histogram with the gaussian curve are reported in the table 8.40. The values have been rounded at the second decimal place. These sigma values have been then used, as explained previously, to compute the spatial resolution multiplying it by 2,35.

Table 8.40: Gaussian fitting sigma values at different source to collimator distances

| **Gaussian Fit Sigma for Ga67-184 keV** | | | |
|---|---|---|---|
| **Distance (mm)** | $\sigma$ **(a)** | $\sigma$ **(b)** | $\sigma$ **(c)** |
| 5 | 1,51 | 1,55 | 1,28 |
| 10 | 1,81 | 2,20 | 2,06 |
| 20 | 2,49 | 2,96 | 2,64 |
| 30 | 2,50 | 3,17 | 3,03 |

### Ga67 - 293 keV

In Figure 8.41 and 8.42 the spatial resolution and sensitivity computed using the three novel collimator concept are reported.

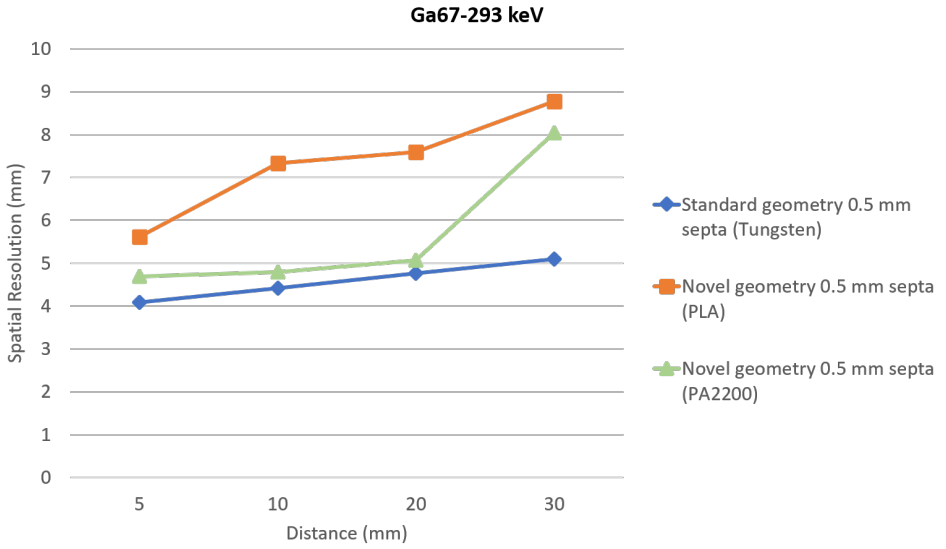


Figure 8.41: Spatial resolution as function of source to collimator distance

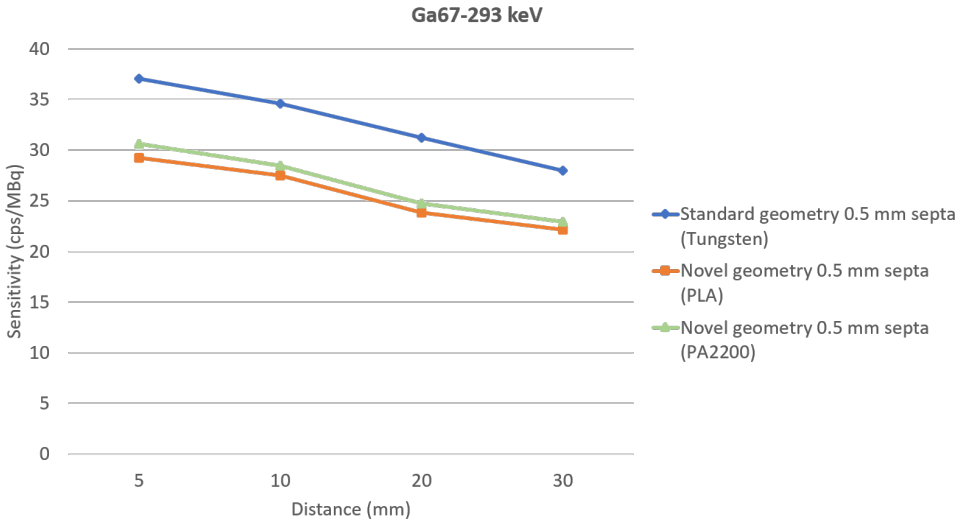


Figure 8.42: Sensitivity as function of source to collimator distance

In Table 8.41 the spatial resolution values are highlighted, while in Table 8.42 the sensitivity is reported. For the spatial resolution at 5 mm source to collimator distance we get a $\mu$ of 4,793 mm and a $\sigma$ of $\pm$0,770. The sensitivity showed by the two novel concept collimator with the extruded plastic pixels is respectively almost

∼78% for the PLA concept and almost ∼82% for the PA2200 concept. In table 8.44 the sensitivity percentage at all the source to collimator distances are reported. In Table 8.43 the other values of mean and standard deviation are reported.

Table 8.41: Simulated spatial resolution (SR) at different source to collimator distances for Ga67 - 293 keV

| **Spatial resolution (mm)** | | | |
|---|---|---|---|
| **Distance (mm)** | **SR (a) mm** | **SR (b) mm** | **SR (c) mm** |
| 5 | 4,08 | 5,61 | 4,69 |
| 10 | 4,42 | 7,33 | 4,80 |
| 20 | 4,77 | 7,60 | 5,07 |
| 30 | 5,09 | 8,78 | 8,04 |

Table 8.42: Simulated sensitivity (S) at different source to collimator distances for Ga67 - 293 keV

| **Sensitivity (cps/MBq)** | | | |
|---|---|---|---|
| **Distance (mm)** | **S (a)** | **S (b)** | **S (c)** |
| 5 | 37,07 | 29,24 | 30,63 |
| 10 | 34,58 | 27,48 | 28,44 |
| 20 | 31,25 | 23,86 | 24,72 |
| 30 | 27,99 | 22,12 | 22,93 |

Table 8.43: Spatial resolution mean and standard deviation at different source to collimator distances of the simulated configurations for Ga67 - 293 keV

| **Distance (mm)** | $\mu$ | $\pm\sigma$ |
|---|---|---|
| 5 | 4,793 | 0,770 |
| 10 | 5,516 | 1,581 |
| 20 | 5,813 | 1,554 |
| 30 | 7,303 | 1,952 |

Table 8.44: Sensitivity percentage of optimized simulated collimators with respect to the reference one

| **Sensitivity percentage Ga67-293 keV** | | |
|---|---|---|
| **Distance (mm)** | **% (b)** | **% (c)** |
| 5 | 78,88 | 82,63 |
| 10 | 79,47 | 82,24 |
| 20 | 76,35 | 79,10 |
| 30 | 79,03 | 81,92 |

In Figure 8.43 and 8.44 and 8.45 the energy spectrum, capillary source and gaussian fit of Ga67 with energy of reference set at 293 keV are reported.

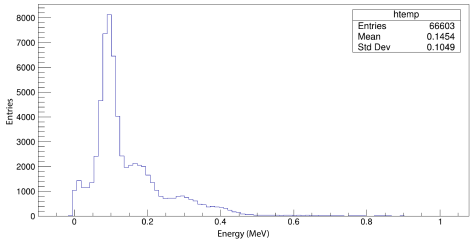


(a) SG 0.5 mm septa

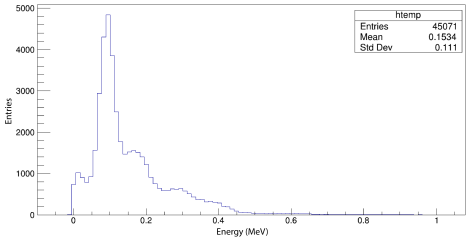


(b) NG 0.5 mm septa PLA

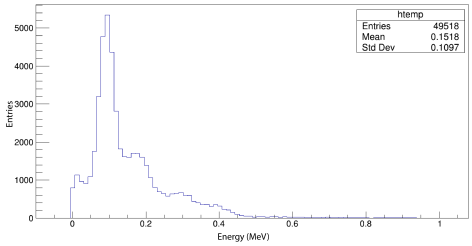


(c) NG 0.5 mm septa PA2200

Figure 8.43: Energy spectrum Ga67 - 293 keV. SG = Standard geometry and NG = Novel geometry concept

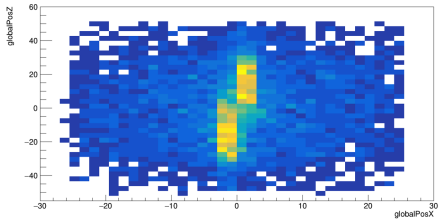


(a) SG 0.5 mm septa

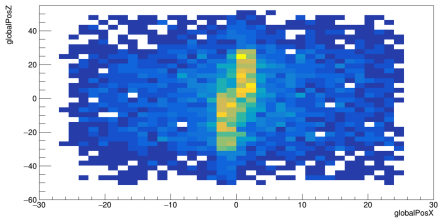


(b) NG 0.5 mm septa PLA

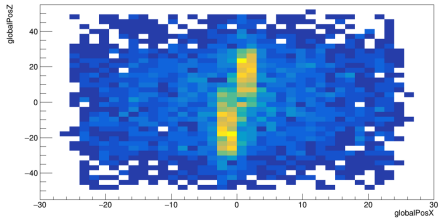


(c) NG 0.5 mm septa PA2200

Figure 8.44: Capillary radioactive source Ga67 - 293 keV. SG = Standard geometry and NG = Novel geometry concept

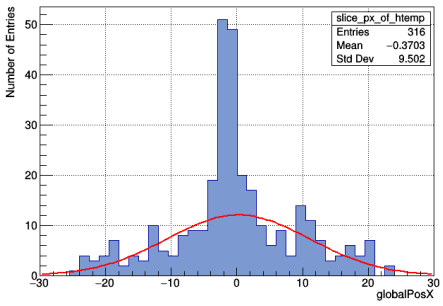


(a) SG 0.5 mm septa

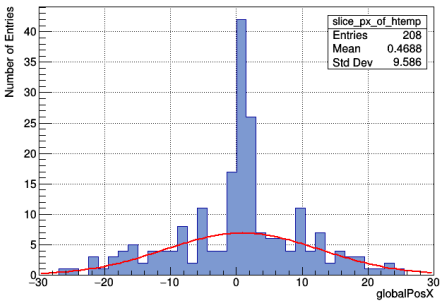


(b) NG 0.5 mm septa PLA

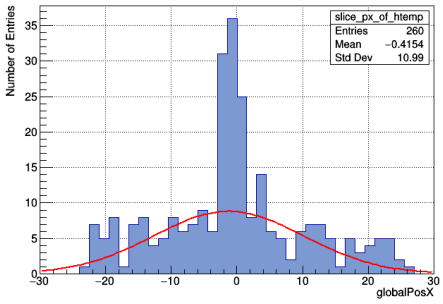


(c) NG 0.5 mm septa PA2200

Figure 8.45: Gaussian fit Ga67 - 293 keV. SG = Standard geometry and NG = Novel geometry concept. The inset of each figure is referred to relative histogram

The sigma values obtained by fitting the histogram with the gaussian curve are reported in the table 8.45. The values have been rounded at the second decimal place. These sigma values have been then used, as explained previously, to compute the spatial resolution multiplying it by 2,35.

Table 8.45: Gaussian fitting sigma values at different source to collimator distances

| **Gaussian Fit Sigma for Ga67-293 keV** | | | |
|---|---|---|---|
| **Distance (mm)** | **$\sigma$ (a)** | **$\sigma$ (b)** | **$\sigma$ (c)** |
| 5 | 1,73 | 2,38 | 1,99 |
| 10 | 1,90 | 3,12 | 2,04 |
| 20 | 2,03 | 3,23 | 2,15 |
| 30 | 2,16 | 3,73 | 3,42 |

As for Lu177 where we had energy peaks with low emission percentage, also here with Ga67 we get for the energy of reference of 184 keV and 293 keV low emission percentage. The effect of this low photons emission is highlighted clearly looking at the sensitivity we get for the three energy peaks. Moreover, considering the last two peaks. The inability to properly fit with a gaussian curve the line profile of the capillary source (Figure 8.45) results consequently in a bad spatial resolution, specially for the 283 keV energy of reference.

# Chapter 9

# Experimental validation

The first novel collimator concept and optimized geometry have been sent to BioEmission Technology Solutions in order to experimentally validate them. The first collimators concept (1.5x1.5x45 mm and 0.4 mm septa thickness) have been evaluated using both a vial and a capillary source placed at direct contact with the front face of the collimators. Three different isotopes have been used to observe the efficiency of the 3D printed collimators that are respectively $^{99}$Tc, In111 and Ga67.
The vial was filled with 19uCi - 200ul once of $^{99}$Tc, In111 and Ga67 and two minutes acquisition was done. The experimental set-up can be seen in Figure 9.1 and in Figure 9.2 the block scheme of the experimental set-up is reported.

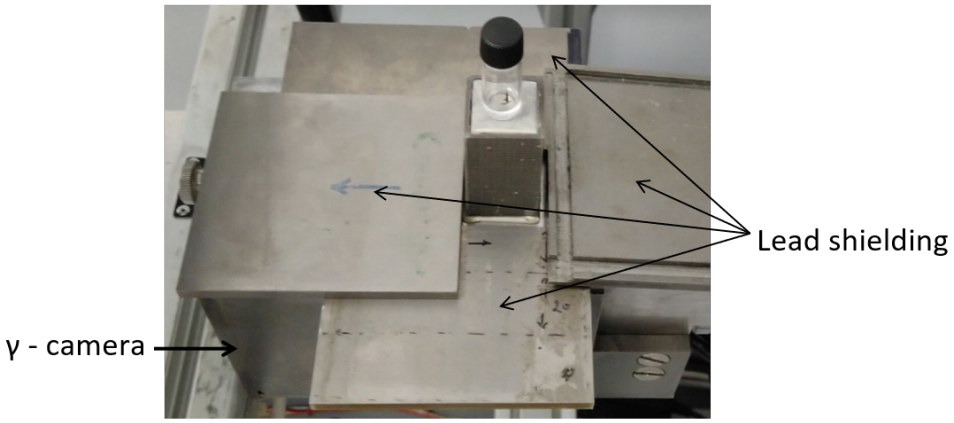


Figure 9.1: Experimental set-up with vial

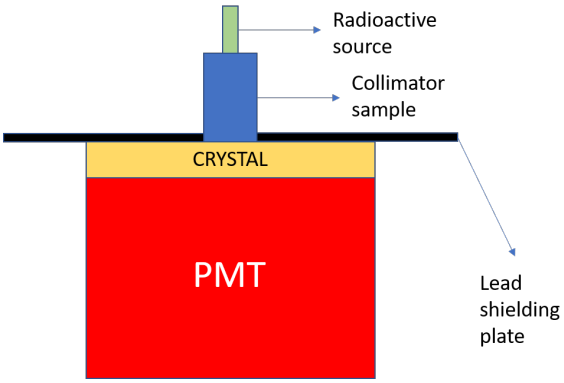


Figure 9.2: Block scheme of experimental set-up

With the first PLA and PA2200 first collimator concept, a third collimator 3D printed with the standard geometry and using a radiopaque PLA (Figure 9.3) was sent to BIOEMTECH[1]. As we will see, the radiopaque PLA, even if certified to block the X-ray radiation, was not good for the gamma rays. For this reason, since it allows pass practically all the incoming photons without being able to block them, it was considered as the reference in terms of number of recorded photons to which compare the other two samples. In Figure 9.4, 9.5 and 9.6 the vial as imaged by the $\gamma$-eye$^{TM}$ system with the additive manufactured collimators using the different radioisotopes is shown. In Table 9.1 the total counts with the vial as source are reported.

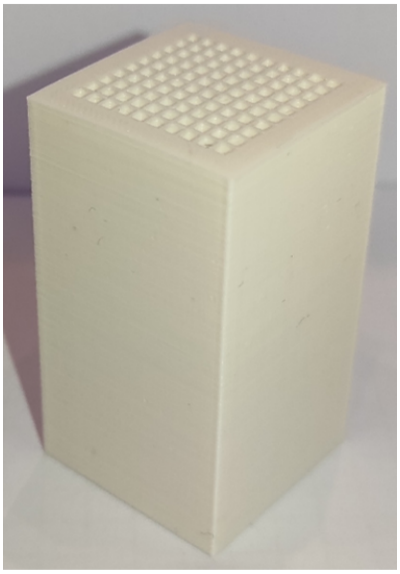

Figure 9.3: Reference collimator 3D printed with radiopaque PLA

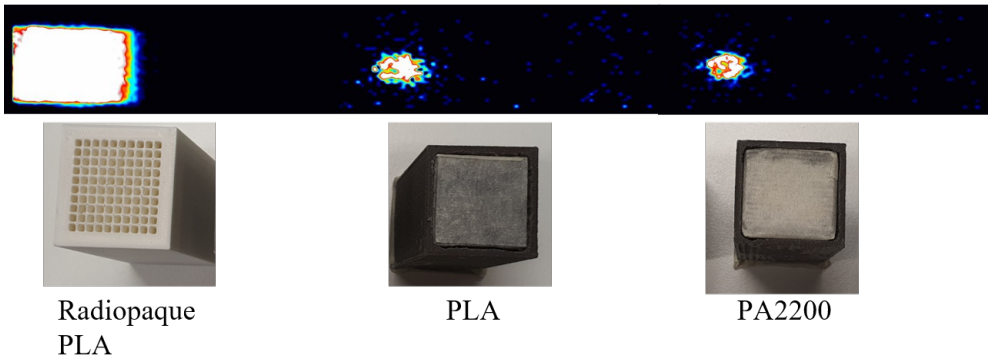


Figure 9.4: Tc99 vial

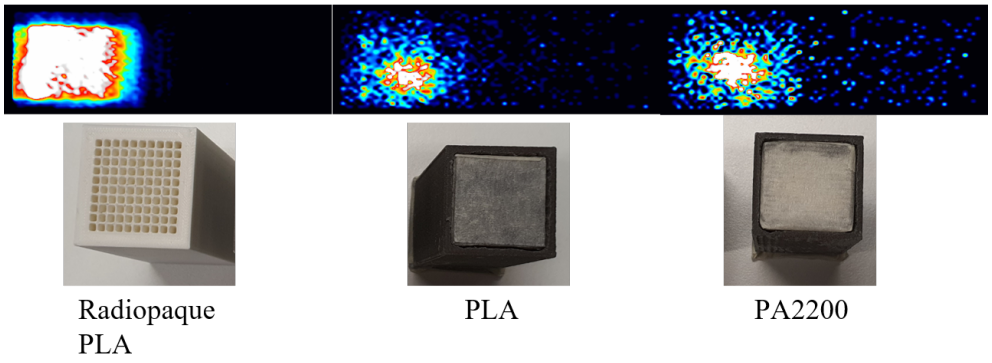


Figure 9.5: In111 vial

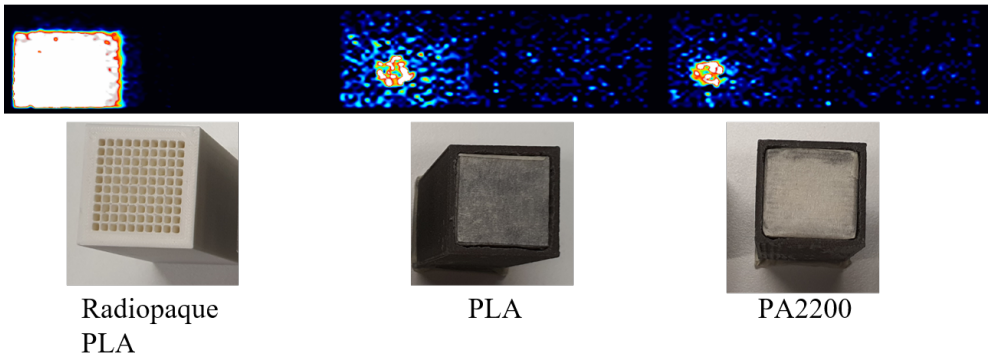


Figure 9.6: Ga67 vial

Table 9.1: Entries counts with vial source

| Total Count | | | |
|---|---|---|---|
| **Collimator** | **Tc99** | **In111** | **Ga67** |
| Radiopaque PLA | 8*$10^9$ | 9*$10^9$ | 2850000 |
| PLA | 17000 | 49000 | 39000 |
| PA2200 | 13000 | 44000 | 26000 |

In Figure 9.7 the experimental set-up for imaging the capillary source is reported, while in Figure 9.8, 9.9 and 9.10 instead the capillary source as imaged by the imaging device are presented. The capillary was filled $^{99}$Tc, In111 and Ga67 with (5uCi - 30ul) and the the source was acquired for ten minutes.

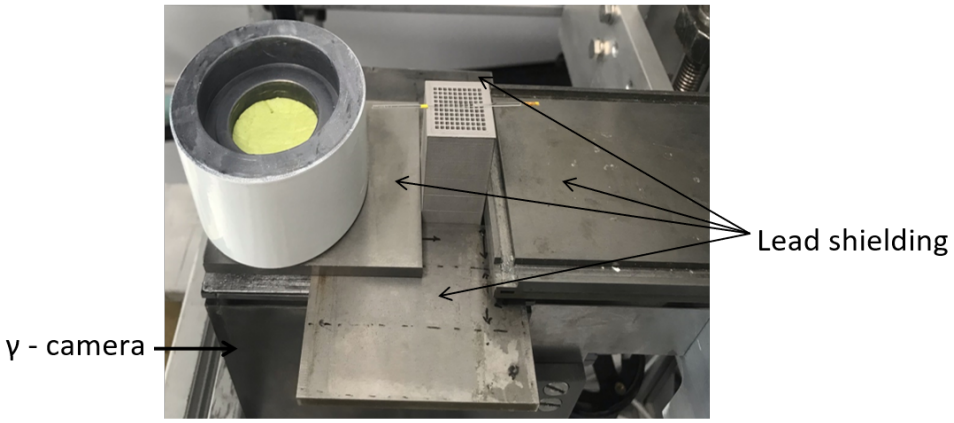


Figure 9.7: experimental set-up for capillary source acquisition

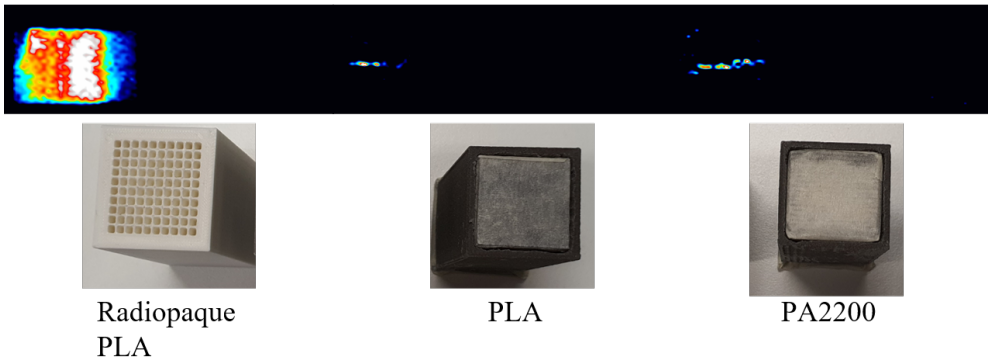


Figure 9.8: Tc99 vial

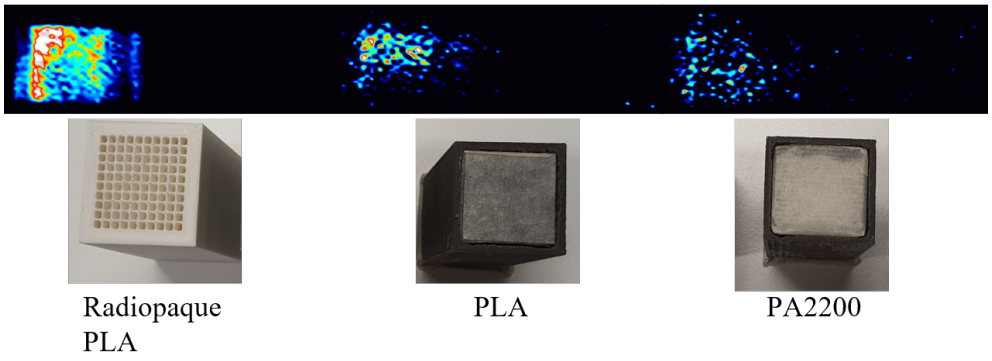


Figure 9.9: In111 vial

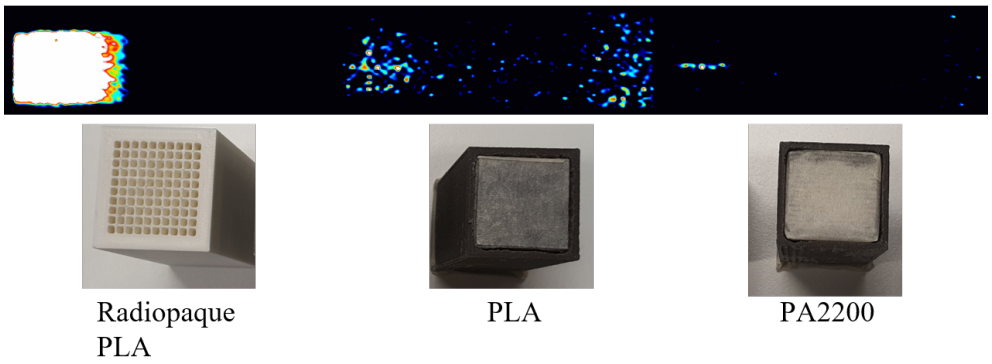


Figure 9.10: Ga67 vial

The experimental tests conducted on the the first collimator concept additively manufactured, demonstrated that using a low energy isotope, such as $^{99}$Tc, both the vial and the capillary source are well imaged. Instead, using higher energy isotopes such as Ga67 and In111, the sample are no more able to provide good performance in terms of spatial resolution mainly. This is also due to the fact that these collimator samples suffer for the lacking of tungsten powder. Indeed, as already highlighted we were unable to provide the effective filling with the metal powder, and this problem is highlighted specially with higher energy isotopes. The reference collimator 3D printed using the radiopaque PLA instead resulted completely transparent to the gamma rays impacting on the detector.

# Chapter 10

# Discussion and conclusion

A novel concept collimator fabricated using the additive manufacturing processes, nowadays easily accessible to everyone, has been presented. The most accessible and low cost 3D printing technologies are the FDM and the SLS processes. For sure, the FDM process results to be the most used printing technology with more then 60% of the market. But, as highlighted in this work, different FDM printers exist ranging from cheap devices (as the Ender 5 Plus that we used) up to industrial machine or more expensive one like the Original Prusa mod. I3 MK3S+ used by M.A.D.E Concept to fabricate some of the proposed collimator samples.
All the investigated additive manufacturing technologies have been demonstrated to be reliable processes for the fabrication of a collimator for small-animal imaging devices. **In particular, the proposed innovative idea of fabricating a collimator on the base of the "negative structure" concept to maximize the efficiency of the printing process and the ease of the production process itself**, specially the process of those printing devices that have not good accuracy or precision, resulted to be highly effective. The collimators, first concept and optimized concept, have been evaluated using a CT system in order to evaluate the geometric differences between the printed part and CAD model. The CT scansion has been done also in order to investigate the dispersion of the tungsten powder between the extruded holes of the collimator. The CT investigation permitted also to validate, even if only partially, the goodness of the proposed idea. Indeed, the extruded plastic pixels resulted transparent to the X-ray radiation (much lower in energy with respect to gamma radiation).
The new proposed geometry have been then **simulated in their function environment by numerical simulations performed in GATE, to assess the value of sensitivity and spatial resolution and their differences with respect to the standard collimators at different source to collimator distances**. Different simulations have been done both for the first collimator concept, with hole 1.5x1.5 mm and 45 mm in length and spaced by 0.4 mm septa, and for the optimized concept, with hole of 2x2mm and 30 mm in length and spaced by 0.5 mm septa. What emerges from the simulation of both the proposed concept is that **the spatial resolution is not greatly or at all affected by the material (PLA and PA2200) used for the extruded holes, while the sensitivity results to be affected by the material**. Indeed, what we saw for every simulations done, not only with $^{99}$Tc, but also with higher energy isotopes like **Lu177, In111 and Ga67 is that the sensitivity of the system tends to decrease and settle on a value between ∼40-80% of**

**the sensitivity of the reference collimator simulated**. This limitation was considered and awaited in the thinking of the novel 3D printed geometry, since the plastic material used in the additive manufacturing processes have, as already said, higher density than the air that usually fills the holes of a standard collimator. Considering the optimized geometry with which higher isotopes have been simulated, what we saw is that we start getting bad spatial resolution and sensitivity values with Ga67 higher energy peaks. The performance of the collimator decreases producing bad resolution and sensitivity. This is due mainly to the fact that the higher energy peaks of Ga67 show low photons emission percentage and the plastic material of the holes tends to reduce even more the counted photons. Furthermore, with Ga67 resulted difficult to achieve a good fitting with the gaussian curve of the line profiles of the capillary source. Effect this that contribute to the worsening of the computation of the spatial resolution. Considering the optimized geometry **we simulated, for $^{99}$Tc isotope, also the 3D reconstructed model obtained using the imaging system onboard of the 3D printer**. The imaging system used to reconstruct the 3D model of the 3D printed collimator, in this workflow has been used only for the reconstruction of the model itself, withouth performing geometric measurements on the printed part. The reconstructed model has been then imported in GATE software in order to be simulated and observe the issues produced by the printing process errors on the parallelism and not linearity of the extruded holes. The results of the simulation were really interesting because they highlight the effects of the printing error on the spatial resolution and sensitivity of the system. Indeed, the presence of non parallelism between the extruded holes, holes with section bigger than the one defined in CAD and defects such as the fusion of multiple holes together, play a really important role in the definition of the performance of the imaging system. Effects this that we are not able to simulate directly in GATE with the traditional geometry definition.
Furthermore, an **experimental data** obtained, with $^{99}$Tc source, using a $\gamma$-eye$^{\text{TM}}$ system, gave a value in terms of spatial resolution and sensitivity that **confirmed the validity of the simulation done**. The experimental data refers to a commercial tungsten collimator, mounted on a $\gamma$-eye$^{\text{TM}}$ system, with the optimized geometry (hole dimension, length and septa thickness equal to the one simulated in GATE) with the only exception for the hole shape that was hexagonal instead of square. **The measured spatial resolution at 10 mm source to collimator distance was 4 mm, while the sensitivity 90 cps/MBq with an energy window of $\pm$20%**. The higher sensitivity we experienced is dependent not only on the shape of the hole, that being square guarantee a bigger area trough which the photons can pass but also on the type of activity used for the experimental as well as the acquisition time they used for the test itself. However, this experimental data confirm the goodness of the simulations and make us believe that this kind of approach could be easily applicable with benefits, in pre-clinical small animal imaging devices.
**The novel geometries proposed in this work**, both the first and the optimized one, **have demonstrated, numerically, and experimentally to properly have good measurement performance and being able to provide values of spatial resolution comparable to the one provided by the standard geometries** nowadays used. The sensitivity, from the numerical point of view, as expected, results affected by the plastic material of the extruded holes. We experienced a sensitivity percentage difference of the proposed simulated novel concept collimators with respect to the reference one. Difference this, due to the effect of the plastic extruded holes that tend to absorb a percentage of the incoming photons, causing a decrease in photons collection. But, even if the sensitivity results affected by the material of the

extruded holes, the novelty in the fabrication of this kind of imaging system brings clear advantages in terms of costs and customization.
The customization could be the key-point for overcoming the sensitivity reduction; the printing parameters could be set to reduce the overall density of the extruded pixels enhancing the local transparency to the $\gamma$-rays. From the costs point of view,**the total cost of a complete collimator with the dimension of the one actually used on-board of the $\gamma$-eye$^{\mathbf{TM}}$** and printed in SLS technology, results to be less than 300 euro, plus the cost of the tungsten powder that will be around 100 euro for 500 g of metal powder. Considering the actual cost of such a collimator ($\sim$7000 euro) this solution could be easily implementable and achievable by all those small and medium research groups, and also start-up or small companies, that can, easily and at low cost, fabricate their own nuclear medicine collimator. Furthermore, this new and innovative approach to the production problem of collimators, can stimulate the scientific research on this field, leading to the production, by means of the additive manufacturing processes, of collimation systems with always novel features and innovative geometries or production techniques, improving day by day the efficiency and reliability of the product itself.
Further implementations will regard the filling procedure that it is found to be the weakest point of the fabrication chain and other implementation will focus on the possibility to reduce the printing filling of the extruded holes, going in this way to increase the efficiency in recording the incoming photons.
Even if further implementations are needed to achieve the maximum results from the experimental point of view, specially for what concern the filling procedure, and not all the possible solutions have been explored due to time lacking, the solution we proposed pave the way to enormous future development in this research and application field.
Despite the qualitative experimental results a proof of concept has been demonstrated related to the possibility of using cost effective technologies for producing affordable and reliable collimators. The numerical promising results have been followed by very promising experimental observation. Unfortunately the pandemic has stopped the experimental part of the work which paves the way for future engineered collimators. Anyway, the imaging system has shown to have a huge potentiality in helping to understand how the printing errors could affect the measurement characteristics of a collimator.
The workflow of the thesis, that includes both the 3D printer set up, the simulation set up and the experimental set up, represents an important starting point for future studies. Starting from this research, it could be possible to implement and upgrade the production method with advanced features and allow researchers to explore and test and validate complex and always more innovative and, I will suggest, futuristic collimation systems and also detectors. The approach proposed in this work intend to give the researchers a way of producing something, today complex and not so easy to fabricate, in a more ease way and with production methodology that doesn't require complex knowledge or specific tools. The presented work implements a method that allow to dynamically evaluate the efficiency of a collimation systems as well of the imaging system itself. Further development will regard the possibility to integrate a feedback control able to detect, by means of th imaging system and dedicated algorithms, when we achieved a deviation in the printed geometry big enough to drastically decrease the imaging performance of the collimator, making it useless for the purpose it would be made and try to correct it going to modify the printing parameters or stop the printing process in order to avoid waste of material.

# Bibliography


[1] Bioemtech. https://bioemtech.com.

[2] Mehslab. www.meshlab.net.

[3] Opencv distance transform. https://docs.opencv.org/4.x/d2/dbd/tutorial-distance-transform.html.

[4] Opencv otsu thresholding. https://docs.opencv.org/3.4/d7/d4d/tutorial-py-thresholding.html.

[5] Opencv template matching. https://docs.opencv.org/3.4/de/da9/tutorial-template-matching.html.

[6] Prosilas. www.prosilas.com.

[7] Scikitimage marching cubes. https://scikit-image.org/docs/dev/auto-examples/edges/plot-marching-cubes.html.

[8] Karen Van Audenhaege, Roel Van Holen, Stefaan Vandenberghe, Christian Vanhove, Scott D. Metzler, and Stephen C. Moore. Review of SPECT collimator selection, optimization, and fabrication for clinical and preclinical imaging. *Medical Physics*, 42(8):4796–4813, jul 2015. http://dx.doi.org/10.1118/1.4927061.

[9] Bailey, Humm, A. Todd-Pokropek, and A. van Aswegen. *Nuclear Medicine Physics: A Handbook for Teachers and Students*. INTL ATOMIC ENERGY AGENCY, March 2015.

[10] Simon R. Cherry, James A. Sorenson, and Michael E. Phelps. *Physics in Nuclear Medicine*. SAUNDERS W B CO, 2012.

[11] Young-Hyu Choi, Cheol-Min Kim, Hwan-Seock Jeong, and Jeong-Ho Youn. Influence of bed temperature on heat shrinkage shape error in FDM additive manufacturing of the ABS-engineering plastic. *World Journal of Engineering and Technology*, 04(03):186–192, 2016. 10.4236/wjet.2016.43D022.

[12] Karel Deprez, Stefaan Vandenberghe, Karen Van Audenhaege, Jonas Van Vaerenbergh, and Roel Van Holen. Rapid additive manufacturing of MR compatible multipinhole collimators with selective laser melting of tungsten powder. *Medical Physics*, 40(1):012501, dec 2012. http://dx.doi.org/10.1118/1.4769122.

[13] Virtual Foundry. 3d tungsten pla. *https://www.thevirtualfoundry.com*, 2019.

[14] Maria Georgiou, Eleftherios Fysikopoulos, Konstantinos Mikropoulos, Eirini Fragogeorgi, and George Loudos. Characterization of "$\gamma$-eye": a low-cost benchtop mouse-sized gamma camera for dynamic and static imaging studies. *Molecular Imaging and Biology*, 19(3):398–407, oct 2016. https://doi.org/10.1007/s11307-016-1011-4.

[15] Maria Georgiou, George Loudos, Eleftherios Fysikopoulos, Efthimis Lamprou, Kwnstantinos Mikropoulos, Antonio Shegani, and Panagiotis Georgoulias. $\lambda$-eye. *Nuclear Medicine Communications*, 37(10):1001–1009, oct 2016. 10.1097/MNM.0000000000000546.

[16] Ian Gibson, David Rosen, and Brent Stucker. *Additive Manufacturing Technologies*. Springer New York, 2015. 10.1007/978-1-4939-2113-3.

[17] David W. Holdsworth, Hristo N. Nikolov, and Steven I. Pollmann. 3d-printed focused collimator for intra-operative gamma-ray detection. *Medical Imaging 2017: Physics of Medical Imaging*, mar 2017. 10.1117/12.2256051.

[18] S Jan, D Benoit, E Becheva, T Carlier, F Cassol, P Descourt, T Frisson, L Grevillot, L Guigues, L Maigne, C Morel, Y Perrot, N Rehfeld, D Sarrut, D R Schaart, S Stute, U Pietrzyk, D Visvikis, N Zahra, and I Buvat. Gate v6: a major enhancement of the gate simulation platform enabling modelling of ct and radiotherapy. *Physics in Medicine and Biology*, 56(4):881–901, jan 2011. doi:10.1088/0031-9155/56/4/001.

[19] S Jan, G Santin, D Strul, S Staelens, K Assié, D Autret, S Avner, R Barbier, M Bardiès, P M Bloomfield, D Brasse, V Breton, P Bruyndonckx, I Buvat, A F Chatziioannou, Y Choi, Y H Chung, C Comtat, D Donnarieix, L Ferrer, S J Glick, C J Groiselle, D Guez, P-F Honore, S Kerhoas-Cavata, A S Kirov, V Kohli, M Koole, M Krieguer, D J van der Laan, F Lamare, G Largeron, C Lartizien, D Lazaro, M C Maas, L Maigne, F Mayet, F Melot, C Merheb, E Pennacchio, J Perez, U Pietrzyk, F R Rannou, M Rey, D R Schaart, C R Schmidtlein, L Simon, T Y Song, J-M Vieira, D Visvikis, R Van de Walle, E Wieërs, and C Morel. Gate: a simulation toolkit for pet and spect. *Physics in Medicine and Biology*, 49(19):4543–4561, sep 2004. doi:10.1088/0031-9155/49/19/007.

[20] Michael Kazhdan and Hugues Hoppe. Screened poisson surface reconstruction. 32(3):1–13, jun 2013. https://doi.org/10.1145/2487228.2487237.

[21] J.C. Khong, R. Speller, S. Dorkings, K. Moss, and R. Moss. Rapid prototyping of cost efficient x-ray collimators. *Manufacturing Letters*, 20:49–53, apr 2019. https://doi.org/10.1016/j.mfglet.2019.05.001.

[22] S. Kowarik, L. Bogula, S. Boitano, F. Carlà, H. Pithan, P. Schäfer, H. Wilming, A. Zykov, and L. Pithan. A novel 3d printed radial collimator for x-ray diffraction. *Review of Scientific Instruments*, 90(3):035102, mar 2019. 10.1063/1.5063520.

[23] Rafal Kudelski, Jacek Cieslik, Mykola Kulpa, Piotr Dudek, Krzysztof Zagorski, and Rafal Rumin. Comparison of cost, material and time usage in FDM and SLS 3d printing methods. In *2017 XIIIth International Conference on Perspective Technologies and Methods in MEMS Design (MEMSTECH)*. IEEE, apr 2017. 10.1109/MEMSTECH.2017.7937521.

[24] William E. Lorensen and Harvey E. Cline. Marching cubes: A high resolution 3d surface construction algorithm. 1987. 10.1145/37401.37422.

[25] Padmakumar M. Additive manufacturing of tungsten carbide hardmetal parts by selective laser melting (SLM), selective laser sintering (SLS) and binder jet 3d printing (BJ3dp) techniques. *Lasers in Manufacturing and Materials Processing*, 7(3):338–371, jul 2020. https://doi.org/10.1007/s40516-020-00124-0.

[26] Olga V. Makarova, Guohua Yang, Platte T. Amstutz, and Cha-Mei Tang. Fabrication of antiscatter grids and collimators for x-ray and gamma-ray imaging by lithography and electroforming. *Microsystem Technologies*, 14(9-11):1613–1619, jan 2008. 10.1007/s00542-008-0558-7.

[27] Brian W. Miller, Jared W. Moore, Harrison H. Barrett, Teresa Fryé, Steven Adler, Joe Sery, and Lars R. Furenlid. 3d printing in x-ray and gamma-ray imaging: A novel method for fabricating high-density imaging apertures. *Nuclear Instruments and Methods in Physics Research Section A: Accelerators, Spectrometers, Detectors and Associated Equipment*, 659(1):262–268, dec 2011. 10.1016/j.nima.2011.08.051.

[28] Vasilis Ntziachristos, Gordon Turner, Joshua Dunham, Stephen Windsor, Antoine Soubret, Jorge Ripoll, and Helen A. Shih. Planar fluorescence imaging using normalized data. *Journal of Biomedical Optics*, 10(6):064007, 2005. https://doi.org/10.1117/1.2136148.

[29] Matthew Rever. *Computer Vision Projects with OpenCV and Python 3*. Packt Publishing, 2018.

[30] Christopher J. Ridley, Pascal Manuel, Dmitry Khalyavin, Oleg Kirichek, and Konstantin V. Kamenev. A novel compact three-dimensional laser-sintered collimator for neutron scattering. *Review of Scientific Instruments*, 86(9):095114, sep 2015. http://dx.doi.org/10.1063/1.4931695.

[31] Adrian Rosebrock. *Practical python and opencv*.

[32] David Sarrut, Mateusz Bała, Manuel Bardiès, Julien Bert, Maxime Chauvin, Konstantinos Chatzipapas, Mathieu Dupont, Ane Etxebeste, Louise M Fanchon, Sébastien Jan, Gunjan Kayal, Assen S Kirov, Paweł Kowalski, Wojciech Krzemien, Joey Labour, Mirjam Lenz, George Loudos, Brahim Mehadji, Laurent Ménard, Christian Morel, Panagiotis Papadimitroulas, Magdalena Rafecas, Julien Salvadori, Daniel Seiter, Mariele Stockhoff, Etienne Testa, Carlotta Trigila, Uwe Pietrzyk, Stefaan Vandenberghe, Marc-Antoine Verdier, Dimitris Visvikis, Karl Ziemons, Milan Zvolský, and Emilie Roncali. Advanced monte carlo simulations of emission tomography imaging systems with gate. *Physics in Medicine and Biology*, 66(10):10TR03, may 2021. doi: 10.1088/1361-6560/abf276.

[33] David Sarrut, Manuel Bardiès, Nicolas Boussion, Nicolas Freud, Sébastien Jan, Jean-Michel Létang, George Loudos, Lydia Maigne, Sara Marcatili, Thibault Mauxion, Panagiotis Papadimitroulas, Yann Perrot, Uwe Pietrzyk, Charlotte Robert, Dennis R. Schaart, Dimitris Visvikis, and Irène Buvat. A review of the use and potential of the gate monte carlo simulation code for radiation therapy and dosimetry applications. *Medical Physics*, 41(6Part1):064301, may 2014. doi:10.1118/1.4871617.

[34] Statista. Worldwide most used 3d printing technologies. https://www.statista.com/statistics/756690/worldwide-most-used-3d-printing-technologies.

[35] M. B. Stone, D. H. Siddel, A. M. Elliott, D. Anderson, and D. L. Abernathy. Characterization of plastic and boron carbide additive manufactured neutron collimators. *Review of Scientific Instruments*, 88(12):123102, dec 2017. https://doi.org/10.1063/1.4998930.

[36] David B. Stout and Habib Zaidi. Preclinical multimodality imaging in vivo. *PET Clinics*, 3(3):251–273, jul 2008. https://doi.org/10.1016/j.cpet.2009.03.001.

[37] Lorenzo Verdenelli, Luigi Montalto, Lorenzo Scalise, Stratos David, George Loudos, Daniele Rinaldi, and Nicola Paone. New opportunities in the design of gamma-camera collimators for medical imaging. In *2021 IEEE Sensors Applications Symposium SAS*, pages 1–6. IEEE, aug 2021. 10.1109/SAS51076.2021.9530134.

[38] Xiaofeng Zhu, Joseph Driewer, Sicong Li, Vivek Verma, Yu Lei, Mutian Zhang, Qinghui Zhang, Dandan Zheng, Timothy Cullip, Sha X. Chang, Andrew Z. Wang, Sumin Zhou, and Charles A. Enke. Technical note: Fabricating cerrobend grids with 3d printing for spatially modulated radiation therapy: A feasibility study. *Medical Physics*, 42(11):6269–6273, oct 2015. http://dx.doi.org/10.1118/1.4932223.